UNIVERSIDAD NACIONAL AUTÓNOMA DE MÉXICO
POSGRADO EN CIENCIAS DE LA TIERRA
INSTITUTO DE GEOFÍSICA
VULCANOLOGÍA

TOMOGRAFÍA DE VOLCANES USANDO EL RUIDO SÍSMICO

TESIS
QUE PARA OPTAR POR EL GRADO DE:
DOCTOR EN CIENCIAS DE LA TIERRA

PRESENTA:

ZACK JACK SPICA

DR. DENIS LEGRAND
INSTITUTO DE GEOFÍSICA

DR. ARTURO IGLESIAS MENDOZA
INSTITUTO DE GEOFÍSICA
DR. CARLOS MIGUEL VALDÉS GONZALÉZ
POSGRADO EN CIENCIAS DE LA TIERRA

MÉXICO, D. F. JUNIO 2015

JURADO

DR. FRANCISCO SÁNCHEZ SESMA INSTITUTO DE INGENIERÍA	PRESIDENTE
DR. YURI TARAN INSTITUTO DE GEOFÍSICA	VOCAL
DR. DENIS LEGRAND INSTITUTO DE GEOFÍSICA	SECRETARIO
DR. ARTURO IGLESIAS MENDOZA INSTITUTO DE GEOFÍSICA	SUPLENTE
DR. PHILIPPE LESAGE ISTERRE, UNIVERSITÉ DE SAVOIE	SUPLENTE

"Appearance rules the world."

Friedrich Schiller

(1759-1805)

Resumen

Tomografía de Volcanes Usando el Ruido Sísmico

Durante la década pasada se demostró que la correlación cruzada de un campo de onda difuso registrado en dos puntos de la Tierra converge hacia la función de Green del medio entre estos dos puntos. Desde entonces, las correlaciones de ruido sísmico ambiental han sido utilizadas en un número considerable de estudios para cartografiar las velocidades de las ondas sísmicas dentro de la corteza terrestre a escalas regionales o continentales. Sin embargo, existen pocos trabajos a escala local, suficientemente detallada para caracterizar una estructura volcánica. El conocimiento de la estructura volcánica, a través de un modelo de velocidad, es esencial para entender los diversos procesos eruptivos que pueden desarrollarse y/o monitorear un volcán activo y, a la sazón, disminuir el riesgo asociado.

El objetivo de este trabajo es estudiar diversos sistemas volcánicos a través de los métodos de correlación de ruido sísmico. Para ello, se eligieron tres complejos volcánicos andesíticos diferentes, tanto por sus características geológicas, como por su comportamiento eruptivo, y por las diversas configuraciones de las redes sísmicas instaladas en ellos. El primer caso de estudio es sobre un volcán mexicano, el volcán de Colima, uno de los estratovolcanes más activos de Norteamérica. Los mapas tomográficos de ondas de grupo de Rayleigh obtenidos a diferentes periodos en este volcán permiten interpretar rasgos de la geodinámica local. El segundo caso de estudio es el área volcánica del Lazufre (Chile-Argentina) que se caracteriza por tener uno de los levantamientos corticales más importantes del mundo. En esta zona, la obtención de un modelo 3-D de ondas S pone en evidencia un sistema magmático a 5 km de profundidad que está acoplado a un sistema hidrotermal más superficial. Ambos reservorios se encuentran debajo del volcán Lastarria, el único volcán activo de la zona. El último volcán estudiado es el Kawah Ijen, en Indonesia. La particularidad de este volcán reside en el hecho que aloja uno de los sistemas volcano-hidrotermales más grandes del mundo. La estructura superficial del volcán y de la caldera fue evaluada gracias a nuevos métodos alternativos usando el ruido sísmico. Entre otros resultados, validamos el método de inversión de los cocientes de densidad de energía direccional del ruido sísmico ambiental (DEDHVR, por sus siglas en inglés) gracias a la comparación directa de los resultados con la geología de la área estudiada.

Cada uno de estos estudios permite comprobar la viabilidad del método de correlación de ruido a periodos muy cortos y en entornos estructuralmente complejos. Cabe resaltar que los resultados muestran las estructuras internas de los volcanes estudiados, lo que permite hacer un aporte para una la mejor comprensión de la estructura interna de los sistemas volcánicos estudiados y de su comportamiento.

Abstract

Ambient Noise Tomography of Volcanic Systems

During the last decade, it has been demonstrated that the correlation of a random seismic wave-field recorded at two sensors converged toward the Green's function of the medium between the sensors. Since then, numerous studies applied the ambient noise correlation technique in order to map seismic waves velocities in the Earth crust at continental or regional scale. At local scale, i.e. detailed enough to characterize the volcanic features, only few studies were conducted. The knowledge of the volcanic structure is essential to understand the various eruptive processes and/or to monitor an active volcano and therefore, mitigate the risk.

The aim of this work is to study several volcanic systems using the ambient seismic noise correlation methods. For this purpose, three different andesitic volcanic complexes were chosen for both, their different geological settings and their eruptive behaviors. The first case of study refers to a mexican volcano, the *volcán de Colima*, which is one of the most active stratovolcanoes in North America. The Rayleigh wave group tomographic maps obtained at different periods allow to interpret features related the local geodynamics. The second case of study focuses on the Lazufre area (Chile-Argentina), which is characterized by one of the world's most important cortical uplift. In this zone, the 3-D S-waves velocity model obtained reveals a magmatic system located at about 5 km depth, which is coupled to a superficial hydrothermal system. Both reservoirs are located below the Lastarria volcano, the only active volcano in the studied region. The last case of study deals with the Kawah Ijen, in Indonesia. The particularity of this volcano resides in the fact that it hosts one of the world's largest volcano-hydrothermal systems. Amongst others results, local velocity profiles of the first thousands of meters are obtained by inverting horizontal to vertical spectral ratio computed through auto-correlation of ambient noise; i.e. according to the directional energy density ratio of ambient noise (DEDHVR). These velocity models are then compared to the geology and important discontinuities are evidenced.

Each of these studies gives valuable information about the viability of the methods at short periods in a structurally complex environment. Mainly, the results highlight the internal structure of these volcanoes, which is a estimable information to understand the volcanic behavior.

Agradecimientos

Mi agradecimiento al Posgrado en Ciencias de la Tierra de la Universidad Nacional Autónoma de México. A los comités, direcciones y personal administrativo del Posgrado, gracias por su guía durante el transcurso de esta investigación. Gracias también a CONACyT por haberme dado la oportunidad de estudiar el doctorado en México.

Mi mayor agradecimiento es para Denis, mi tutor, quien me tendió la mano y me apoyó para iniciar este trabajo. Mi afecto para él, como hombre de muchos valores que siempre trató transmitirme.

A mis asesores: Arturo Iglesias, por ayudarme al inicio de esta tesis, por su generosidad y su paciencia; y Carlos Valdés, por escucharme siempre.

A Francisco Sánchez Sesma por haber participado en mi formación doctoral e interesarse en mis estudios.

A Mathieu Perton, por las discusiones interminables y por las numerosas críticas.

A Víctor Cruz, por ayudarme y también por supervisar una parte de este trabajo. Gracias por su acompañamiento y apoyo incondicional.

Al jurado de grado, Dr. Sanchez Sesma; Dr. Yuri Taran, por las aventuras en Chiapas; Dr. Arturo Iglesias y Dr. Philippe Lesage, por las aventuras en Chambéry. Gracias a todos ellos que con sus observaciones me permitieron mejorar el documento final y concluir este trabajo.

Y gracias a ...

Lilia por los cafés, por tu afecto y por las correcciones del español de este trabajo. A Oryaëlle y Loïc, por chismear todos los días en la cantina. A Oscar, por siempre reirse de todo conmigo. Gracias también a Robin y Nathalie por siempre discutir de todo y de nada. Gracias a todos los estudiantes de vulcanología y de sismología por hacer del instituto de geofísica un lugar agradable y, a veces, divertido. A Dolors y Diana por apoyar tembié en la corrección del español

Gracias a tí, Audrey, por haberme acompañado y soportado a lo largo de estos tres años. Pasamos momentos inolvidables.

Gracias a todos mis amigos de la casa de Cerro Tuera! Gracias a ustedes pasé tres años extraordinarios en esta gran Ciudad de México.

Mi último agradecimiento es para mi mamá. Gracias por creer en mi y por consentirme. Ya por fin no voy a ser estudiante y, te lo prometo, voy a tener un trabajo de verdad!

Índice

Bibliografía

Lista de Figuras

Lista de Tablas

ANT	**A**mbient **N**oise **T**omography
C₃	**C**orrelación de **C**oda de **C**orrelaciones
CCFs	**C**ross-**C**orrelation **F**unctions
CVC	**C**olima **V**olcano **C**omplex
DED	**D**irectional **E**nergy **D**ensity | **D**ensidad de **E**nergía **D**ireccional
DEDHVR	**D**irectional **E**nergy **D**ensity **H**orizontal-to-**V**ertical **R**atio
EGF	**E**lastodynamic **G**reen's **F**unction
GF | FG	**G**reen's **F**unction | **F**unción de **G**reen
FMM	**F**ast **M**arching **M**ethod
FTAN	**F**requency **T**ime **An**alysis
HVSR	**H**orizontal-to-**V**ertical **S**pectral **R**atio | Cociente Espectral **H/V**
InSAR	**In**terferometric **S**ynthetic **A**perture **R**adar
LVZ	**L**ow **V**elocity **Z**one
MATVF	**M**ascota-**A**yutla-**T**apalpa **V**olcanic **F**ields
MGVF	**M**ichoacán-**G**uanajuato **V**olcanic **F**ield
RMS	**R**oot **M**ean **S**quare
RSA	**R**uido **S**ísmico **A**mbiental
SA	**S**imulated **A**nnealing
SNR	**S**ignal-to-**N**oise **R**atio
TMVB	**T**rans-**M**exican **V**olcanic **B**elt

ULVZ   Ultra **L**ow **V**elocity **Z**one

Introducción general

Motivación de la investigación

Durante la última década, se demostró que la correlación cruzada de un campo de onda difuso grabado en dos puntos de la Tierra converge hacia la función de Green del medio entre estos dos puntos; exactamente como si una estación sísmica actuara como fuente y la otra como receptor. Basándose en lo anterior, las técnicas de tomografía que usan el ruido sísmico ambiental tuvieron un desarrollo sin precedentes. Desde el trabajo pionero de Shapiro et al. [2005], se realizaron un número considerable de estudios alrededor del mundo sobre estructuras geológicas muy diversas y para diferentes escalas espaciales. A pesar de que la mayoría de estos estudios fueron realizados a escalas regionales [e.g., de Kool et al., 2006, Ekström et al., 2009, Gaite et al., 2012, Gudmundsson et al., 2007, Iglesias et al., 2010, Karplus et al., 2013, Lin et al., 2007, Nicolson et al., 2012, Nishida et al., 2008, Pyle et al., 2010, Yao et al., 2006, Zheng et al., 2011], también existen varios ejemplos a escala continental [e.g., Bensen et al., 2009, 2008, Saygin and Kennett, 2010, Stehly et al., 2009, Yang et al., 2007, Zheng et al., 2008] o global [e.g., Nishida et al., 2009]. Sin embargo, se han desarrollado muy pocos trabajos a escala local o de detalle, debido por una parte a que se requiere de redes sísmicas densas para llevarlos a cabo y por otra a que el rango de periodo de las funciones de Green extraídas por correlación del ruido sísmico ambiental es mucho menor. Entre los trabajos de este tipo existen los realizados « *offshore* » i.e. aplicados a la prospección petrolera [e.g., Bussat and Kugler, 2011, de Ridder and Dellinger, 2011,

Mordret, 2014, Mordret et al., 2013a,b], a la caracterización de campos geotermales [e.g., Calò et al., 2013, Lehujeur et al., 2013, 2015] y a las tomografías de edificios volcánicos. Entre estos últimos estudios se encuentran los desarrollados en el Piton de la Fournaise (Francia; Brenguier et al. [2007]), la caldera de Toba, (Indonesia; Stankiewicz et al. [2010]) o el volcán Okmok en Alsaka (U.S.A.; Masterlark et al. [2010]). Al inicio de este proyecto de tesis (enero, 2012), estos tres trabajos eran los únicos ejemplos del uso del ruido sísmico ambiental para la obtención de tomografías en volcanes.

Cada sistema volcánico tiene sus propias características físicas y geológicas, debido a la interacción de diferentes factores, como el contexto geodinámico, la presencia de una intrusión magmática y/o de un sistema hidrotermal. El conocimiento de la estructura volcánica es esencial para entender las señales precursoras de actividad que se registran con el monitoreo volcánico, así como comprender los diversos procesos eruptivos que pueden desarrollarse en un volcán en específico. En algunos casos, una tomografía permite evaluar la forma, el tamaño y/o la profundidad de la(s) cámara(s) magmática(s); lo que es una información valiosa para entender la dinámica de recargas y descargas magmáticas y el possible comportamiento de una erupción. La integración de esta información con otros estudios geofísicos, geológicos o volcanológicos constituye la base para evaluar el peligro volcánico de una zona determinada y a reducir el riesgo volcánico.

A pesar de que esta información tiene un gran interés para la comunidad científica y civil, la observación de un cuerpo magmático debajo de un volcán activo sigue siendo excepcional [e.g., Brenguier et al., 2007, Lees, 2007, Marsh, 2000]. Esto se debe a que las técnicas de tomografía "clásicas", basadas en terremotos, adolecen de la baja ocurrencia de temblores. Por tanto, para tener una distribución homogénea de sismos alrededor de la zona de estudio y poder conseguir una resolución satisfactoria de las imágenes, las técnicas clásicas necesitan de una gran cantidad de información; es decir, de registros sísmicos obtenidos por tiempos muy largos y con redes sísmicas densas. Por el contrario, la resolución de las tomografías del ruido sísmico ambiental depende principalmente de la configuración de la red usada, ya que los tiempos de viaje de ondas (fuente-receptor) pueden calcularse entre cada par de estaciones y no tiene dependencia de la tasa de sismicidad regional. Respecto a la geometría de la red de sensores utilizada, una tomografía del ruido sísmico permite recuperar la información a periodos mucho más cortos que una tomografía clásica, por lo que posibilitan la generación de imágenes de las estructuras volcánicas más superficiales. Esto representa una ventaja ya que los cuerpos magmáticos (cámaras, diques, etc. . .)

suelen yacer en los primeros kilómetros de la corteza [e.g., Chaussard and Amelung, 2012, Lees, 2007, Pritchard and Simons, 2004].

Las ventajas que ofrecen los métodos de correlación del ruido sísmico ambiental, así como el carácter novedoso de sus aplicaciones en volcanología motivaron el presente trabajo. El objetivo principal de esta tesis es estudiar diversos sistemas volcánicos y mejorar el conocimiento de sus estructuras internas, mediante la combinación de varios métodos de tratamiento y análisis del ruido sísmico ambiental.

Para alcanzar este objetivo y con el fin de analizar la viabilidad de las técnicas de correlación del ruido en entornos volcánicos complejos, se propuso estudiar tres volcanes alrededor del mundo, que presentan características geológicas, estructurales y eruptivas muy diferentes: el volcán de Colima (Edo. de Colima, México), la zona volcánica de Lazufre (Chile-Argentina) y el volcán Kawah Ijen (Indonesia).

Objetivo general

Obtener los modelos de velocidad y mejorar el conocimiento de las estructuras internas de diversos sistemas volcánicos andesíticos, con entornos estructuralmente muy complejos, mediante el uso de las técnicas de correlación del ruido sísmico ambiental; mostrando que estas son herramientas de gran valor para completar otros estudios geofísicos o geológicos en zonas volcánicas activas.

Objetivos específicos

Con el uso de varias técnicas de correlación del ruido sísmico ambiental se plantearon los siguientes objetivos específicos en la presente investigación:

a) Elaborar, adaptar o mejorar códigos numéricos para el uso de las técnicas de ruido y desarrollarlos para que puedan ser utilizados en paralelo y por lo tanto mejorar el rendimiento del procesamiento de datos.

b) Obtener varios modelos de velocidad 2-D del volcán de Colima (Edo. de Colima, México) y sus regiones circundantes.

c) Obtener un modelo de velocidad 3-D de la zona del Lazufre (Chile-Argentina).

d) Proporcionar información sobre las propiedades mecánicas y obtener modelos de velocidad 1-D para la caldera del Ijen (Indonesia).

e) Analizar las estructuras internas de los sistemas volcánicos estudiados y, si posible, aportar información sobre la ubicación de los reservorios magmáticos y/o hidrotermales.

f) Difundir los resultados adquiridos para cada uno de los estudios.

Contenido y alcances de la investigación

La tesis se estructura en cinco capítulos. Los dos primeros incluyen el marco teórico en el que se basa el desarrollo de la investigación, tanto en relación a nociones de sismología básica (capítulo 1), como en el método de correlación del ruido sísmico ambiental, a través de varios enfoques (capítulo 2). La descripción de las técnicas usadas para las mediciones de ondas superficiales, así como el procesamiento de datos para obtener los mapas tomográficos se incluyeron en el anexo A. Los capítulos 3, 4 y 5 incluyen la aplicación de las técnicas en las tres áreas volcánicas seleccionadas.

En el primer estudio (capítulo 3), se aplicaron la técnica de correlación-cruzada del ruido sísmico ambiental y de tomografía de ondas superficiales en el volcán de Colima y en sus regiones circundantes, que incluyen varios campos volcánicos monogenéticos de los más importantes del mundo (Tlapala, Michoacán-Guanajuato, Ayutla, . . .). Este estudio representa un caso ideal para familiarizarse con los métodos. En efecto, el volcán y las regiones adyacentes contaron con la instalación de redes sísmicas muy densas; lo que permitió obtener una excelente resolución espacial. Además, siendo el volcán de Colima uno de los más estudiados de Norteamérica, los resultados obtenidos en este estudio pudieron ser comparados y discutidos ampliamente. El resultado principal de este estudio es la obtención de mapas de velocidades de las ondas de grupo de Rayleigh a diferentes periodos, que son discutidos dentro en un contexto geodinámico regional. Estos resultados fueron publicados en *Journal of Volcanology and Geothermal Research* y pueden consultarse con la siguiente referencia: Spica, Z., Cruz-Atienza, V. M., Reyes-Alfaro, G., Legrand, D., and Iglesias, A. (2014), Crustal Imaging of Western Michoacán and the Jalisco Block, Mexico, from Ambient Seismic Noise, *Journal of Volcanology and Geothermal Research*, 289, 193–201, doi: 10.1016/j.jvolgeores.2014.11.005.

A continuación, en el capítulo 4, se describe la aplicación de la técnica de tomografía usando el ruido sísmico ambiental, para obtener el campo de velocidad 3-D de la zona volcánica de Lazufre (acrónimo de Lastarria y Cordón del Azufre). El Lazufre es una región muy particular por su dinámica volcánica, ya que se caracteriza por uno de los levantamientos corticales más importantes del mundo, con una tasa de deformación comparable en amplitud y tamaño a la zona de Yellowstone [Froger et al., 2007, Pritchard and Simons, 2004]. En este contexto, la tomografía 3-D nos permitió poner en evidencia una cámara magmática acoplada a un sistema hidrotermal debajo del volcán Lastarria, el único volcán activo de la zona. Los resultados obtenidos tienen grandes implicaciones para las modelaciones InSAR (Interferometric Synthetic Aperture Radar) que son casi los únicos estudios que se pueden realizar para caracterizar esta zona remota y de difícil acceso [Anderssohn et al., 2009, Froger et al., 2007, Henderson and Pritchard, 2013, Pearse and Lundgren, 2013, Pritchard and Simons, 2002, 2004, Remy et al., 2014, Ruch et al., 2008, 2009, Ruch and Walter, 2010]. Los resultados de nuestro trabajo permiten inferir el origen de los gases volcánicos. Nuestro estudio confirma, una vez más, el interés de usar el método de correlación-cruzada del ruido aún cuando el número de estaciones es baja y la geometría de la red sísmica no es ideal. Este trabajo se publicó en *Earth and Planetary Science Letters* con la siguiente referencia: Spica, Z., Legrand, D., Iglesias, A., Walter, T., Heimann, S., Dahm, T., Froger, J.-L., Rémy, D., Bonvalot, S., West, M., Pardo, M., (2015), Hydrothermal and magmatic reservoirs at Lazufre volcanic area, revealed by a high-resolution seismic noise tomography, *Earth and Planetary Science Letter*, 421, 27–38, doi: 10.1016/j.epsl.2015.03.042.

El capítulo 5 se refiere a los estudios realizados en el volcán Kawah Ijen. Este volcán indonesio tiene la particularidad de alojar el lago cratérico de aguas ácidas ($pH \simeq 0.0$) más grande del mundo [e.g., Takano et al., 2004]. En la caldera del Ijen, la disposición de las estaciones sísmicas no permitió aplicar los métodos de tomografía previamente usados, por lo que se propuso la aplicación de diferentes métodos para caracterizar la estructura volcánica usando mediciones del ruido. Para ello, se calcularon varios modelos 1-D tanto con correlación-cruzada del ruido sísmico, como por inversión de los cocientes de densidad de energía direccional del ruido ambiental (i.e. calculados por auto-correlación del ruido sísmico). Los modelos obtenidos permiten caracterizar las grandes estructuras de la caldera del Ijen y ciertas características mecánicas del volcán Kawah Ijen. Este trabajo demuestra la posibilidad de obtener información valiosa del ruido sísmico ambiental a pesar de que la configuración de la red sísmica es desfavorable. Los resultados de este estudio se publicaron

en *Journal of Volcanology and Geothermal Research* como: Spica, Z., Caudron, C., Perton, M., Lecocq, T., Camelbeeck, T., Legrand, D., Piña-Flores, J., Iglesias, A., Syahbana D., (2015), Velocity models and site effects at Kawah Ijen volcano and Ijen caldera (Indonesia) determined from ambient noise cross-correlations and directional energy density spectral ratios. *Journal of Volcanology and Geothermal Research.*

Finalmente se presentan las conclusiones generales y las perspectivas que ofrece este trabajo de tesis. Entre otros, se hace referencia a las herramientas y capacidades instaladas en el Instituto de Geofísica a partir de este trabajo, así como los proyectos de investigación en curso que utilizaron los resultados y desarrollos obtenidos durante este proyecto doctoral.

Bases de sismología

1.1. Ecuación de onda

La evolución espacio-temporal de una excitación f dentro de un medio continuo sin atenuación e inelástico, suele ser descrita a través de dos ecuaciones:

la ecuación de difusión
$$\left[\Delta - \frac{1}{D}\frac{\partial}{\partial t} \right] \quad \phi(\vec{r}, t) = f(\vec{r}, t); \tag{1.1}$$

y la ecuación de onda
$$\left[\Delta - \frac{1}{c^2}\frac{\partial^2}{\partial t^2} \right] \quad \phi(\vec{r}, t) = f(\vec{r}, t): \tag{1.2}$$

donde D es el coeficiente de difusión y c la velocidad de una onda asociada a cualquier valor físico ϕ (escalar o vectorial). Estas dos ecuaciones elementales tienen propiedades sumamente diferentes. Típicamente, la ecuación de onda (1.2) es simétrica por inversión temporal (cf. 2.3); lo que significa que si $\phi(\vec{r}, t)$ es solución de la ecuación, $\phi(\vec{r}, -t)$ también es una solución (principio de reciprocidad). Por el contrario, la ecuación de difusión (1.1) no tiene esta propiedad de simetría. Esta sencilla diferencia tiene consecuencias mayores sobre la física de los procesos de propagación de las ondas ya que es reversible mientras que la difusión no lo es. Por lo tanto, las ondas pueden ser manipuladas para obtener información sobre la fuente, mientras que los fenómenos de difusión no lo permiten.

1.2. Las ondas sísmicas

Cuando un sólido elástico está deformado, la relajación de la tensión que provocó dicha deformación permite al sólido volver a tener su forma inicial. Entonces, la ecuación de propagación de una onda sísmica en un medio elástico, homogéneo e isótropo, suele ser descrita por el primer principio de la dinámica:

$$\rho\frac{\partial^2 \vec{u}}{\partial t^2} = (\lambda + 2\mu)\vec{\nabla}(\nabla \vec{u}) - \vec{\triangle} \wedge (\vec{\triangle} \wedge \vec{u}) + f, \tag{1.3}$$

donde $\vec{u}$ es el vector de desplazamiento del suelo al paso de la onda (típicamente lo que será registrado en una estación sismológica), ρ es la masa volumétrica, $\vec{\nabla}$ es el gradiente, $\nabla \vec{u}$ es la divergencia, $\vec{\triangle} \wedge \vec{u}$ es el rotacional y f una función fuente. λ y μ son los coeficientes de Lamé que describen las propiedades elásticas del medio. Considerar el medio como homogéneo e isótropo, significa que los parámetros ρ, λ y μ son constantes y que la propagación es la misma en todas las direcciones. La ecuación diferencial 1.3 describe la

propagación de una deformación en términos de ondas elásticas.

En los sólidos elásticos existen tres grandes familias de ondas: las *ondas de volumen* (cf. 1.2.1), las *ondas de superficie* (cf. 1.2.2) y las ondas de campo cercano[1].

1.2.1. Las ondas de volumen

El vector desplazamiento resulta de la contribución de las ondas P y S. Así, el vector desplazamiento $\vec{u}$ de la ecuación 1.3 puede descomponerse en dos campos vectoriales: $\vec{u} = \vec{u}_P + \vec{u}_S$, con $\vec{u}_P = \vec{\nabla}\phi$ y $\vec{u}_S = \vec{\triangle} \wedge \psi$, donde $\vec{u}_P$ proviene de una fuente escalar con $\vec{\triangle} \wedge \vec{u}_P = \vec{0}$ y $\vec{u}_S$ proviene de una fuente rotacional con $\vec{\nabla}\vec{u}_S = \vec{0}$ y $\nabla\vec{u}_S = \vec{0}^2$

Sustituyendo el campo $\vec{u}$ dentro de la ecuación 1.3, se obtiene una ecuación de onda (cf. 1.2) de la siguiente forma:

$$\frac{1}{c^2}\frac{\partial^2 p}{\partial t^2} = \triangle p, \tag{1.4}$$

donde p es igual a $\vec{u}_P$ o a $\vec{u}_S$, c es la velocidad de la onda dentro del medio considerado y $\triangle$ es el Laplaciano. Si $p = \vec{u}_p$, la velocidad de la onda será:

$$v_P = \sqrt{\frac{\lambda + 2\mu}{\rho}}; \tag{1.5}$$

si $p = \vec{u}_S$ la velocidad será:

$$v_S = \sqrt{\frac{\mu}{\rho}}. \tag{1.6}$$

Las ecuaciones 1.5 y 1.6 describen los dos tipos fundamentales de propagación de ondas de volumen dentro de un medio elástico. En sismología, son denominadas ondas P y S, respectivamente.

- Las ondas P ($\vec{u}_P$, 1.5) de compresión, son polarizadas longitudinalmente; es decir en una dirección paralela a la dirección de propagación (proviene de un escalar).

- Las ondas S ($\vec{u}_S$, 1.6; también llamadas ondas de corte o de cizalla), son polarizadas transversalmente; es decir, en una dirección perpendicular a la dirección de propagación (proviene de un rotacional). Para una misma dirección de propagación, la ondas

---

[1]Las ondas de campo cercano son ondas que llegan entre la onda P y la onda S y que decaen en $1/r^2$, mientras que las ondas de volumen decaen en $1/r$. Son ondas que no vamos a considerar en nuestros estudios.

[2]Sin tomar en cuenta las ondas de campo cercano.

S suelen ser separadas en ondas SH y SV, las cuales corresponden a la deformación dentro del plano horizontal y vertical respectivamente.

Los parámetros de propagación del medio (ρ, λ y μ) influyen sobre la velocidad de propagación de las ondas. Sin embargo, las ondas de compresión siempre se propagan más rápidamente que las ondas de corte ($V_p > V_s$). Es igualmente importante señalar que las velocidades de estas ondas dependen únicamente de dichos parámetros.

1.2.2. Las ondas de superficie

En la interfaz entre el medio de propagación elástico y la superficie libre (el aire o el vacío, como entre cualquier otra interfaz dentro de la Tierra) las ondas P y S interfieren de manera constructiva, produciendo las ondas de superficie.

Distinguimos dos tipos de ondas de superficie: las ondas de *Rayleigh* y las ondas de *Love*. Las ondas de Rayleigh resultan de interferencias constructivas entre las ondas P y SV. Por ello, la polarización de estas ondas es elíptica (retrograda en superficie libre y prograda en profundidad) y la amplitud del movimiento decrece de manera exponencial con la profundidad [Aki and Richards, 2002]. Las ondas de Love resultan de interferencias constructivas de la componente horizontal (SH) entre la superficie libre y una (o varias) discontinuidad(es) en profundidad. La polarización de estas ondas es lineal, como la de las ondas SH y su amplitud decrece de manera exponencial con la profundidad. Las ondas de superficie se mueven a menos velocidad que las ondas de volumen ($c < V_s < V_p$; donde c es la velocidad de fase), pero tienen la particularidad de presentar variaciones de velocidad con la profundidad y la frecuencia. Esta propiedad, llamada « *dispersión* » (cf. 1.2.2.1), es particularmente útil para cuantificar ciertas propiedades físicas de la Tierra.

1.2.2.1. Dispersión de las ondas de superficie

Cuando las ondas de superficie viajan en un medio estratificado, la velocidad de propagación de cada uno de los modos que constituyen estas ondas depende de la frecuencia. En efecto, las ondas de superficie son sensibles a diferentes profundidades con respecto a su longitud de onda. Por tanto, una longitud de onda pequeña λ será más sensible en las estructuras superficiales del subsuelo. Ahora bien, la longitud de onda está vinculada a la frecuencia (ν) a partir de la relación $\lambda = \frac{c}{\nu}$; por consiguiente, las ondas de superficie

tienen una sensibilidad a la profundidad inversamente proporcional a la frecuencia. La relación $c(\omega)$ representa esta propiedad, ya que vincula la velocidad c a la pulsación ω ($\omega = 2\pi\nu$); relación que describe la dispersión de las ondas de superficie sólo dependiendo de los parámetros físicos del medio (velocidad de las ondas P, velocidad de las ondas S) [Stein and Wysession, 2009].

Debido a que que una onda de superficie está constituida por varios modos de propagación (para una frecuencia dada solo existen un número finito de velocidades posibles), un sismograma de ondas de superficie suele ser descrito cómo una superposición de varios modos[3]:

$$U(r_0, r, \omega) = \sum_{\nu} U^{\nu}(r_0, r, \omega), \tag{1.7}$$

donde r_0 es la posición de la fuente, r la posición del receptor, ω la frecuencia y ν el número del modo. En el caso 2-D, donde x y z representan las direcciones horizontal y vertical respectivamente, cada modo tomado por separado es solución de la ecuación de Helmholtz:

$$\nabla^2 U^{\nu}(x, z, \omega) + \frac{\omega^2}{c_{\nu}^2(\omega)} U^{\nu}(x, z, \omega) = 0, \tag{1.8}$$

lo que para un medio ligeramente heterogéneo lateralmente, permanece válido [Woodhouse, 1974]:

$$\nabla^2 U^{\nu}(x, z, \omega) + \frac{\omega^2}{c_{\nu}^2(x, z, \omega)} U^{\nu}(x, z, \omega) = 0. \tag{1.9}$$

Considerando una onda plana de amplitud A y de fase $\phi = \omega\tau$, una de las soluciones generales de la ecuación 1.9 puede escribirse como:

$$U(x, z, \omega) = A(x, z, \omega) e^{i\omega\tau(x, z, \omega)}. \tag{1.10}$$

Introduciendo la solución 1.10 en la ecuación 1.9, encontramos que:

$$e^{i\omega\tau} \left(\nabla^2 A - A\omega^2 (\nabla\tau)^2 + 2i\omega\nabla A\nabla\tau + i\omega A\nabla^2\tau \right) = -\frac{\omega^2}{c^2} A e^{i\omega\tau}. \tag{1.11}$$

Igualando las partes reales, obtenemos la ecuación Eikonal que depende de la frecuencia:

$$\|\nabla\tau(x, z, \omega)\|^2 = \frac{\nabla^2 A(x, z, \omega)}{\omega^2 A(x, z, \omega)} + \frac{1}{c^2(x, z, \omega)}. \tag{1.12}$$

---

[3]la siguiente demostración (ecuaciones 1.7 a la 1.14) fue modificada de Mordret [2014].

Si nos limitamos a las altas frecuencias, la ecuación 1.12 puede ser simplificada como:

$$\|\nabla\tau(x,z,\omega)\|^2 = \frac{1}{c^2(x,z,\omega)}, \tag{1.13}$$

lo que nos da la ecuación Eikonal sin dependencia de la frecuencia o de la amplitud de la onda. Una de las soluciones de esta ecuación,

$$\tau(x,z,\omega) = \int_{rayo} \frac{\mathrm{d}l}{c(x,z,\omega)}, \tag{1.14}$$

es la base de la tomografía de tiempo de arribo.

Sin embargo, para describir de manera más completa el movimiento de una onda, se deberían también considerar otros parámetros del medio tales como: Δ - la distancia fuente-receptor, φ - el azimut entre la fuente y el receptor -, s^ν - la función fuente -, p^ν - una función de polarización -, $\alpha^\nu(\omega)$ - la función de atenuación y/o $k^\nu(\omega)$ - la función (o curva) de dipersión (siendo $k = {}^{2\pi}/\lambda$ el número de onda). Sin embargo, la función (y medición) más usada es la curva de dispersión de las ondas de superficie

$$k^\nu = {}^\omega/c^\nu(\omega), \tag{1.15}$$

que está relacionada a todos los parámetros del medio con particular sensibilidad a la velocidad de las ondas S. La ecuación precedente (1.15) describe la velocidad de fase c de una onda de superficie. La velocidad de fase es aquella con la que viaja cada armónico (uno distinto para cada frecuencia) de una onda sísmica. También existe una velocidad característica de los paquetes completos de energía, cuya velocidad es denominada velocidad de grupo (U). La velocidad de grupo se define como:

$$U = \frac{\partial\omega}{\partial k}. \tag{1.16}$$

Debido que $c = {}^\omega/k$, existe una relación que vincula la velocidad de fase a la velocidad de grupo:

$$c = U + k\frac{\partial c}{\partial k} = \frac{U}{1 - \frac{\omega}{c}\frac{\partial c}{\partial\omega}}. \tag{1.17}$$

Por tanto, conociendo la velocidad de fase es posible deducir la velocidad de grupo. Sin embargo, lo opuesto no es posible, como muestra la ecuación 1.17.

1.2.3. La coda

La Tierra no es un medio homogéneo, ni estratificado de forma simple. Por el contrario, presenta heterogeneidades a todas las escalas. Una parte de las ondas generadas por terremotos será reflectada en las interfases entre los estratos, mientras otra será refractada o reflectada cuando encuentre heterogeneidades dentro de la corteza terrestre [Aki and Chouet, 1975].
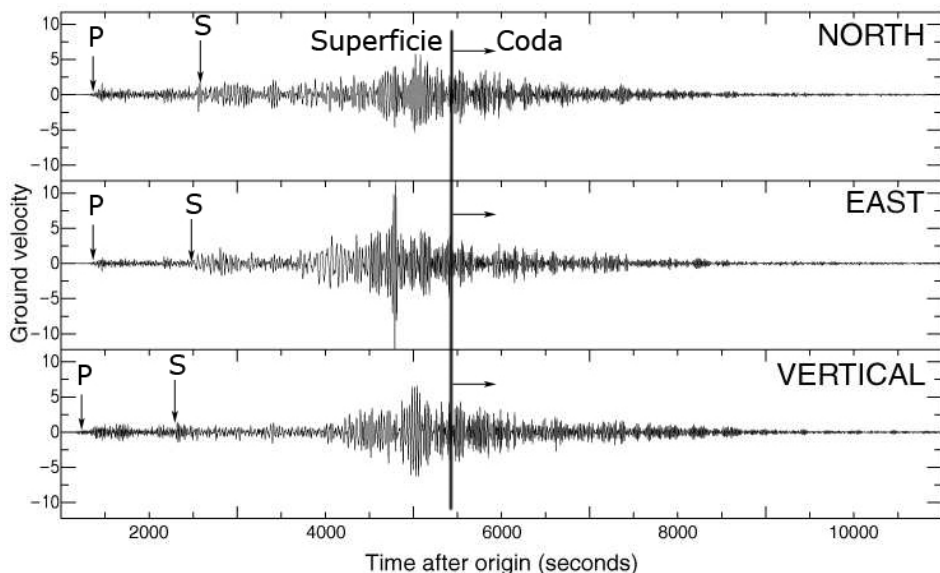
FIGURA 1.1: Ejemplo del sismograma del terremoto de Sumatra (26/12/2004) registrado en Arizona. Pueden identificarse las ondas P, S y de superficie. La última parte del registro es la coda sísmica, que puede durar varios minutos.

La coda es la parte de la señal que tiene por origen la difusión de las ondas dentro de la Tierra [Aki, 1969, Aki and Chouet, 1975, Margerin et al., 1999]. Estas ondas « *difusas* » recorren distancias mucho más largas y llegan a la estación sísmica incluso más tarde que las ondas de superficie. Como podemos ver en la Figura 1.1, la señal perdura varios minutos después de la llegada de las ondas directas (P y S), mientras que el fenómeno a la fuente de la generación de las ondas sísmicas ocurre solamente durante algunos segundos. El tiempo de recorrido correspondiente a la coda es, en promedio, casi igual a diez veces el tiempo de recorrido de las ondas directas (sin reflexiones y refracciones) entre la fuente y el sismómetro. Entonces, se puede considerar que las ondas han sondado un volumen del medio de propagación proporcional a la distancia que recorrieron. Por lo tanto, la coda todavía contiene información estadística sobre el medio, ya que existe una equivalencia entre el tiempo de observación y la distancia recorrida.

Debido a su rasgo aleatorio y caótico, la coda sísmica parece ser una señal incoherente (y durante mucho tiempo ha sido considerado como tal). Efectivamente, cada vez que una onda es reflectada por un difusor, cambia de dirección, de fase, de amplitud y no se pueden predecir sus características finales. Sin embargo, la coda conserva un carácter perfectamente determinista. Por ejemplo, dos registros sucesivos realizados en el mismo sitio, con una misma fuente y el mismo sensor, darán estrictamente la misma señal. En contraposición, si solamente se modifica un difusor sencillo, la coda será drásticamente diferente [Tourin et al., 2001]. En conclusión, la coda es muy sensible a las variaciones del medio. Esta propiedad fue utilizada en acústica y permite medir perturbaciones ínfimas dentro de un medio [Cowan et al., 2000] y también ha sido usada en sismología con el método de « *coda wave interferometry* » [Snieder, 2002, 2006, e.g.,].

Otra propiedad estadística de la coda es que el fenómeno de difusión produce una conversión y una redistribución de la energía entre los diferentes modos de propagación. Así, después de un gran número de difusiones, la energía es, supuestamente, « equiparticionada » entre todos los modos de propagación de las ondas [Campillo et al., 1999, Hennino et al., 2001, Margerin et al., 2000, Shapiro et al., 2000]. De la misma manera, debido a las múltiples difusiones aleatorias, la señal registrada en el sensor será isótropa, sin ninguna dirección predominante, después de un tiempo suficientemente largo (lo que depende de las velocidades de las ondas y de la tasa de difusión del medio). Por tanto, existen dos regímenes de « equipartición »: uno de energía y uno de dirección, que son obtenidos solo asintóticamente ($t \to \infty$), con tiempo característico diferente [Paul et al., 2005]. Una propiedad remarcable de la coda es que la evolución de su intensidad se explica con una ecuación de difusión (1.1) y no con una ecuación de onda [Margerin et al., 1999].

La coda domina una gran parte de la señal y también contiene la mayor parte de la energía. Aki and Chouet [1975] demostraron que la coda contiene información a pesar de su aspecto caótico. Estos autores mostraron que la disminución temporal de la energía de la coda se traduce a una característica física regional y que esta particularidad es independiente de las propiedades de la fuente (magnitud, localización, mecanismo focal, etc.). En efecto, para una pulsación ω, la envolvente E_ω de la coda sigue una ley exponencial:

$$E_\omega(t) \propto \frac{1}{t^\gamma} e^{\left(-\frac{\omega t}{Q_c(\omega)}\right)}, \tag{1.18}$$

$1/t^\gamma$ siendo un factor geométrico, con γ comprendida entre 1 y 2 y Q_c es el « *factor de calidad* » de la coda que es un número adimensional, dependiente de la frecuencia de la

región estudiada.

Entre 1969 y 1975, Aki [1969] y Aki and Chouet [1975] expusieron dos posibles explicaciones :

- o la coda resulta de la difusión sencilla y por tanto la disminución de su envolvente se relaciona con la absorción del medio;

- o la coda resulta de la difusión múltiple y en este caso, su evolución puede explicarse por las propiedades de difusión del medio de propagación.

Actualmente, se acepta que la coda resulta de la difusión múltiple y que la disminución de su energía es descrita correctamente por la ecuación de transferencia de radiación [Margerin et al., 1999, Ryzhik et al., 1996].

1.3. El ruido sísmico ambiental

Con el desarrollo de enormes redes sismológicas alrededor del mundo, una cantidad muy importante de datos continuos está disponible actualmente. Sin embargo, la casi totalidad de las señales registradas es ruido. Durante la década pasada, se demostró que el ruido sísmico ambiental (RSA) todavía contiene una información determinista acerca de las características físicas del medio (de la Tierra) y que dicha información puede extraerse mediante su correlación cruzada. El RSA se ha convertido en una señal, lo que ofrece la posibilidad de producir imágenes de las características físicas de la Tierra, tomografías sin fuente (« *imaging without a source* » o « *passive imaging* »).

En este trabajo, planteamos el uso del RSA para obtener imágenes tomográficas de la corteza terrestre somera en zonas volcánicas. Veremos en el capítulo 2 que esto es posible si consideremos el RSA como un campo *difuso*, exactamente como la coda [Shapiro and Campillo, 2004]. En efecto, la derivada temporal de la inter-correlación de un campo difuso registrado entre dos puntos es igual a la *función de Green* (FG; cf. 1.4) entre estos dos puntos [Weaver and Lobkis, 2001]. Sin embargo, esta teoría requiere que la corteza terrestre tenga propiedades de difusión y/o que las fuentes que generan el RSA sean « *equiparticionadas* », es decir, repartidas aleatoriamente alrededor de los receptores.

Antes de abordar la teoría de correlación de un campo difuso en el capítulo 2 es necesario definir las características de nuestras herramientas de trabajo.

1.3.1. Características del ruido sísmico ambiental

El RSA se compone de todas las ondas emitidas de manera aleatoria (en apariencia) por fuentes de baja amplitud. A diferencia de los terremotos, es difícil localizar sus fuentes, ya que no es posible identificar cada una de las señales que constituye el ruido. Por lo tanto, es muy difícil ubicar la posición y encontrar la señal asociada a cada fuente.

La caracterización del RSA fue abordada en diversos estudios durante las últimas décadas [e.g., Asten, 1978, Friedrich et al., 1998, Gutenberg, 1958, Nishida et al., 2009, Stehly et al., 2006]. El ruido puede ser generado por las mareas, las oleadas, el efecto del viento en la superficie de la Tierra o sobre los árboles, la circulación en carreteras y más de forma genérica por todas las actividades humanas. Gutenberg [1958] y Asten [1978] definieron diferentes categorías del ruido sísmico en función de su frecuencia. Generalmente se definen tres categorías:

1. a bajas frecuencias ($<1\ Hz$), con fuentes generalmente naturales (oceánicas, fenómenos meteorológicos de gran envergadura, etc.);

2. a frecuencias intermedias (de 1 a 5 Hz), con fuentes también de origen natural (fenómeno meteorologicos locales como viento, lluvia, etc.) y/o antrópicas (urbanas) y

3. a altas frecuencias ($>5\ Hz$) con fuentes únicamente antrópicas (fábricas, tráfico, estaciones de bombeo, etc.).

Esta clasificación permite distinguir el microtremor (de origen antrópico) del microsismo (de origen natural). Friedrich et al. [1998] o Bonnefoy-Claudet et al. [2006b] demostraron que las ondas de superficie generan la mayor parte de la energía contenida dentro del ruido sísmico. Esta observación sugiere que el ruido es efectivamente generado en la superficie de la Tierra, y más específicamente en los océanos.

La mayor parte de la energía del RSA se concentra en la banda de 5 a 20 s (Figura 1.2). Esta parte del espectro presenta dos picos: uno bien definido a 7 s y otro con menor definición a 14 s. Estos picos se denominan "pico microsísmico primario" y "pico microsísmico secundario" respectivamente. Los dos son atribuidos a la marea oceánica (« *seismic hum* »). La frecuencia del pico primario corresponde a la frecuencia dominante de las olas oceánicas y se genera por las diferentes presiones sobre el fondo oceánico, resultado de las

interacciones no lineales de las olas [Longuet-Higgins, 1950]. El ruido generado a muy bajas frecuencias puede ser registrado en todas las partes de la Tierra, aunque sea originado en los océanos profundos [e.g., Stehly et al., 2006]. Por el contrario, el ruido con frecuencias superiores a 100 Hz está presente únicamente en las proximidades de las ciudades o zonas con actividad humana. El RSA no parece cumplir la propiedad de isotropía de la misma manera para bajas o altas frecuencias.
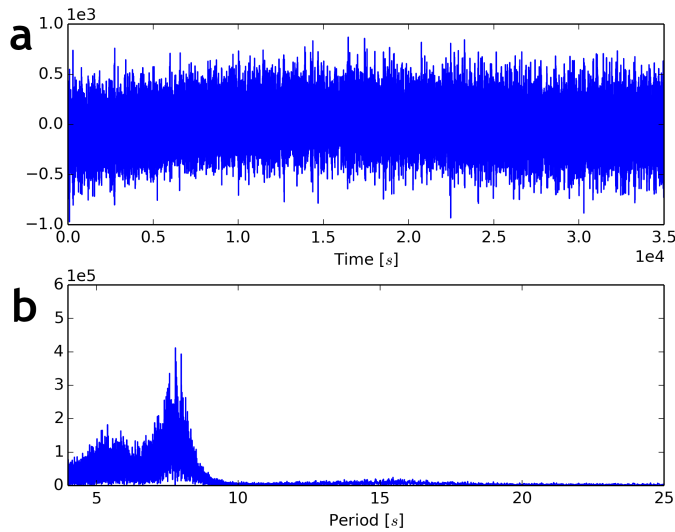
FIGURA 1.2: (a) Registro de una hora (el 23/10/2011) de ruido sísmico en la estación PSG en el volcán Kawah Ijen, Indonesia. (b) Transformada de Fourier del mismo registro; el pico de 7 s es el más importante.

Stehly et al. [2006] mostraron que para los periodos alrededor de 5 – 10 s, el RSA es directivo y estable en el tiempo. Para periodos más largos (de 10 – 20 s y de 20 – 40 s), el RSA es menos direccional pero presenta grandes variaciones por temporadas [e.g., Caudron, 2013, Landès et al., 2010]. El RSA de 10 – 20 s puede ser generado por fuentes puntuales y locales, correspondientes a las tormentas oceánicas [Landès et al., 2010].

1.3.2. Ventajas del uso del ruido sísmico ambiental

Con la evolución de las técnicas de adquisición, de almacenaje y de procesamiento de datos sísmicos, la duración de los registros ha aumentado considerablemente. Actualmente y desde hace alguna(s) decena(s) de años (dependiendo de las áreas geográficas), los datos sísmicos son registrados de manera continua. La Figura 1.3 presenta un día completo de datos: aunque en esta jornada ocurrió un terremoto, este representa solo una pequeña parte del registro. Es frecuente que ocurran días y/o periodos largos de tiempo durante

los cuales no se registran terremotos, sino únicamente RSA.

Los métodos tomográficos sísmicos « tradicionales » usan los tiempos de arribo de las

un día de registro sísmico
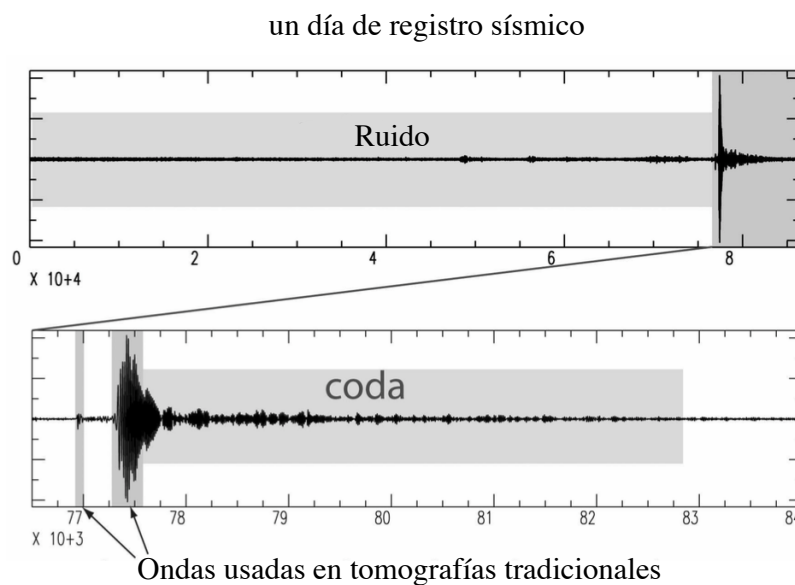
FIGURA 1.3: Ejemplo de un día de registro sísmico incluyendo un terremoto. El RSA representa aproximadamente 95 % del tiempo del registro, el 4 % corresponde a coda y el 1 % a las ondas utilizadas en métodos tomográficos tradicionales. (modificado de Gouédard [2008]).

ondas generadas por terremotos. Con estos métodos, para obtener una imagen tomográfica con una resolución satisfactoria, se requieren muchos registros de sismos que sondeen la zona de estudio con diferentes azimuts. En las zonas sísmicamente activas (zona de falla(s), cerca de los límites de placas), el tiempo de espera previo al registro de un sismo puede ser largo, obligando a instalar y operar redes sísmicas durante numerosos años, lo que es costoso. Por otra parte, es casi imposible estudiar regiones asísmicas. Por lo tanto, los métodos tomográficos tradicionales adolecen de la limitación espacio-temporal de la ocurrencia de terremotos.

El uso del RSA permite superar estas limitaciones, debido a que este es propio de la Tierra. Por otra parte, se suprime el problema de fuente, ya que usando métodos pasivos, la resolución de las imágenes tomogáficas depende principalmente de la configuración de la red sísmica usada y no de la distribución de las fuentes. Además, no es necesario que el tiempo de adquisición sea muy extenso.

1.4. La función de Green

La función de Green ($FG(\vec{r}, t)$) es la solución general de la ecuación 1.3 para una fuente impulsional, un Dirac ($\int \delta(t)\mathrm{d}t = 1$), con las condiciones de frontera siguientes:

$$\begin{cases} FG(\vec{r} \to \infty) & = 0 \\ FG(t = 0) & = 0 \\ \frac{\partial FG}{\partial t}(t = 0) & = 0 \end{cases}$$

Entonces, según 1.2:

$$\left[\Delta - \frac{1}{c^2} \frac{\partial^2}{\partial t^2} \right] \quad FG(\vec{r}, t) = \delta(\vec{r})\delta(t). \tag{1.19}$$

Un Dirac se describe como una sumatoria infinita de todas las frecuencias continuas de igual amplitud (i.e. la transformada de Fourier de un Dirac es una constante: $\mathcal{F}\{\delta(t)\} = 1$, es decir, contiene todas las frecuencias). La FG permite caracterizar un sistema porque representa la salida de un Dirac que contiene la salida a todas las frecuencias.[4]

Por lo tanto, sean dos puntos cualesquiera A y B de un sólido, los desplazamientos en $A(\vec{u}(A, t))$ y $B(\vec{u}(B, t))$ estarán vinculados por la siguiente relación: $\vec{u}(A, t) = FG(A, B, t) \otimes \vec{u}(B, t)$, donde $FG(A, B, t)$ es la FG entre A y B (y por tanto la solución general de la ecuación 1.3) y el símbolo $\otimes$ es la convención para describir la convolución. Gracias al principio de reciprocidad tratado en 1.1, la propagación de las ondas entre los puntos A y B puede escribirse como:

$$FG(A, B, t) \otimes FG(A, B, -t) = \delta(t) \tag{1.20}$$

Así, la FG permite caracterizar completamente la propagación de las ondas dentro de un medio dado.

El campo de desplazamiento puede generalizarse a un espacio en tres dimensiones $(O, \vec{i}, \vec{j}, \vec{k})$, donde el desplazamiento $\vec{u}$ es definido por tres coordenadas $(u_{\vec{i}}, u_{\vec{j}}, u_{\vec{k}})$. Por lo tanto, para describir de manera completa el campo de desplazamiento de los dos puntos A y B se deben determinar nueve FFG diferentes. Dichas soluciones se agrupan en una matriz

---

[4]En esta definición matemática de la función de Green, no se especifica con ninguna cantidad física. Por tanto, se puede definir varias funciones de Green, de acuerdo que $FG(\vec{r}, t)$ representa (p.e.) un desplazamiento, una velocidad o una aceleración.

llamada Tensor de Green que tiene la siguiente estructura:

$$FG(A,B,t) = \begin{pmatrix} FG(A,B,t)_{\vec{i}\vec{i}} & FG(A,B,t)_{\vec{i}\vec{j}} & FG(A,B,t)_{\vec{i}\vec{k}} \\ FG(A,B,t)_{\vec{j}\vec{i}} & FG(A,B,t)_{\vec{j}\vec{j}} & FG(A,B,t)_{\vec{j}\vec{k}} \\ FG(A,B,t)_{\vec{k}\vec{i}} & FG(A,B,t)_{\vec{k}\vec{j}} & FG(A,B,t)_{\vec{k}\vec{k}} \end{pmatrix},$$

donde $FG(A,B,t)_{\vec{i}\vec{j}}$ describe la relación entre el desplazamiento en la dirección $\vec{i}$ para el punto A ($\vec{u}(A,t)$) y el de la dirección $\vec{j}$ en el punto B ($\vec{u}(B,t)$).

1.5. Síntesis

La propagación de ondas de volumen y de superficie es la repuesta a la deformación de un sólido elástico. Gracias a las características de estas ondas, la sismología estudia las propiedades físicas y estructurales de la Tierra. Generalmente, se utilizan los tiempos de arribo de las ondas generadas por grandes o pequeños movimientos de la corteza terrestre para obtener imágenes del subsuelo. El uso de las técnicas tomográficas tradicionales implica una localización espacial de la fuente de los terremotos. Por lo tanto, la señal sísmica debe ser registrada en un número de estaciones importante y debe ser, idealmente, de gran amplitud.

El rápido desarrollo de los sistemas de adquisición numéricos y la sorprendente cantidad de datos disponible, llevaron a los sismólogos a interesarse por nuevas señales. Hoy en día, los « campos difusos » tales como la coda o el ruido sísmico son considerados como señales deterministas que pueden utilizarse para caracterizar las propiedades física del interior de la Tierra. Este desarrollo técnico llevó a la sismología a explorar nuevos métodos de análisis. Una de éstas es el estudio de las estructuras volcánicas a través de la correlación de las vibraciones ambientales.

En el capítulo siguiente, se presentan las bases teóricas y la evolución histórica de la técnica de correlación del RSA. Mediante la recopilación de diversos trabajos, se analizan las condiciones para las cuales la teoría es válida y las propiedades de las funciones de correlación obtenidas por correlación cruzada.

Correlación del ruido sísmico ambiental y la Función de Green

2.1. Correlación del ruido sísmico ambiental

La derivada temporal de la correlación cruzada de un campo difuso medido entre dos puntos converge hacia la FG del medio entre estos dos puntos [Weaver and Lobkis, 2001], incluyendo todas las reflexiones, difracciones y modos de propagación [Weaver, 2005], con la siguiente expresión:

$$\delta_\tau C_{AB} \propto FG^+(A, B, \tau) - FG^-(A, B, -\tau), \tag{2.1}$$

donde FG^+ representa la parte positiva (causal) y FG^- la parte negativa (acausal) de la función de correlación entre A y B. Este significativo resultado se ha demostrado teóricamente, experimentalmente y empíricamente para numerosos campos científicos tales como la acústica [Weaver and Lobkis, 2001], la sismología [Campillo and Paul, 2003, Shapiro and Campillo, 2004] o el electromagnetismo [Fan et al., 2010].

2.1.1. Revisión Histórica

Aki [1957] fue el primer investigador en interesarse en la coda de los terremotos y en el RSA. Aki afirmaba que, desde el punto de vista de la fase, es posible deducir la naturaleza del medio de propagación, a partir de las ondas generadas por la microsismicidad, tremores volcánicos, microtremores generados por el tráfico u otros tremores de origen artificial. Además, mostró como el coeficiente de auto-correlación de los movimientos verticales es proporcional a la función de Bessel de orden cero. Esto se interpretó 50 años después, relacionándose a la parte imaginaria de la FG escalar [Sánchez-Sesma and Campillo, 2006]. Basándose en las características estadísticas del campo de onda, tanto en el tiempo como en el espacio, por las cuales se asumen ondas estacionarias, el método de Aki permitió extraer curvas de dispersión desde el microtremor. En este trabajo pionero se llevó a cabo el desarrollo del método SPAC (« *Spatial Autocorrelation* », por sus siglas en inglés).

Históricamente, fue en heliosismología que las correlaciones del ruido fueron usadas por primera vez, usando correlaciones de las fluctuaciones de los movimientos de la superficie del Sol con la finalidad de medir las velocidades de propagación de las ondas P dentro del astro [Duvall et al., 1993, Giles et al., 1997].

Más adelante, Weaver and Lobkis [2001] demostraron que las auto-correlaciones de un campo acústico difuso en la superficie de un bloque de aluminio son iguales a la FG del mismo cuerpo. Un resultado similar fue obtenido correlacionando los campos de ondas registrados con dos receptores distintos. Los mismos autores también realizaron pruebas ultrasónicas en laboratorio para confirmar estas afirmaciones y estipularon que el carácter aleatorio del campo de ondas no es el resultado de la repartición de la fuentes, sino el resultado de la difusión múltiple en un medio heterogéneo. Por lo tanto, la correlación muestra todos los trayectos entre dos puntos, incluyendo aquellos con reflexiones múltiples. Una estipulación similar fue propuesta por Draeger et al. [1995]. Lobkis and Weaver [2001] supusieron que el ruido se compone de todos los modos propios del medio con un mismo nivel de energía, como propusieron también Campillo et al. [1999], Shapiro et al. [2000] y Hennino et al. [2001] con la coda de los terremotos (cf. 1.2.3).

Después de estos resultados experimentales, se desarrollaron diferentes enfoques teóricos para explicar la reconstrucción de la FG; entre ellos, el teorema de fluctuación-disipación [e.g., Godin, 2007, Kubo, 1966, van Tiggelen, 2003, Weaver and Lobkis, 2001, 2003], el teorema de reciprocidad [Wapenaar, 2004] o el teorema de fases estacionarias [Roux et al., 2005b, Snieder, 2004]. Derode et al. [2003a,b] la explicaron gracias al teorema de inversión temporal que veremos más adelante en la sección 2.3, ya que es el más intuitivo y porque se aplica a un medio abierto. Cada uno de estos teoremas difiere en los conceptos utilizados (medio abierto / cerrado, homogéneo / heterogéneo, etc.) así como en las definiciones del ruido (fuente(s) única / multiples / aleatorias, etc.).

Wapenaar [2006] y Godin [2007] estudiaron también el caso particular donde las FFG no son recíprocas (la propagación de A a B difiere de la propagación de B a A) o no elásticas; por lo que no se aplican a la sismología, sino más bien a los fluidos. Snieder [2004] y Roux et al. [2005b] introdujeron el concepto de « zona coherente », refiriéndose a en un medio isótropo, donde las fuentes están repartidas de manera isótropa alrededor de los receptores y donde las fuentes en línea con los receptores tienen mayores contribuciones en cuanto a la reconstrucción de la FG. Existen regiones (en forma de hipérbolas) donde las fuentes tendrán un efecto constructivo en cuanto a la reconstrucción de las FFG. Por otra parte, las fuentes fuera de estas zonas contribuyen de manera aleatoria y entonces se anulan de manera mutua.

A pesar de las numerosas derivaciones teóricas que fueron desarrolladas durante la última década, varios autores señalaron recientemente que en realidad las claves necesarias para el entendimiento de las correlaciones del ruido siempre fueron conocidas desde los trabajos iniciales de Aki [1957], Claerbout [1968] o Cox [1973] y que las propiedades de las correlaciones solo fueron redescubiertas en un nuevo contexto [e.g., Chávez-García and Luzón, 2005, Chávez-García et al., 2005, García-Jerez et al., 2013, Nakahara, 2006, Roux et al., 2005b, Sánchez-Sesma and Campillo, 2006, Sánchez-Sesma et al., 2006]. Por ejemplo, el método SPAC es el antecedente de los métodos de correlación usando el RSA para recuperar la FG [García-Jerez et al., 2013, Tsai and Moschetti, 2010].

2.1.2. Correlación del ruido sísmico ambiental y convergencia hacia la Función de Green

La sismología difiere de las otras aplicaciones que involucran el RSA porque implica el uso de ondas elásticas; al contrario que la acústica donde se consideran solamente ondas escalares. Como se mencionó, la convergencia de la derivada temporal de la correlación cruzada del RSA hacia la FG implica que el campo de ondas sea *equiparticionado* [e.g., Perton et al., 2009, Sánchez-Sesma and Campillo, 2006, Sánchez-Sesma et al., 2006, 2008]. La *equipartición* del campo de onda significa que en el espacio de fase, la energía disponible se distribuye equitativamente, con cantidades promedio fijas, entre todos los estados posibles. Después de un tiempo suficientemente largo, los cocientes de la energía de los modos tienden a estabilizarse a un valor constante [e.g., Ryzhik et al., 1996]. La equipartición de los modos puede obtenerse de dos maneras:

- con la repartición discreta (o localizada) de las fuentes, en un medio heterogéneo; lo que permite a los difusores actuar como fuentes secundarias (Figura 2.1);

- con la repartición aleatoria de las fuentes del ruido primarias.

El primer caso es similar a las características de propagación de la coda sísmica ([Hennino et al., 2001]; cf. 1.2.3), como mostró el trabajo de Campillo and Paul [2003], donde se utilizaron registros de coda de terremotos mexicanos para reconstruir la FG entre dos estaciones sísmicas. Este trabajo inició el campo de investigación de la sismología de las correlaciones y más adelante, Shapiro and Campillo [2004] pudieron obtener ondas superficiales correlacionando el RSA entre estaciones espaciadas de ~100 a ~1000 kilómetros.
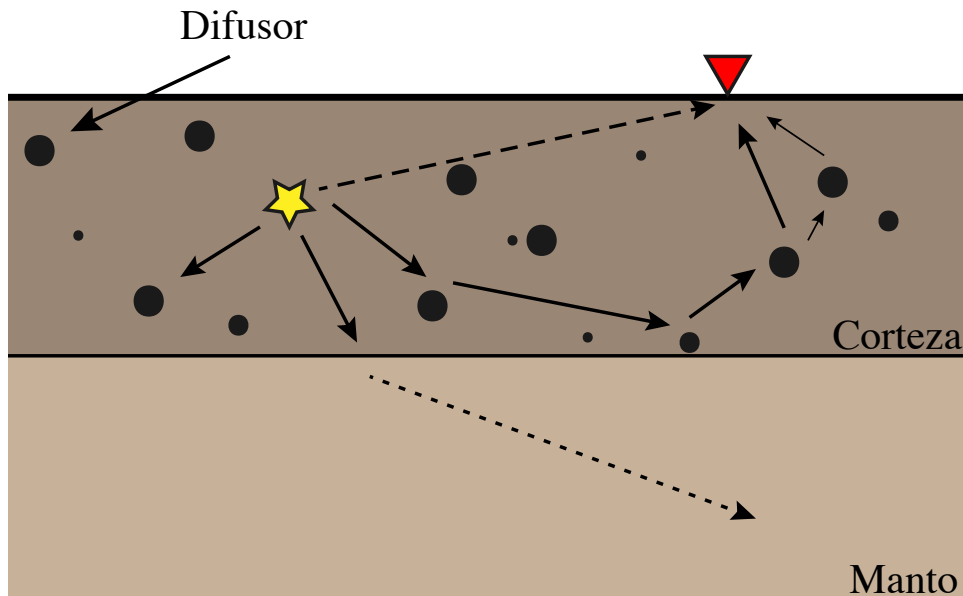
FIGURA 2.1: Esquema sobre el fenómeno de difusión dentro de la corteza terrestre, donde cada vez que una onda encuentra un difusor, cambia de dirección, de fase y de amplitud. Se considera que la sumatoria de todos estos cambios construye un campo de onda isótropo en el receptor. Además, para cada reflexión se produce una conversión de onda a otro tipo de onda. Estos fenómenos conducen a la generación de un campo de onda equiparticionado [Hennino et al., 2001].

La primera aplicación de la técnica de correlación para fines de « tomografía pasiva » (*passive imaging*) fue realizada en California con una resolución espacial sin precedentes [Sabra et al., 2005b, Shapiro et al., 2005]. Para distancias inter-estaciones más pequeñas, Larose et al. [2005] correlacionaron el RSA de datos provenientes del "Apollo Seismic Network" (1969-1972), demostrando así que la técnica es robusta y aplicable en entornos difíciles con datos de baja calidad.

Desde entonces, se realizaron un gran número de estudios tomográficos pasivos a diferentes escalas temporales y espaciales [e.g., Bensen et al., 2009, 2008, Ekström et al., 2009, Fang et al., 2010, Gaite et al., 2012, Gudmundsson et al., 2007, Iglesias et al., 2010, Karplus et al., 2013, Lin et al., 2008, 2009, 2007, Mordret et al., 2013a,b, Moschetti et al., 2010, Nicolson et al., 2012, Nishida et al., 2008, 2009, Pyle et al., 2010, Ritzwoller et al., 2011, Shapiro et al., 2005, Stankiewicz et al., 2012, Stehly et al., 2009, Villaseñor et al., 2007, Yang et al., 2011, 2007, 2008, 2010, Yao et al., 2008, 2006, Zhan et al., 2010] y para diferentes entornos, como en sistemas geotermales [e.g., Calò et al., 2013, Kinnaert et al., 2012, Lehujeur et al., 2013, 2015] y/o en volcanes [Brenguier et al., 2007, Jaxybulatov et al., 2014, Jay et al., 2012, Masterlark et al., 2010, Mordret et al., 2014a, Nagaoka et al., 2012, Stachnik and Dueker, 2006, Stankiewicz et al., 2010]. Sin embargo, la tomografía

en sí no es el objetivo final de las técnica de correlación del RSA, sino que estas ofrecen un gran número de posibilidades para la obtención de información determinista de la Tierra. En efecto, en paralelo a la rápida evolución de las técnicas tomográficas, se han desarrollado también diversas herramientas de monitoreo sísmico [e.g., Clarke et al., 2011, Hadziioannou, 2011, Hadziioannou et al., 2011, 2009, Weaver et al., 2011] para zonas de falla [e.g., Froment et al., 2013, Liu et al., 2014, Minato et al., 2012, Rivet et al., 2014b, 2011, Wegler et al., 2009, Wegler and Sens-Schönfelder, 2007], para volcanes y para sistemas geotermales [e.g., Brenguier et al., 2011, 2008, Duputel et al., 2009, Lecocq et al., 2014, Lesage et al., 2014, Mordret et al., 2010, Rivet et al., 2014a, Sens-Schönfelder and Wegler, 2006], para zonas de instabilidad [Mainsant et al., 2012] o para zonas industriales [e.g., Mordret et al., 2014b, Stähler et al., 2011]. También se ha encontrado una manera eficaz de cuantificar la atenuación sísmica [e.g., Lawrence et al., 2013, Lawrence and Prieto, 2011, Lin and Ritzwoller, 2011, Lin et al., 2012, Prieto et al., 2009, 2011, 2010, Snieder and Larose, 2013, Weaver, 2012, Weemstra et al., 2012, 2014, Zhang and Yang, 2013], lo que tiene enormes implicaciones para la predicción de la repuesta de Tierra frente a un terremoto [Denolle et al., 2013, 2014, Prieto and Beroza, 2008]. Igualmente, después de 25 años (1989), el desarrollo de las correlaciones del RSA permitió desarrollar una teoría para explicar el HVSR (Horizontal-to-Vertical Spectral Ratio, por sus siglas en inglés; cf. sección 2.4.2 y capítulo 5; Sánchez-Sesma et al. [2011]).

2.2. Propiedades de la función de correlación

Al generarse el RSA principalmente en la superficie terrestre (oleaje; cf. 1.3), donde las ondas de superficie son más energéticas, estas ondas dominan la FG reconstruida por correlación cruzada [Shapiro et al., 2005]. Sin embargo, las ondas de volumen ya fueron observadas dentro de las correlaciones del ruido, lo que abrió nuevas posibilidades para cuantificar las propiedades sísmicas de la Tierra profunda [e.g., Poli et al., 2012a,b, Prieto, 2012, Roux et al., 2005a].

En un medio recíproco, las dos partes de la función de correlación (causal y acausal) deberían ser idénticas y simétricas. En la práctica, es raro observar simetría en las correlaciones; e.g., la amplitud de la señal difiere entre la parte causal y acausal (Figura 2.2). Estas asimetrías pueden deberse a varios factores:

- El ruido no es perfectamente isótropo, por lo que presenta una dirección de propagación predominante, por ejemplo de A hacia B. Entonces, la función de correlación tendrá una amplitud más importante en el tiempo positivo. Sin embargo, este tipo de anisotropía puede ser útil para localizar las fuentes del ruido y sus variaciones espacio-temporales, como lo muestra el trabajo de Stehly et al. [2006]. Por otra parte, las variaciones de simetría en fase pueden servir para identificar errores físicos o instrumentales (anisotropía del ruido, errores de reloj, etc.) [e.g., Stehly et al., 2007].

- Las fuentes del ruido no son de la misma naturaleza, por lo que es posible encontrar algunas de ellas con espectros diferentes rodeando a los receptores. En este caso, la función de correlación resultante no será la misma (en fase y amplitud) en la parte positiva y negativa.
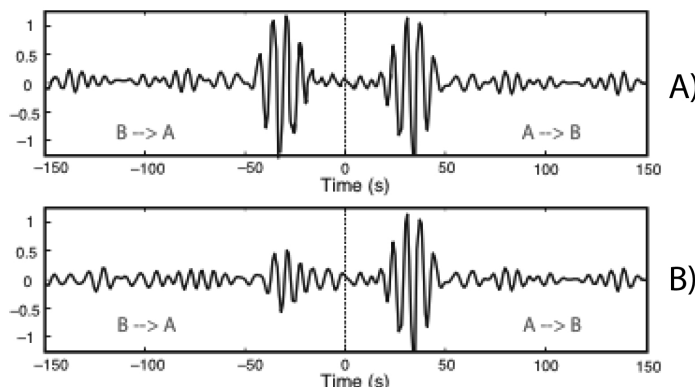
Figura 2.2: Ejemplo de funciones de correlación entre dos puntos A y B. A) distribución homogénea de fuentes; B) distribución de fuentes heterogénea. La asimetría observada en la función de correlación se refleja en un flujo de energía más importante de A hacia B. (modificado de Froment [2011].)

Generalmente se acepta que para fines tomográficos, las funciones de correlación del RSA no pueden ser directamente consideradas como la FG. Sin embargo, haciendo suposiciones simples, es posible determinar cuantitativamente el sesgo entre las correlaciones del ruido y las verdaderas FFG [Campillo et al., 2014].

Para minimizar el efecto de anisotropía de las fuentes, varios autores mostraron que se puede mejorar la equipartición a través de un procesamiento de datos adecuado, con normalizaciones apropiadas [e.g., Bensen et al., 2007, Campillo et al., 2014, Sabra et al., 2005a,b, Weemstra et al., 2014]. Sin embargo, es importante mencionar que varios trabajos numéricos y empíricos señalan que los errores obtenidos en los tiempos de viaje

extraídos desde las funciones de correlación son despreciables ($<1\,\%$) para fines tomográficos [Froment et al., 2010, Garnier and Papanicolaou, 2010, Godin, 2009]. Por ejemplo, Froment et al. [2010] utilizaron las FFG reales obtenidas durante un experimento de exploración sísmica y encontraron una excelente concordancia entre las observaciones y la teoría. Tsai [2009] presentó una derivación de la teoría de rayos que facilita la comprensión de cómo las correlaciones cruzadas del RSA pueden usarse para hacer mediciones directas de los tiempos de viaje. Gracias a un modelo numérico que incluye una distribución no uniforme de las fuentes, una estructura de velocidad heterogénea y ondas que no cumplen perfectamente con la equipartición, el autor logra cuantificar los efectos de la carencia de condiciones ideales en los tiempos de viaje de las mediciones tomográficas.

2.3.   Analogía entre la correlación y la inversión del tiempo

En esta sección se presenta una demostración intuitiva de como la correlación del RSA entre dos puntos A y B puede desembocar en la FG.

Se describe el principio de la inversión del tiempo (reciprocidad) que es una representación aplicable a un medio abierto, homogéneo o heterogéneo [Derode et al., 2003a,b]. La demostración se hace en dos etapas: (I) se demuestra que correlación e inversion del tiempo son dos principios idénticos y; (II) se deduce que una sumatoria de correlaciones converge hacia la FG.

(I) Sea una fuente localizada en F emitiendo una pulsación $e(t)$. La señal registrada en los puntos A y B es la repuesta « impulsional » convolucionada por la función fuente (Figura 2.3: izquierda); es decir, $h_{FA}(t) \otimes e(t)$ y $h_{FB}(t) \otimes e(t)$ respectivamente; donde $\otimes$ simboliza la convolución. Dado que la correlación cruzada puede relacionarse con la convolución de la manera siguiente: $h_{FA}(t) \times h_{FB}(t) = h_{FA}(t) \otimes e(t)\ h_{FB}(-t)$, Por lo tanto, la señal registrada en A y B puede escribirse como:

$$
\begin{aligned}
C_{AB} &= h_{FA}(t) \otimes e(t) \otimes h_{FB}(-t) \otimes e(-t) \\
&= h_{FA}(t) \otimes h_{FB}(-t) \otimes f(t),
\end{aligned}
\tag{2.2}
$$

donde $f(t) = e(t)\ \otimes\ e(-t)$. Si a este resultado le aplicamos una inversión temporal, de tal manera que B es ahora la fuente, el resultado es exactamente como si B produjera una pulsación que fuera registrada en F como $h_{BF}(t)$. Esta señal es invertida en el tiempo

y emitida de nuevo como $h_{BF}(-t)$, lo que es registrado en la estación A como $h_{FA}(t) \otimes h_{BF}(-t)$ (Figura 2.3: derecha). Si el medio es recíproco, es decir en reposo: $h_{BF}(-t) = h_{FB}(-t)$; por lo tanto, la ecuación 2.2 puede también escribirse como: $C_{AB} = h_{FA}(t) \otimes h_{BF}(-t) \otimes f(t)$ [Fink, 1992]; lo que significa que la experiencia es exactamente similar. Esta analogía permite aplicar el teorema de la inversion del tiempo a las correlaciones.
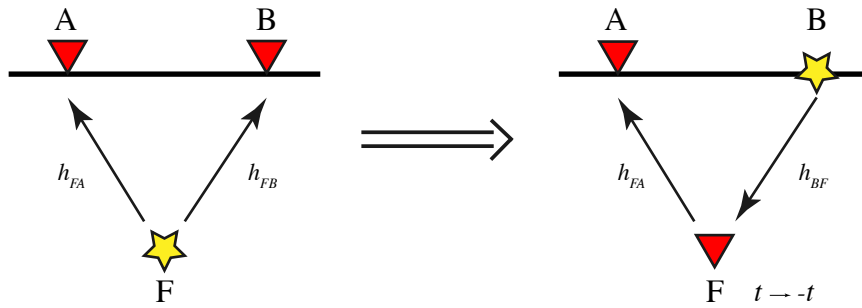
FIGURA 2.3: Esquema de la analogía entre la correlación y la inversión del tiempo (I). Izquierda: correlación de la señal emitida en F y registrada en A y B. Esta operación es exactamente la misma que se representa en la ilustración de la derecha: se emite una señal en B que se registra en F, se le aplica una inversión temporal, es emitida de nuevo y se registra una vez más en A.

(II) Consideramos ahora el caso donde existe un número infinito de fuentes (F) rodeando los receptores A y B (Figura 2.4). En primer lugar A envía una pulsación que se propaga en todas las direcciones del medio ($h_{AF}(t)$), por lo que hay una trayectoria pasando a través de B con una repuesta igual a $h_{AB}(t)$; es decir, la FG entre las estaciones A y B. Las ondas siguen propagándose hacia las fuentes F que, por reciprocidad, vuelven a emitir la señal $h_{AF}(-t)$ hacia la estación A. En este caso, la estación B registra una señal igual a $h_{AB}(-t)$; lo que implica que la FG entre A y B se puede obtener a partir de la correlación de todas las fuentes que rodean a los receptores, con la siguiente expresión:

$$\sum_{fuentes} h_{FA}(t) \otimes h_{BF}(-t) = h_{AB}(t) + h_{AB}(-t). \tag{2.3}$$

Considerando el ruido como ubicuo, podemos inferir que las fuentes rodean los receptores (Figura 2.4). Sin embargo, si las fuentes no rodean perfectamente el medio, todavía es posible estudiarlo con la condición de tener un medio suficientemente heterogéneo y por tanto lleno de « *difusores* » (Figura 2.1). En este caso, los difusores actuan como fuentes secundarias [Derode et al., 2003a,b].
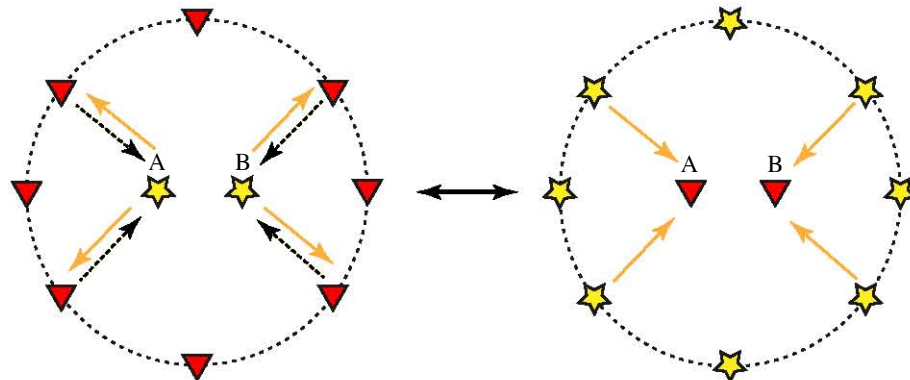
Figura 2.4: Esquema de la analogía entre la correlación y la inversión del tiempo (II). Las dos experiencias son similares. Izquierda: *A* emite una señal que es registrada por todos los receptores a sus alrededor; estos vuelven a emitir la señal que es registrada en *B*. Derecha: correlación de los registros del ruido en *A* y *B* emitidos desde todas las fuentes repartidas homogéneamente alrededor de los receptores.

2.4. Más allá de las correlaciones

El objetivo principal de este trabajo es caracterizar las estructuras volcánicas y para ello se utiliza la tomografía de tiempo de arribo de ondas superficiales extraídas desde las correlaciones cruzadas del RSA. En paralelo al desarrollo de las técnicas de correlación para fines tomográficos, se propusó usar otras técnicas que implican el RSA para aumentar la resolución o el conocimiento de las propiedades físicas terrestres, algunas de las cuales presentan grandes ventajas para el propósito de este trabajo. Las secciones siguientes (2.4.1 y 2.4.2) las describen.

2.4.1. Correlación de Coda de Correlaciones (C_3)

Hasta ahora, solo se ha discutido la reconstrucción de las ondas balísticas por correlación cruzada del ruido ambiental. Sin embargo, la FG obtenida por correlación cruzada también contiene las llegadas tardías asociadas a las ondas difusas [e.g., Derode et al., 2003b]. En otras palabras, la parte final de la correlación del ruido contiene la parte « *coda* » de la FG (cf. 1.2.3). Al respecto, Campillo and Paul [2003] mostraron que es posible correlacionar la parte coda de los sismos para reconstruir la FG. De manera similar, Stehly et al. [2008] propusieron correlacionar la parte coda de las correlaciones del RSA para reconstruir la FG entre pares de estaciones; lo que implica que pueden calcularse las FFG entre pares de estaciones no-concomitantes. Este método se denomina **C**orrelación de **C**oda de **C**orrelaciones o C_3 (Figura 2.5; Stehly et al. [2008]). Posteriormente, varios

estudios mostraron la viabilidad de este método tanto empíricamente [Campillo et al., 2014, Froment, 2011, Froment et al., 2011, Ma and Beroza, 2012, Stehly et al., 2008] como teóricamente [de Ridder et al., 2009, Garnier and Papanicolaou, 2009]. El método C_3 es por lo tanto una alternativa que puede mejorar las mediciones del ruido, sobre todo porque las funciones de correlación son independientes de las fuentes que lo generan [Froment et al., 2011]. Ma and Beroza [2012] demostraron que es posible utilizar el método C_3 para complementar con una red virtual unas estaciones que estuvieron funcionando durante diferentes periodos. En la actualidad el método C_3 todavía tiene un gran potencial inexplorado, ya que ningún estudio tomográfico lo ha aplicado para mejorar la resolución de los resultados.
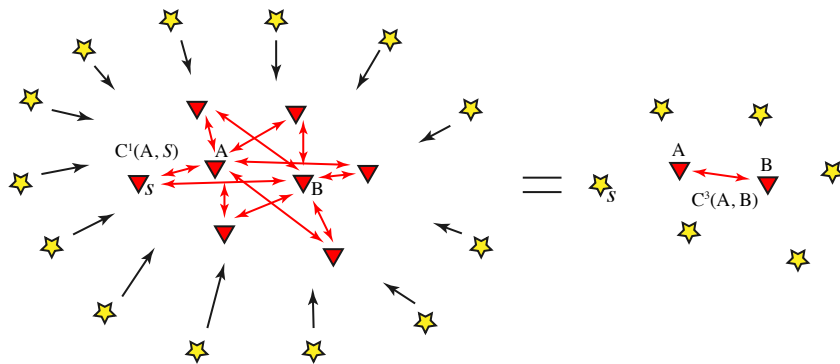
Figura 2.5: Esquema sobre la Correlación de Coda de Correlaciones. Sea una red de N estaciones, la function C^3 entre A y B se obtiene por el apilamiento de todas las correlaciones de coda de correlaciones entre cada par $S - A$:$S - B$ existente y para las partes causales y acausales.

2.4.2. Correlación del ruido y su vínculo con el cociente espectral H/V

El cociente espectral H/V (HVSR) es un método muy popular para determinar la frecuencia natural de un sitio y/o para estimar un modelo de velocidad sencillo (una capa sobre un semi-espacio) debajo de una estación sísmica. Sin embargo, este método siempre ha sido un tópico controversial, ya que carece de base teórica, además de falta de claridad para su interpretación. En realidad, el HVSR ha estado sujeto a una gran cantidad de estudios con el fin de aclarar sus fortalezas y debilidades [e.g., Arai and Tokimatsu, 2004, Cara et al., 2010, Guéguen et al., 2007, Lachetl and Bard, 1994, Lermo and Chávez-García, 1993, Mucciarelli, 1998], así como para determinar la composición del campo de onda del ruido que contribuye a los picos frecuenciales H/V [e.g., Bonnefoy-Claudet et al., 2008, Herak, 2008, Malischewsky and Scherbaum, 2004, Nakamura, 2000].

Sánchez-Sesma et al. [2011] propusieron recientemente una teoría que permite explicar el HVSR. A partir de la teoría del campo difuso [e.g., Perton et al., 2009] (cf. 2.1.2), estos autores sugirieron que el HVSR observado en un receptor puede ser calculado en términos de las partes imaginarias de las FFG, que a su vez, son proporcionales a las densidades de energía direccionales (DED). Entonces, el HVSR puede expresarse de la siguiente manera:

$$\frac{H}{V}(x,\omega) = \sqrt{\frac{Im(G_{11}(x,x,\omega)) + Im(G_{22}(x,x,\omega))}{Im(G_{33}(x,x,\omega))}} = \sqrt{\frac{\langle |u_1(x,\omega)|^2 \rangle + \langle |u_2(x,\omega)|^2 \rangle}{\langle |u_3(x,\omega)|^2 \rangle}},$$
(2.4)

donde $H/V(x,\omega)$ es el HVSR en la estación x para la frecuencia $f = 2\pi\omega$; $G_{ii}(x,x,\omega)$ es la componente de la FG correspondiente al desplazamiento a lo largo de la dirección i, generado por una fuente aplicada en la dirección i, cuando la fuente y el receptor se superponen en x. Im se refiere a la parte imaginaria y los paréntesis $\langle \rangle$ simbolizan el valor promedio. Las direcciones 1 y 2 representan el plano horizontal y la dirección 3, la vertical.

La ecuación 2.4 vincula una sencilla medición del ruido en una estación de 3 componentes a las FFG 1D en un punto x. Por tanto, la ecuación 2.4 permite plantear un problema inverso para evaluar las propiedades físicas del medio bajo la estación sísmica.
En caso de tener una red sísmica poco favorable para la elaboración de una tomografía (ver capítulo 5), la evaluación de los modelos superficiales de velocidad puede plantearse de la forma descrita en este apartado.

2.5. Síntesis

La extracción de información determinista sobre la estructura de la Tierra, gracias a las correlaciones de series de tiempo del ruido abrió nuevas oportunidades y líneas de investigación en sismología. Las correlaciones de RSA fueron ampliamente utilizadas para reconstruir las repuestas impulsionales entre diferentes receptores, lo que llevó al desarrollo del « *passive imaging* ». Aunque las técnicas de correlación tuvieron un importante desarrollo durante la última década, el interés científico para el desarrollo de este enfoque ya existía de tiempo atrás, como lo demuestran los trabajos de Aki [1957] y Claerbout [1968]. De hecho, los mismos principios se han aplicado con éxito en heliosismología [Duvall et al., 1993]. Hoy en día, se conocen bien las técnicas de correlación del ruido RSA y están identificadas una gran parte de sus limitaciones. Sin embargo, queda mucho por

descubrir. Un ejemplo significativo es el reciente descubrimiento, por parte de tres grupos de investigación diferentes, de ondas de volumen telesísmicas dentro de las correlaciones del ruido [Poli et al., 2012a,b, Prieto, 2012, Roux et al., 2005a, Ruigrok et al., 2011]. Otro ejemplo importante es el inicio de tomografías 4-D [Brenguier et al., 2014].

En este trabajo, se muestra como las técnicas de correlación del RSA tienen un gran potencial para la caracterización de la configuración y propiedades físicas del medio volcánico a escala de detalle.

Crustal imaging of western Michoacán and the Jalisco Block, Mexico, from Ambient Seismic Noise

3.1. Resumen

El estudio que se presenta en este capítulo representa la primera aplicación del método de correlación del RSA en un volcán mexicano, el volcán de Colima. Fue planeado como un estudio de prueba, ya que las redes sísmicas que rodean el volcán de Colima son de primera calidad e incluyen un número importante de estaciones de banda ancha. Así, se uasron un total de 78 estaciones sísmicas para producir las imágenes tomográficas del estado de Colima y sus regiones circundantes con alta resolución. Sin embargo, los mapas obtenidos no contienen la información de la profundidad, ya que son calculados por periodos. Para superar esta limitación y poder interpretar los mapas con respecto a la profundidad, se calculó la sensibilidad de la velocidad de las ondas de Rayleigh con respecto a una pequeña variación de velocidad dentro del modelo (i.e. « *sensitivity kernels* »).

Los resultados muestran una zona de baja velocidad profunda y debajo del complejo volcánico de Colima; la cual se enraíza a ∼22 km de profundidad, así como una cámara magmática superficial restringida en los ∼7 primeros km de la corteza. Por otra parte, se observa un sistema de baja velocidad superficial localizado al sur de la falla de Chapala y al oeste del campo volcánico de Michoacán-Guanajuato, que se une por debajo del *rift* de Colima con el sistema volcánico del Colima a unos ∼20 km de profundidad. Este sistema de baja velocidad sigue la geometría de la Faja Volcánica trans-mexicana de manera excepcional. Para profundidades mayores a ∼30 km, las zonas de baja velocidad se paralelizan a la trinchera, justo debajo de los campos volcánicos de la Mascota, Ayutla y Tapalpa; lo que sugiere la presencia de la cuña del manto por encima de la placa de Rivera. Todos los cuerpos de baja velocidad antes mencionados se correlacionan espacialmente con la actividad volcánica superficial; lo que sugiere un posible origen magmático. Se encuentra también una correlación entre las edades de estos cuerpos de baja velocidad y sus respectivas profundidades. Finalmente, se muestra que, a lo largo de la costa las placas Rivera y Cocos subducen con ángulos de buzamiento diferentes.

3.2. Abstract

Detailed crustal imaging of western Michoacán and the Jalisco Block is obtained from ambient noise tomography. Results show a deep and well-delineated volcanic system below the Colima volcano complex, rooting up to 22 km depth, with a shallow magmatic chamber

constrained to the first 7 km. A shallow low-velocity system to the south of the Chapala rift and west of the Michoacán-Guanajuato volcanic field merges, underneath the Colima rift, with the Colima volcano system at about 20 km depth, honoring the geometry of the Trans-Mexican Volcanic Belt. For depths greater than 30 km, low-velocity features become parallel to the slab strike, right beneath the Mascota, Ayutla and Tapalpa volcanic fields, suggesting the presence of the mantle wedge above the Rivera plate. All mentioned low-velocity bodies are spatially correlated with the superficial volcanic activity suggesting their magmatic origin so that, the shallower these bodies, the younger are the associated volcanic deposits. Along the coast, different depths of the uppermost layer of the Rivera and the Cocos plates suggest that the latter plate subducts with an angle 9° steeper than the former.

3.3. Introduction

In western Mexico, the Rivera and the Cocos oceanic plates subduct beneath the North American continental plate (Fig. 3.1). Both oceanic plates have different ages, compositions [e.g., Rosas-Elguera et al., 1996, Schaaf et al., 1995], convergence vectors and subduction angles [Abbott, 2014, Andrews et al., 2011, Kostoglodov and Bandy, 1995, Manea et al., 2006, Pardo and Suárez, 1995, Pérez-Campos et al., 2008, Skinner and Clayton, 2011, Soto et al., 2009, Suhardja, 2013, Taran et al., 2013, Yang et al., 2009]. Five to 10 Ma ago, the Rivera plate that subducts the Jalisco Block detached from the Cocos plate [DeMets and Traylen, 2000], generating an extensional rifting process that separates the Jalisco Block from the North American plate [e.g., Bandy et al., 2000, Ferrari and Rosas-Elguera, 2000]. Although the Jalisco Block is well delineated by the Colima graben to the East and the Tepic-Zacoalco rift to the North (Fig. 3.1), the nature and the exact location of the boundary between both subducting plates are still unclear [e.g., Andrews et al., 2011, Gaviria et al., 2013]. At present, it is believed that the boundary lies beneath the Colima graben on land and the El Gordo graben offshore [e.g., Dougherty et al., 2012, Serrato-Díaz et al., 2004], but the existing uncertainty makes it challenging to understand the dynamic interaction between the Rivera plate and the deformation of the overriding Jalisco Block.

The rifting structures bounding the Jalisco Block along with the subduction process have produced spatio-temporal variations of the volcanism in the Jalisco Block and the western part of the Trans- Mexican Volcanic Belt (TMVB). Geochemical analysis of lava sampled
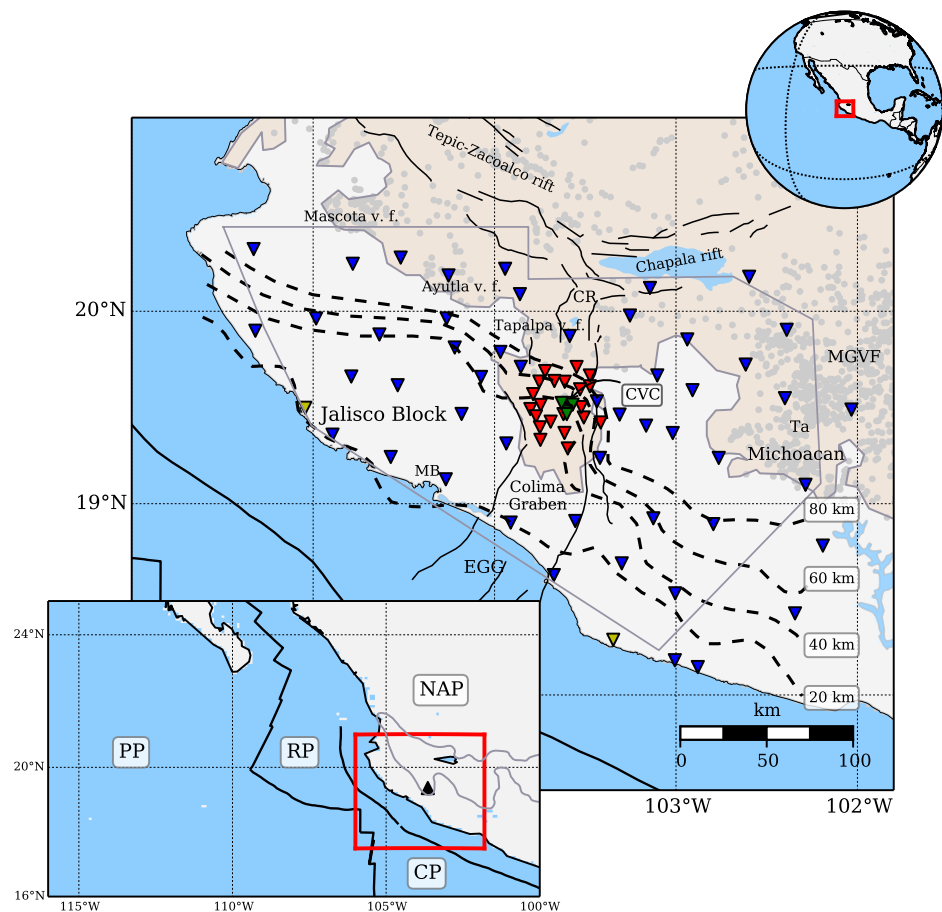
FIGURA 3.1: Tectonic and geologic setting of the study region. Triangles correspond to the seismic stations: MARS (blue); CODEX (red); RESCO (green); SSN (yellow). The study region is delineated by the grey polygon. Gray dots refer to the monogenetic volcanoes (from Ferrari et al. [2011]). The acronyms are as follows: CP, coco plate; CR, Colima rift; CVC, Colima volcanic complex; EGG, El Gordo graben; MB, Manzanillo Bay; MGVF, Michoacan-Guanajuato volcanic field; NAP, North American Plate; PP, Pacific plate; RP, Rivera plate; Ta, Tancítaro stratovolcano. Tectonic features (black lines), the Trans-Mexican Volcanic Belt (sandy colored region) and slab isodepth contours (black dotted lines) are taken from Yang et al. [2009], Ferrari et al. [2011] and Abbott [2014], respectively.

in the region revealed contrasting compositions, including both subduction-related calk-alkaline and intraplate alkaline volcanic signatures [e.g., Ferrari et al., 2000]. Furthermore, the volcanic front in the western TMVB has migrated trenchward from the late Miocene to the Quaternary [Ferrari et al., 2001]. This migration may be related to the steepening of the Rivera plate, due to a reduction of its convergence rate about 8.5 to 6.5 Ma ago [e.g., Pardo and Suárez, 1995] (i.e., a slab rollback; Ferrari et al. [2001]). Although Frey et al. [2007] are skeptical of the trenchward slab migration due to a lack of geological evidence, recent seismological studies support the "rollback theory", which seems to explain a lateral

asthenospheric flow around the slab edges toward the mantle wedge [Ferrari et al., 2011, Soto et al., 2009, Suhardja, 2013, Yang et al., 2009]. Furthermore, shear-waves splitting and P-wave tomographic studies [Soto et al., 2009, Yang et al., 2009] support the idea of a slab gap between the Rivera and the Cocos plates (deeper than 150 km) starting just north of the Colima volcano. This aperture would also allow deep and enriched asthenospheric materials to flow into the mantle wedge. Furthermore, Yang et al. [2009] proposed the existence of a slab detachment in the Rivera plate (about 400 km depth) that allows material to rise and produce a locally warmer mantle wedge. These recent results [Yang et al., 2009] may explain the mixed geochemical signature of the western TMVB basalts. The 'Mapping the Rivera Subduction Zone' (MARS) and the 'Colima Volcano Deep Seismic Experiment' (CODEX) seismic arrays (Fig. 3.1) have significantly contributed to the understanding of the deep structure (i.e., below 80 km depth) and geodynamics of the region. Some authors [Abbott, 2014, Andrews et al., 2011, Taran et al., 2013] suggest that a sharp change in the slab subduction angle takes place beyond 40 km inland from the coast at 35 km depth, so that the Rivera plate becomes steeper than the Cocos plate (dotted lines in Fig. 1). Despite these works, the continental crust is still poorly known. The absence of information responds to the limitations of traditional tomographic techniques based on passive seismology (i.e., earthquake records), which often lack of resolution in the shallow structure due to inadequate ray coverage in the crust. A better understanding of the relationship between the deep geodynamic processes and both seismotectonics and superficial geology (e.g., the active volcanism) requires a detailed description of the crust. To do so, we performed an ambient noise surface wave tomography, which is a technique allowing producing high-resolution images of the upper crust in the absence of earthquakes [e.g., Brenguier et al., 2007, Mordret et al., 2013a, Shapiro et al., 2005, Stankiewicz et al., 2010, Stehly et al., 2009]. The technique retrieves the elastodynamic Green's function (EGF) between pairs of stations in a large frequency range (depending of the seismic network configuration) by cross-correlating the ambient noise time series recorded at the stations [Shapiro and Campillo, 2004, Shapiro et al., 2005, Shen et al., 2012, Weaver, 2005].

In this work, we first explain (Section 3.4) the methodology used to recover the EGFs between concomitant pairs of stations of four seismic networks: (1) the Mapping the Rivera Subduction Zone (MARS) experiment, (2) the Colima Volcano Deep Seismic Experiment (CODEX); (3) the Colima local network (RESCO); and (4) the National Seismological Service (SSN) network. Then we describe how the Rayleigh-wave group velocity measurements were generated from these EGFs (also in Section 3.4) to carry out the crustal
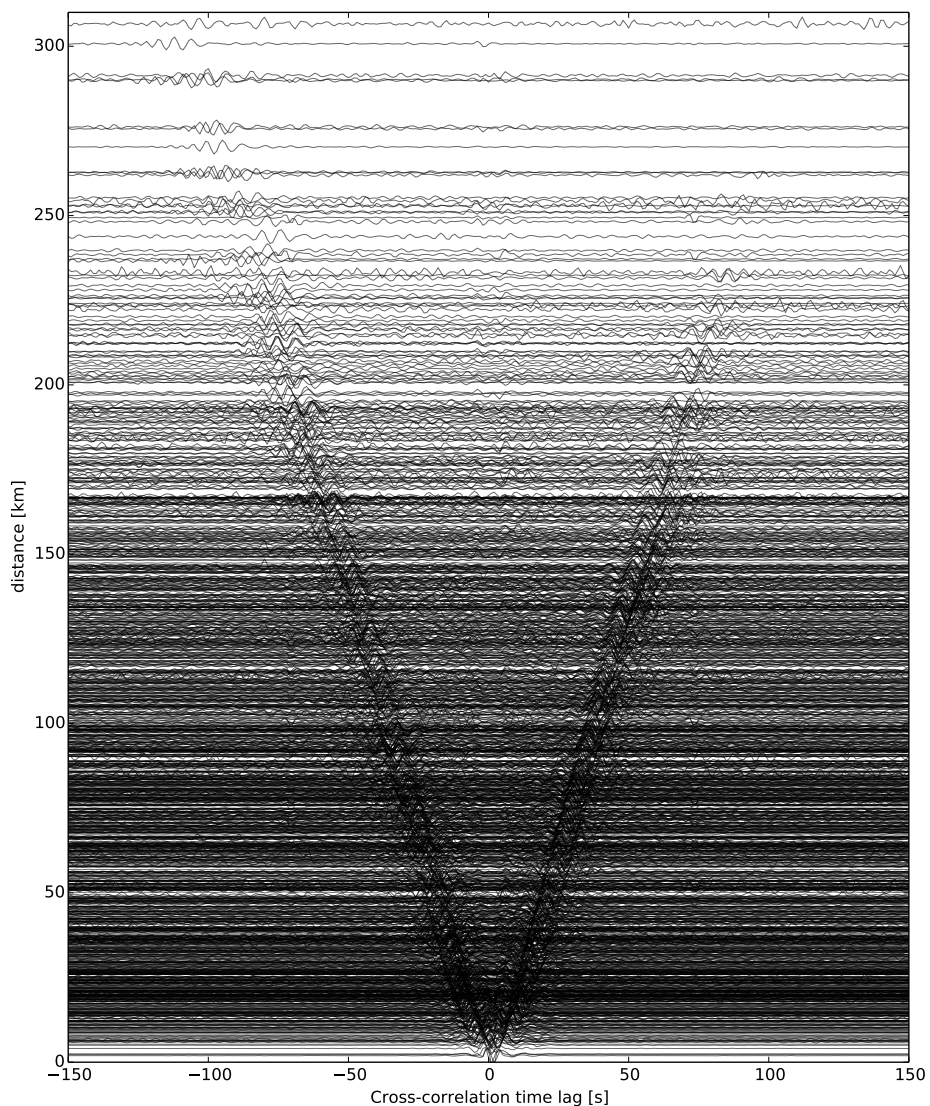
FIGURA 3.2: Band-pass filtered (10 s) EGFs with SNR higher than 15 as a function of inter-station distance.

tomographic imaging (Section 3.5). We finally analyze and interpret the obtained images (Section 3.6) of the upper 35 km across the Jalisco Block and western Michoacán, under the light of previous studies.

3.4. Seismic data processing

The spatial resolution of ambient noise tomography depends on the frequency bandwidth of the seismic measurements and both the density and distribution of the stations. Seismic networks with small inter-station spacing, large footprints and long deployment duration

are appropriate for detailed ambient noise studies [Bensen et al., 2007, Sánchez-Sesma and Campillo, 2006].

In this work, we compiled seismic data from four different networks (Fig. 3.1; MARS, CODEX, RESCO and SSN) that continuously recorded the ground motion. The temporal MARS experiment [Yang et al., 2009] consisted of 50 broadband seismic instruments deployed in southwestern Mexico during 18 months from January 2006 to June 2007. The CODEX experiment, which had a five month overlap with the MARS experiment, consists of 18 short-period seismic instruments deployed in the surroundings of the Colima Volcano.

The RESCO and the SSN permanent networks, have broadband seismometer from which we used continuous records between January 2006 and March 2008. In total, 78 seismic stations were used to obtain vertical component cross-correlation functions (CCFs) for daily time series of all concomitant pairs of stations. We pre-processed the data by down sampling to 20 Hz, removing of the mean, the trend and the instrumental response, followed by a 1- to 40-s band-pass filtering. Temporal (1 bit) and spectral (whitening) normalizations were also applied to diminish the influence of earthquakes and non-stationary noise sources near the stations, but also to broaden the observed frequency band [e.g., Bensen et al., 2007]. The daily CCFs were stacked for

FIGURA 3.3: Examples of Rayleigh-wave dispersion curves. (A) Ray paths over a complete azimuthal range with dispersion curves (color coded) shown in panel B. (B) Dispersion curves for propagation paths shown in panel A. (C) FTAN spectrum (dispersion diagram) for the station pair EFRE-MA11 (thick blue lines in panels A and B).

each station pair to improve the signal-to-noise ratio (SNR). Only CCFs with SNR larger or equal to 15 were used in the study. Forty-six percent of the obtained CCFs were rejected after applying such quality criterion. Fig. 3.2 shows the resulting CCFs as a function of inter-station distance, where a coherent wave train propagating across the network is clearly observed.

To retrieve the EGF between pairs of seismometers, the CCFs were finally folded at the

origin time and stacked to further enhance the SNR and to reduce the effect of sources distribution [e.g., Sabra et al., 2005a]. Since we only considered the vertical component of ground motions, our EGFs are dominated by Rayleigh waves.

From the EGFs, we extracted the surface wave group velocities by means of a frequency time analysis (FTAN) [e.g., Dziewonski et al., 1969]. The FTAN technique applies a set of Gaussian filters with different dominant frequencies to the input-signal spectrum. The arrival times for each frequency band are then estimated from the maxima of the time envelopes (i.e., group velocities). However, the FTAN method leads to systematic errors in the group velocity estimates due to variations in the spectral amplitudes that shift the central frequency toward the origin of the filtered spectrum [Levshin et al., 1989]. This shift was corrected by considering the centroid frequency [Shapiro and Singh, 1999], which is the frequency where the filtered spectrum reaches its maximum. The resulting dispersion curves were visually selected. Only the group travel times for stations separated by more than three wavelengths were accepted [Bensen et al., 2007]. Besides, curves with incoherent dispersion patterns were also rejected (i.e., the group velocity do not vary smoothly with the period) using as a reference the average dispersion curve obtained for the region by Iglesias et al. [2001]. Examples of dispersion curves between the EFRE station at the center of the study region (RESCO network) and many others with a complete azimuthal coverage are shown in Fig. 3.3A and B. Fig. 3.3C also shows an example of FTAN diagram obtained for the station pair EFRE-MA11 (RESCO-MARS; thicker blue lines in Fig. 3.3A and B).

3.5. Group velocity tomography

We obtained Rayleigh-wave group velocity maps from the picked travel times at different periods (i.e., 3, 5, 10, 15, 20 and 25 s) by means of a non-linear iterative 2-D tomographic technique [Rawlinson et al., 2008, Saygin and Kennett, 2010]. At each iteration, the ray paths between stations were updated so that the influence of their length is taken into account to compute theoretical arrival times. This step was carried out by the fast marching method (FMM) [Rawlinson and Sambridge, 2004b, Sethian, 1996]. The FMM is a grid-based Eikonal solver that uses implicit wavefront construction and provides stable and robust solutions for wave propagation in highly heterogeneous media [de Kool et al.,

2006, Rawlinson and Sambridge, 2004b]. The inversion method then seeks for the perturbation of the model parameters that better match the group velocity measurements. Once the perturbations are estimated, the model is updated and propagation paths are retraced using the FMM scheme. In this study, we used the Fast Marching Surface Wave Tomography code developed by N. Rawlinson in the framework of the aforementioned studies.
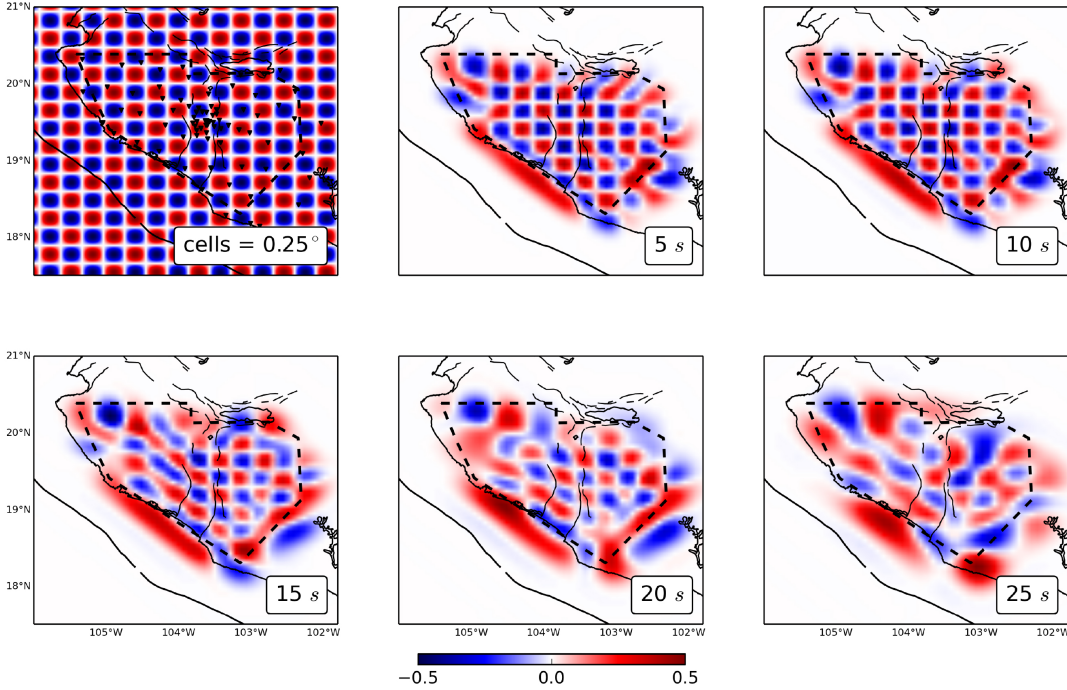
FIGURA 3.4: Checkerboard tests for different periods. The upper-left panel shows the target checkerboard model (i.e., velocity perturbations; color scale). The other panels show the inversion results for 5-, 10-, 15-, 20- and 25-s period. Stations are depicted with black triangles. The black dashed polygon represents the satisfactory-resolution-box. Major tectonic features (black lines) are the same as in Fig. 3.1.

For each period of interest, a set of 2D inversions (i.e., over horizontal planes) was performed from the associated group velocity measurements, using a regular grid with spatial increments of $0{,}18° \times 0{,}16°$ in latitude and longitude, respectively. The inversions were carried out starting with homogeneous velocity models equal to the mean velocity of each set of group speeds observed for the selected period. Based on travel-time misfit values, we used standard L-curve analysis [e.g., Menke, 2012] to determine the optimum weights (in a range of value from 0 to 10,000) for the spatial smoothing and damping.

We performed synthetic checkerboard tests with the available path distribution at different periods to investigate the resolution of our tomographic images. We set an initial 2D problem composed of an alternating pattern of low and high velocity perturbations (i.e., square cells with 25 km per side; Fig. 3.4) and then try to recover the pattern with the
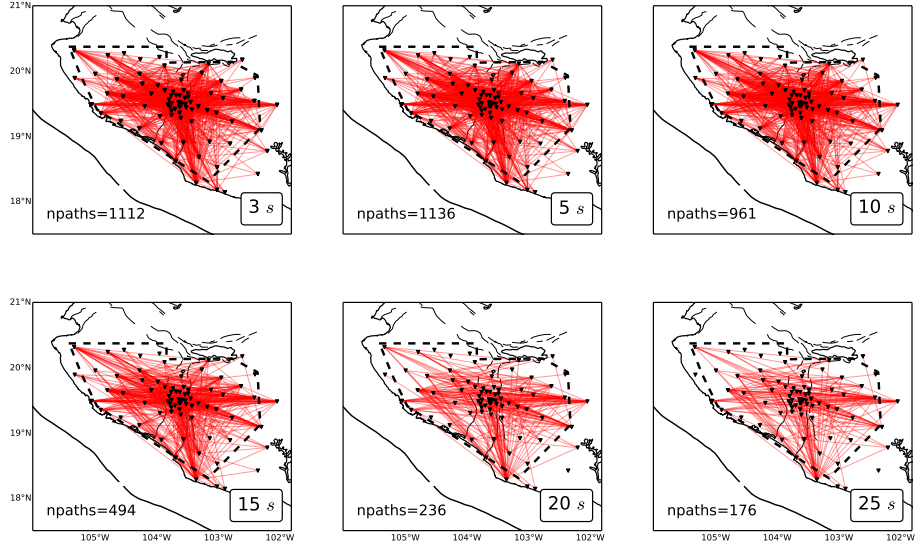
FIGURA 3.5: Ray-path distribution for selected periods (5, 10, 15, 20 and 28 s). The number of rays used in the inversions is given at the bottom of each panel. The stations are depicted with black triangles. The black dashed polygon represents the satisfactory-resolution-box. Major tectonic features (black lines) are the same as in Fig.3.1.

available path coverage for different periods (Fig. 3.5) using the same inversion procedure. The synthetic inversion results are given in Fig. 3.4 and show that the overall recovery of the velocity pattern is good for periods smaller or equal to 20 s. At 25 s, resolution degrades due to a significant reduction of paths density (Fig. 3.5), but it is still possible to extract useful information. A smearing effect is observed in all periods close to the edges of the station ray so that results should be interpreted carefully in these regions. To exclude most of the unresolved zones of the model from our analysis, we defined a "satisfactory-resolution- box" (dashed polygon in Figs. 3.4, 3.5 and 3.6), where our results can be interpreted with fair enough confidence. The box excludes the offshore and east-southeast areas of the model, where the smearing of the checkerboards is evident for all periods.

Checkerboard tests can fail to recover certain kind of velocity anomalies. For example, Lévěque et al. [1993] demonstrated that, for certain path coverage, the tests recover much better small patterns than larger structures. Thus, care should be taken when evaluating the results yielded by this kind of synthetic inversions. An alternative strategy to estimate the resolution consists of analyzing the density of ray paths at different periods (Fig. 3.5).
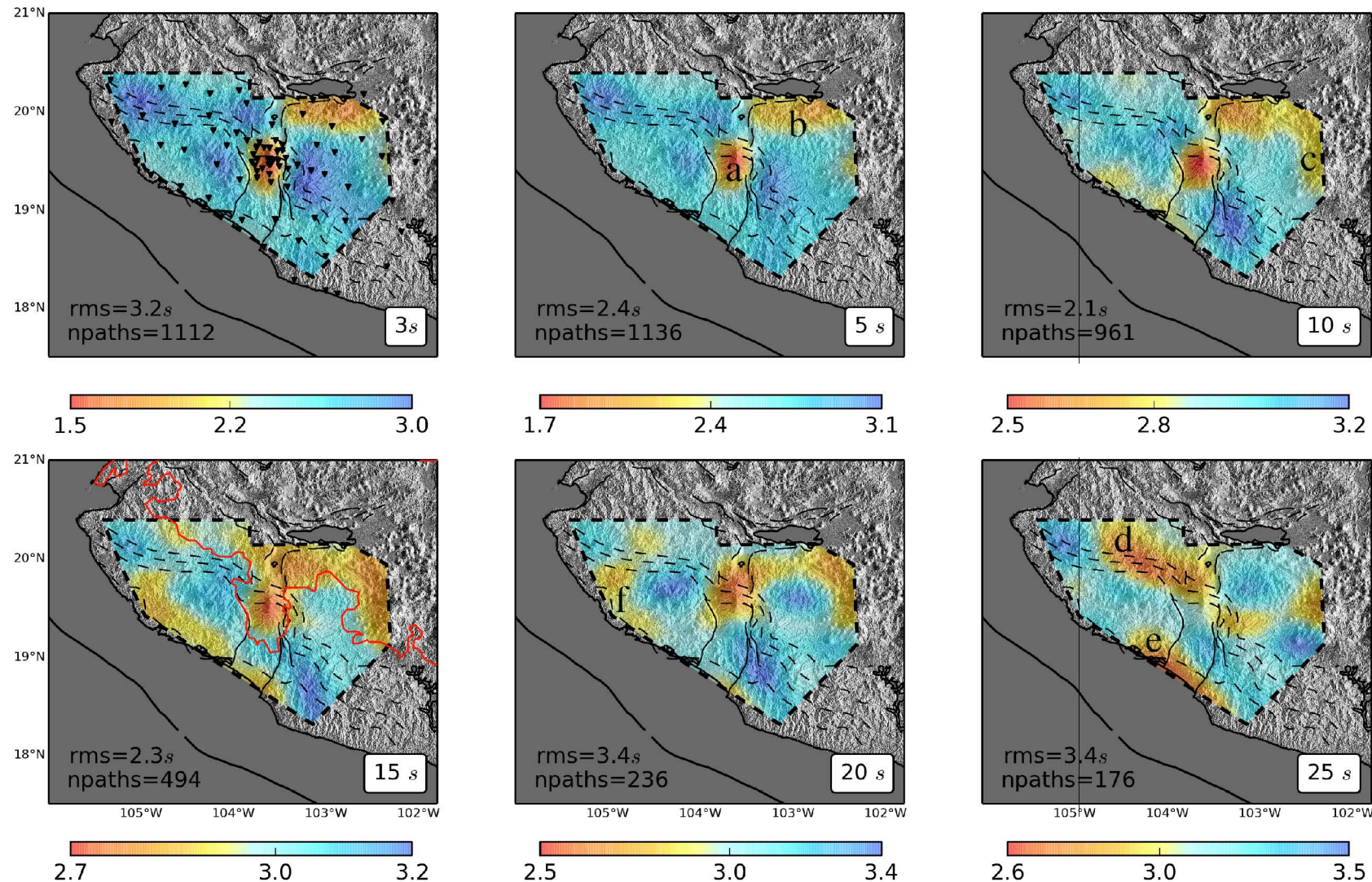
FIGURA 3.6: Rayleigh-wave group velocity tomographic maps yielded by the inversions for selected periods of 3, 5, 10, 15, 20 and 25 s periods. Labels associated to velocity anomalies are referred in the text. The red outline in the 15 s map represents the southern limit of the TMVB. Major tectonic features (black lines) and subducting slab isodepth contours (dotted lines) are the same as in Fig. 3.1.

In our case, a maximum number of 1136 paths were obtained for the shortest period of 5 s. For longer periods, the number of paths gradually decreases down to a minimum value of 176 for the longest period of 25 s. The best-fitting Rayleigh-wave group velocities maps are shown in Fig. 3.6 along with their associated rms travel-time residuals.

3.6. Results and discussion

In order to assess the depth-range sampled in each tomographic map, we computed sensitivity kernels for the Rayleigh-wave fundamental mode [Herrmann, 1996] at the periods shown in Figs. 3.4, 3.5 and 3.6. Since our study area encompasses different geological settings, to compute the kernels we chose two distinct velocity structures obtained for the region: (1) a model determined beneath the Popocatépetl volcano [Cruz-Atienza et al., 2001],which includes both the superficial volcanic deposits associated to the TMVB and a low-velocity zone associated to the volcano magma chamber; and (2) a typical crustal model determined along the coast in southern Mexico [Iglesias et al., 2001] (middle panel, Fig. 3.7). The kernels (left panel, Fig. 3.7) reveal the sensitivity of the surface waves to small perturbations in depth for the model elastic properties [Aki and Richards, 2002]. Their maxima indicate the depths where the corresponding eigenfunctions are primarily determined by the model. The right panel of Fig. 3.7 shows the depth ranges where sensitivity is higher than 85 % of the maximum values. As expected, the longer the period of the surface waves, the larger is the range of depths with similar sensitivity. From now on, attributed depths in the discussion and conclusion sections are based on these estimates.

3.6.1. The Colima volcano complex

The most striking feature in Fig. 3.6 for all periods is a low-velocity zone below the Colima volcano (denoted as "a" in the 5 s map of Fig. 3.6). For the 3- and 5-s period maps (i.e., above 7 km depth), we find very low group velocities of 1.6 km/s. Although no physical characterization can be directly inferred from our measurements, we naturally associate this zone to the presence of the shallow-crust magma body responsible of the current Colima volcano activity [e.g., Lees, 2007]. Similar observations were obtained for group velocity maps at Yellowstone [Stachnik et al., 2008] and beneath the Toba caldera [Stankiewicz et al., 2010]. Although numerous geophysical studies have been done in the
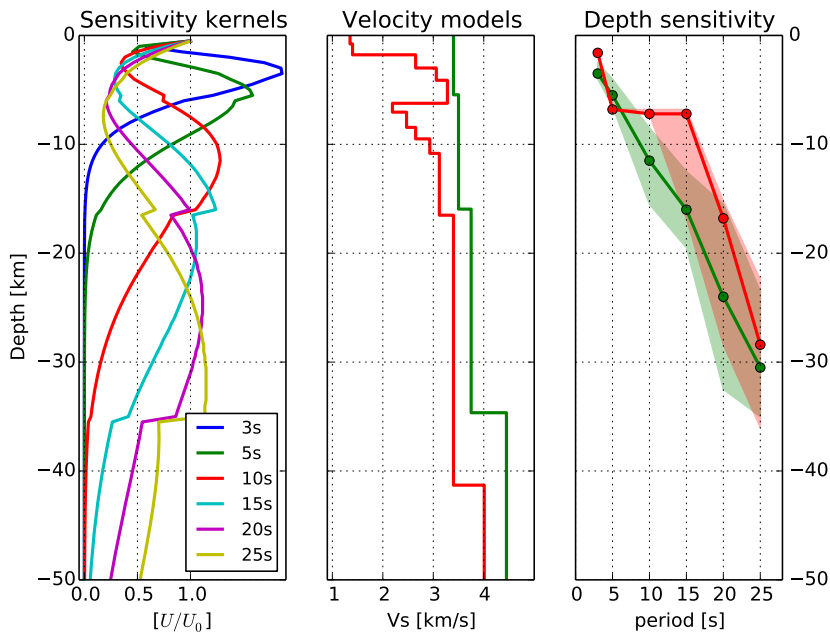
FIGURA 3.7: Left: sensitivity kernels obtained for the velocity model by Iglesias et al. [2001]; middle: velocity models (green: Iglesias et al. [2001]; red: Cruz-Atienza et al. [2001]); right: maximum sensitivity depths (dots) for both models (same colors that middle panel) and associated ranges with 85 % sensitivity (shaded zones).

CVC, no clear evidence of the Colima volcano magma chamber has ever been reported [e.g., López-Loera, 2012, Medina-Martínez et al., 1996, Zobin et al., 2002]. This work confirms the presence of a magma chamber above 7 km depth and provides insights of its horizontal geometry (i.e., lengths of about 30 km in the east-west direction and about 50 km in the north-south graben axis), suggesting a structural control of the Colima graben fault system. Furthermore, although with higher group velocities (i.e., 2.5 km/s), the CVC low-velocity body extends downward, rooting up to 22 km depth (i.e., 20-s period) roughly below the volcano. This suggests the existence of a magma conduit allowing the molten material to rise from the deep crust and thus the existence of a magma reservoir at these depths, as proposed by Vigouroux et al. [2008]. The existence of such conduit could be a consequence of the fracturing associated to the Colima graben, which facilitates the fluids rising from the subducted slab [e.g., Luhr, 1992].

3.6.2. The Michoacán-Guanajuato volcanic field

Another prominent east-west trending low-velocity feature appears to the south of the Chapala rift within the first 7 km (i.e., for periods of 3 and 5 s). Such isolated body

(denoted as "b" in the 5 s map of Fig. 3.6) then merges with a deeper system to the southeast (denoted as "c" in the 10 s map of Fig. 3.6) at depths larger than 10 km, spreading all over the Michoacán-Guanajuato volcanic field (MGVF; i.e., beneath the Tancítaro volcano). Deeper, around 17–24 km depth (i.e., 15- and 20-s periods), the CVC and MGVF low-velocity bodies merge beneath the Colima rift, forming a horseshoe-like feature remarkably delineated by the southernmost edge of the TMVB (red line in the 15 s map of Fig. 3.6). The moderate group velocities of this large structure (around 2.7 km/s) and its spatial correlation with the monogenetic volcanism (gray dots in Fig. 3.1) indicate that the body may have a magmatic origin. Indeed, such a low-velocity zone may be the consequence of the slab dehydration, which promotes the accretion of deep magma bodies such as large batholiths. The connection between the CVC magmatic system and the MGVF low-velocity structure at 22 km depth suggests either a deep source of magma mixing, as revealed by the anomalous enrichments of compatible trace elements in Colima andesites [e.g., Luhr and Carmichael, 1980], or the existence of a common magma source at that depth.

3.6.3. The Rivera plate mantle wedge

Deeper than 30 km(i.e., 25 s), although a low-velocity root remains below the Tancítaro-Paricutín volcanoes, most of low-velocity features migrate to the northwest of the CVC describing an elongated slab parallel body, right beneath the monogenetic Mascota, Ayutla and Tapalpa volcanic fields (MATVF; denoted as "d" in the 25 s map of Fig. 3.6). Considering both the Rivera slab geometry below the body, which abruptly increases its depth from 40 to 80 km (dashed lines in Fig. 3.6) [Abbott, 2014, Suhardja, 2013], and the thickness of the continental crust of 35 km [Ferrari et al., 2011] and references therein; [Suhardja, 2013], this low-velocity body may correspond to the mantle wedge above the Rivera plate. Indeed, the water release from the subducting slab serpentinizes the mantle wedge [e.g., Bostock et al., 2002], producing lower velocity anomalies as compared to the surrounding crustal minerals [Christensen, 1996]. This phenomenon is accentuated by the steeper subduction angle of the Rivera plate, which induces a mantle wedge thickening away from the slab. Actually, by means of receiver function analysis, Suhardja [2013] inferred a serpentinized mantel wedge above the Rivera plate at distances of 80 to 100 km from the coast, which is consistent with our results (Fig. 3.6).

3.6.4. Volcanic deposits

The spatial correlation between the low-velocity bodies and the superficial volcanic activity is one of the most noticeable results of this study. The correlation is clear below (1) the Colima volcano in the center of the study area, (2) the Colima and south of the Chapala rifts to the north and northeast, (3) the MGVF to the east and (4) the MATVF to the northwest. Yet, depending on their locations, the correlation appears at different depths so that the shallower the low-velocity body, the younger are the associated volcanic deposits. For instance, in the currently active Colima volcano, we find the low-velocity anomaly above 3 km depth (i.e., 3-s period). In the MGVF, where a low-velocity anomaly appears deeper, below 10 km depth (i.e., 10-s period), the volcanism started in the late Pliocene (2.78 Ma) [e.g., Gómez-Tuena et al., 2007] and the volume of material erupted in the last 40,000 years has been an order of magnitude less than the Colima stratovolcano [Ferrari et al., 2011]. Moreover, in the MATVF, we find both the oldest lavas in the region with early Pliocene ages ranging from 4.5 to 4.69 Ma [e.g., Gómez-Tuena et al., 2007] and the deepest low-velocity body that probably reaches the mantle wedge, around 30 km depth (i.e., 25-s period). These observations strongly suggest that all mentioned low-velocity bodies have a magmatic origin and then may be responsible of the volcanisms in the entire region.

3.6.5. The subducting slab

An along-coast 30 km width low-velocity zone appears around 28 km depth (i.e., 25-s period) primarily to the southeast of Manzanillo bay (denoted as "e" in the 25 s map of Fig. 3.6). Considering the geometry of the Cocos plate [Abbott, 2014], this body may correspond to the transition from continental to oceanic crusts. Although subducted basalts are generally observed in tomographic studies with higher velocities than the surrounding materials [e.g., Kárason and Van Der Hilst, 2000], recent studies concluded that the basalts may contain pervasive water and/or water-saturated oceanic sediments with low velocities at the very top of the slab [Audet et al., 2009]. We thus interpret such low-velocity zone as the uppermost layer of the Cocos plate. This observation has also been done in the region by Suhardja [2013] and to the east, in the Guerrero segment of the Cocos plate [e.g., Pérez-Campos et al., 2008]. Shallower, around15 km depth (i.e., 15- and 20-s periods), the low-velocity zone appears to the northwest of the bay (denoted as "f" in the

20 s map of Fig. 3.6), possibly indicating the presence of the corresponding uppermost layer of the Rivera plate. These observations suggest that the Cocos plate subducts with a steeper angle than the Rivera plate beneath the first 30 km from the coast (i.e., with a slope 9° steeper ifwe assume a depth difference of 13 km between the plates at 80 km from the trench). This result is also in agreement with recent geophysical and geochemical studies [Abbott, 2014, Andrews et al., 2011, Taran et al., 2013] and joints both the idea of the slab tear between the subducting plates somewhere beneath Manzanillo bay and the hypothesis of the slab detachment in the region [e.g., Suhardja, 2013, Yang et al., 2009] that would allow the asthenosphere to rise above the plates to feed the Colima volcano. Some of the interpretations of Sections 3.6.3, 3.6.4 and 3.6.5 are based on the 25 s tomographic map (Fig. 3.6). Even though the ray-path density at this period is the lowest (Fig. 3.5) and that smearing effects appeared in the associated checkerboard test (Fig. 3.4), we believe that our results are reliable enough to put forward the interpretations.

3.7. Conclusions

Detailed imaging of the crust was obtained across the Jalisco Block and western Michoacán from a Rayleigh-wave group velocity tomography by means of ambient noise cross correlations. Ambient noise tomography was performed using records of 78 seismic stations providing high-resolution images from 2 to 35 km depth. Results robustly show a deep and well-delineated volcanic system below the Colima volcano rooting up to 22 km depth. Seismic evidence of low velocities in the upper 7 km indicates the presence of a shallow magmatic chamber associated to a larger geothermal system limited by the Colima graben fault system in the east-west direction. An independent east-west trending low-velocity zone to the south of the Chapala rift and west of the MGVF (i.e., beneath the Tancítaro-Paricutín volcanoes) spans up to 15 km depth and then merges, underneath the Colima rift, with the CVC low-velocity body at about 20 km depth. Such large horseshoe shaped feature is perfectly delineated by the southernmost edge of the Trans-Mexican Volcanic Belt. For depths greater than 30 km, low-velocity features become parallel to the slab strike, right beneath the MATFV to the northwest of the CVC, suggesting the presence of the serpentinized mantle wedge above the Rivera plate. Our results also show a spatial correlation between the low-velocity bodies in the region and the superficial volcanic activity. The correlation depends on both, the age of the associated deposits and the

location of the bodies. We concluded that the age of volcanism along the Trans-Mexican Volcanic front in its western sector is directly correlated with depth of the low-velocity bodies, so that the shallower the bodies, the younger are the volcanic deposits. This strongly suggests that the low-velocity anomalies have a magmatic origin probably responsible of the overriding volcanism.

On the other hand, an along-coast 30 km width low-velocity region to the southeast of the Manzanillo bay appears around 28 km depth. We interpret this region as the uppermost layer of the Cocos plate. Shallower, around 15 km depth, the low-velocity zone appears to the northwest of the bay, probably revealing the corresponding uppermost layer of the Rivera plate. These observations suggest that the Cocos plate subducts with an angle 9° steeper than the Rivera plate and thus support the idea of the slab tear between both plates somewhere beneath Manzanillo, as suggested by previous works.

3.8. Acknowledgments

Hydrothermal and Magmatic Reservoirs at Lazufre Volcanic Area, Revealed by a High-Resolution Seismic Noise Tomography

4.1. Resumen

En la zona del Lazufre se observa uno de los levantamientos corticales más grande del mundo. En el periodo ente 1998 a 2000, Pritchard and Simons [2004] observaron una tasa de deformación máxima igual a 1 cm/año, afectando un área de ∼2000 km^2. Hoy en día, la deformación sigue produciéndose con una tasa máxima del orden de 3 cm/año, para una superficie de 2700 km^2 [e.g., Remy et al., 2014]. Adicionalmente, una segunda deformación, de menor amplitud, se observó justo debajo del volcán Lastarria [Froger et al., 2007]. Las localizaciones, las formas, así como la caracterización de las fuentes que generan ambos levantamientos corticales no pudieron ser definidos de forma precisa por estudios previos de modelación InSAR y GPS. Además, existe incertidumbre sobre el origen de la doble firma geoquímica magmático-hidrotermal de los gases volcánicos del Lastarria [Aguilera et al., 2012]. Los resultados proporcionados por este estudio mejoran la comprensión de los fenómenos previamente mencionados.

El estudio utilizó datos sísmicos de dos redes de sensores instalados durante diferentes periodos de tiempo entre 2007 y 2012 para llevar a cabo un modelo de velocidad de alta resolución de las ondas S en 3-D. Este modelo de velocidad permitió determinar por primera vez la geometría y la ubicación de la fuente de la deformación cortical observada en el volcán Lastarria, ya que pone en evidencia tres anomalías de baja velocidad. Dos de ellas están localizadas debajo del volcán Lastarria y tienen velocidades de las ondas S entre 1.2-1.8 km/s. La más superficial se encuentra en el primer kilometro de la corteza, mientras que la más profunda tiene velocidades aún más bajas y está ubicada entre 3 y 6 km de profundidad. Ambas anomalías tienen forma elíptica con el eje mayor orientado en la dirección E-W y están separadas por un un zona de 2-3 km con velocidades de las ondas S entre 1.5-2 km/s. Debido a que estas anomalías de velocidad están ubicadas debajo del campo fumarólico del volcán Lastarria, se interpretaron como un cámara magmática (anomalía profunda) que coexiste con un sistema hidrotermal (anomalía somera), resultado de la desgasificación de la cámara magmática. Esta interpretación está en concordancia con estudios previos de geoquímica, de deformación (GPS y InSAR) y magneto-telúricos realizados en el área; y en particular, permite explicar el doble origen de los gases (hidrotermales y magmáticos). La tercera zona de baja velocidad, con velocidades de ondas S aproximadamente de 2,3 km/s está ubicada a 5 km de profundidad y se encuentra debajo de la zona de deformación de gran amplitud previamente determinada por análisis InSAR. Finalmente, se compararon las tomografías obtenidas con los resultados InSAR

para proponer que esta zona de baja velocidad podría corresponder a una zona rica en fluidos hidrotermales y posiblemente en magma.

4.2. Abstract

We determine here for the first time the geometry and location of the hydrothermal and magmatic reservoirs in the Lazufre volcanic area. This furthers the understanding of the origin of one of the largest worldwide volcanic uplift regions, both in space and amplitude. The exact locations and shapes of the sources generating a double-wide uplift region in the Lazufre found by past deformation data (InSAR and GPS) and generating hydrothermal and magmatic fluids found by geochemical gas analysis have not been well-delimited. In this study, we use seismological data to perform a 3-D high-resolution S-wave velocity model, which allows defining better the locations and shapes of the sources of the deformations and the hydrothermal and magmatic reservoirs. We find three anomalies. Two of them (with S-wave velocity of about 1.2-1.8 km/s) are located below the Lastarria volcano. The shallow one (<1 km below the volcano base) has a funnel-like shape. The deeper one is located between a depth of 3 and 6 km below the volcano base. Both are strongly elliptical in an EW direction and separated by a 2-3 km thick zone with V_S of 1.5-2 km/s. As far as these anomalies are located under the hydrothermal activity of Lastarria volcano, they are interpreted as a double hydrothermal (the shallow part) and magmatic source (the deeper part). The later can feed the former. This double hydrothermal and magmatic source is in agreement with previous geochemical, deformation (GPS and In-SAR) and magneto-telluric studies. In particular, it explains the double origin of the gases (hydrothermal and magmatic). The third low-velocity zone (with S-wave velocity of about 2.3 km/s) located at 5 km depth and deeper is centered beneath an area of surface uplift as determined by InSAR data. We compare the seismic tomography and InSAR results to propose that this low-velocity zone is at the top of a large reservoir, hosting hydrothermal fluids and possibly also magma.

4.3. Introduction

Knowledge of volcanic-reservoir geometry, location and strength is of major importance in monitoring and understanding volcanic unrest. Volcanic reservoirs include magmatic

and hydrothermal storage zones and may feed volcanic eruptions when molten material and/or gases reach the surface or a secondary magma reservoir. The depth of a magma reservoir is controlled by a complex association of factors such as the regional stress regime, the magma density, viscosity, volatile content, crystal content or the local crustal structure. In extensional, transtensional, transpressional or strike-slip contexts, the magma reservoirs are generally shallow (between the sub-surface and about 5 km depth) whereas in compressional settings, the magma reservoirs are found to be deeper, without shallow magma reservoirs [e.g., Chaussard and Amelung, 2012, Pritchard and Simons, 2004]. These factors also influence the behavior of a volcanic eruption since they control the pressure-temperature condition of the magma reservoir [Chaussard and Amelung, 2012, Dzurisin, 2006]. Hence it is important to know if andesitic volcanoes can have shallow reservoirs and we take the Lastarria volcano as a study example. Direct and convincing seismic images of the geometry and properties of volcano reservoirs are rare [Marsh, 2000]. This is due to the fact that traditional seismic tomography, based on earthquake data, is not adequate for obtaining high resolution images of the shallow crust where small magma chambers, dykes or sills are expected [e.g., Lees, 2007]. It is particularly true when the number of earthquakes used is small or when the seismograms are difficult to read due to strong path/site effects.

 The problem of having a fewer earthquakes can be easily solved with another technique: the ambient seismic-noise tomography (ANT). The ANT technique can produce high-resolution images of the upper crust [e.g., Shapiro et al., 2005], without earthquakes. The technique allows the retrieval of Green's function between pairs of seismometers by cross-correlating the ambient noise recorded at each of them [Shapiro and Campillo, 2004]. ANT techniques have successfully been applied to reveal different geological structures at global, regional and local scales using only a few hours to a few months of continuous seismic noise [e.g., Bensen et al., 2007, Brenguier et al., 2007, Mordret et al., 2013a, Shapiro et al., 2005]. This technique has also been successfully applied to obtain images of volcanic structures, being especially promising for imaging volcano reservoirs at unprecedented resolution, for instance at: the Piton de la Fournaise volcano (Reunion Island; Brenguier et al. [2007], Mordret et al. [2014a]), the Okmok volcano (Alaska, U.S.A; Masterlark et al. [2010]), the Toba volcano (Sumatra, Indonesia; Jaxybulatov et al. [2014], Stankiewicz et al. [2010]), the Uturuncu volcano (Bolivia; Jay et al. [2012]), Mount Asama (Japan; Nagaoka et al. [2012]) and at the Colima Volcano (Mexico; Spica et al. [2014]).
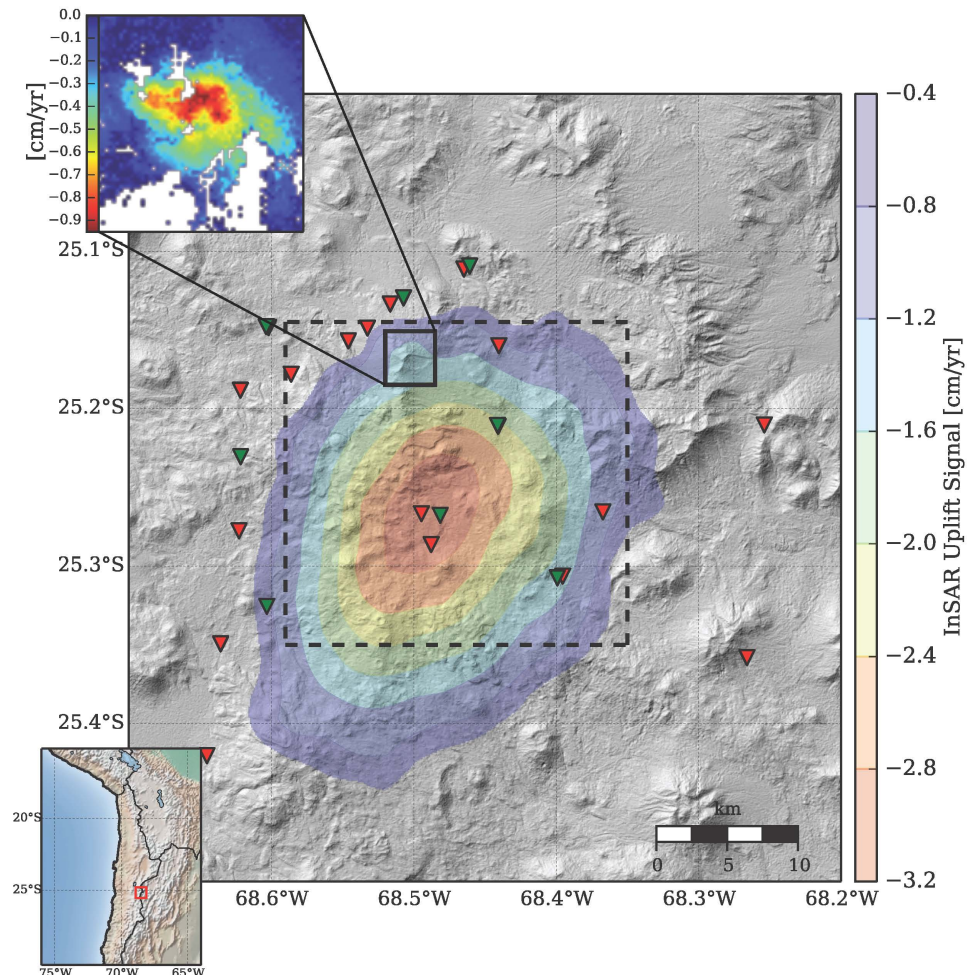
FIGURA 4.1: SRTM-based shaded relief map of the Lazufre volcanic area along with the deformation area (from Froger et al. [2007]) and the location of seismic stations sites. Red and blue reversed triangles are the seismic station from network I and network II, respectively (see text for details). Upper corner left: InSAR signal on Lastarria (from Froger et al. [2007]) volcano is referred with the plain line rectangle on the map. The dashed-line-square is the contour of the satisfactory-resolution-box.

The Lazufre (an acronym for Lastarria and Cordón del Azufre) area [Pritchard and Simons, 2002] is one of the largest uplift deformation areas in the world [Ruch et al., 2008], located in the Altiplano-Puna Plateau in the central Andes (Chile-Argentina). An area of 2000 km2 started inflating between 1997 and 2000 [Froger et al., 2007, Pritchard and Simons, 2002, Ruch et al., 2009] related to an over-pressurized source at depth. Basaltic volcanoes generally show such uplifts before eruptions [e.g., Lu et al., 2010, Wicks et al., 2002], but it is not clear it is the case for andesitic volcanoes [Chaussard and Amelung, 2012, Fournier et al., 2010, Pritchard and Simons, 2004]. A few questions are still unsolved. Geodetic data showed the existence of two sources of deformation (a shallow one and a deep one), but with inaccurate shape and location. The depth of the deep source is not

well constrained since it is modeled somewhere between 7 and 18 km [Anderssohn et al., 2009, Froger et al., 2007, Henderson and Pritchard, 2013, Pearse and Lundgren, 2013, Pritchard and Simons, 2004, Ruch et al., 2008] and re-estimated to be between 2 and 14 km by Remy et al. [2014]. Hence, the depth of this source may be between 2 and 18 km. These errors are due to the trade-off between the pressure, the shape of the source and the depth. The shallower source was supposed to be unique, at a depth of about 1 km and located just beneath the Lastarria volcano [Froger et al., 2007, Ruch et al., 2009]. We show in this study that this source double. Furthermore, these geodetic data cannot discriminate between a hydrothermal and a magmatic system below the Lastarria volcano, as is suggested by geochemical studies.

In this study, we perform a high-resolution 3-D ANT, using data from 26 mainly broadband seismic stations recorded at two different seismic networks deployed at Lazufre. The location and geometry of hydrothermal and magmatic reservoirs below the Lazufre volcanic area are deduced through S-wave velocity tomographic images obtained from the ANT. Results are compared to source inversions from InSAR and GPS data [Anderssohn et al., 2009, Froger et al., 2007, Pearse and Lundgren, 2013, Pritchard and Simons, 2002, 2004, Remy et al., 2014, Ruch et al., 2008, 2009]. As the geometry and the depth of the sources of these deformations cannot be well and uniquely determined with only the InSAR and GPS deformation field, it is important to image these sources with independent data, such as seismicity.

4.4. Data and methods

4.4.1. Data

The data used in this study come from two temporary seismic networks installed during two distinct time periods. Network 1 (red triangles in Figure 4.1) was deployed from 1 February to 26 March 2008 by the GFZ (Germany) and the DGF (Chile). It was composed of 18 seismometers: 17 broadband (12 Guralp CMG3ESP -60 s- and five Trillium T40 -40 s-) and one short period (LE-3D -1 s-), covering the main deformation zone at Lazufre. Network 2 (blue triangles in Figure 4.1) was deployed from November 2011 to March 2013 by the University of Alaska Fairbanks in the framework of the PLUTONS project, but we used only the data from January to March 2012 for this network. Network

2 was composed of eight broadband seismometers (six CMG3T -120 s- and two CMG6TD -30 s-). All seismometers (Figure 4.1) were GPS-time synchronized.

The next paragraphs describe the procedures of how the Rayleigh-wave group velocities were obtained from continuous seismic noise records in order to perform an S-wave tomography later.

4.4.2.   Reconstruction of Green's functions from seismic noise

The following steps were applied on the vertical components of each individual continuous seismic data: (1) a removal of the mean and the trend of the signal; (2) a down-sampling to 20 Hz; (3) an instrumental response correction; (4) a 1-30 s band-pass filter; (5) a temporal (1-bit) normalization; (6) and a spectral (whitening) normalization. Steps (5) and (6) were applied in order to diminish the influence of earthquakes and/or non-stationary noise sources at the vicinity of the seismometer. These normalizations allowed using a larger frequency band [e.g., Bensen et al., 2007] and diminishing the influence of heterogeneous distribution of noise sources. Then, cross-correlation functions (CCFs) were calculated for the vertical components of all concomitant station pairs (181) on 200 seconds time windows. The duration of 200 seconds was chosen because we found that if a particular station would have a punctual instrumental failure, only a 200 s time window of signal would have been lost. We then stacked all available 200 s CCFs for a given station-pair and added the positive and negative parts of the CCF to enhance the signal-to-noise ratio and to reduce the effect of the heterogeneous distribution of the sources [e.g., Bensen et al., 2007, Sabra et al., 2005a]. Each folded and stacked CCF converged towards the estimated Green's function (EGF) between each pair of seismometers. Only the EGFs with a signal-to-noise ratio greater than 8 (value that has been found to give the best associated dispersive curves) were used for further analysis. The signal-to-noise ratio was calculated as the ratio of the maximum amplitude of the signal over the root-mean square of the noisy part of the EGF. Since only the vertical components of the ground motion were used in this study, the EGFs are dominated by Rayleigh surface waves. The Love waves were harder to extract from the seismic noise analysis than the Rayleigh waves at Lastarria volcano, so we performed the following analysis using only the Rayleigh waves.

Figure 4.2 depicts some examples of EGFs with respect to station LGG01 for different azimuths corresponding to different stations.
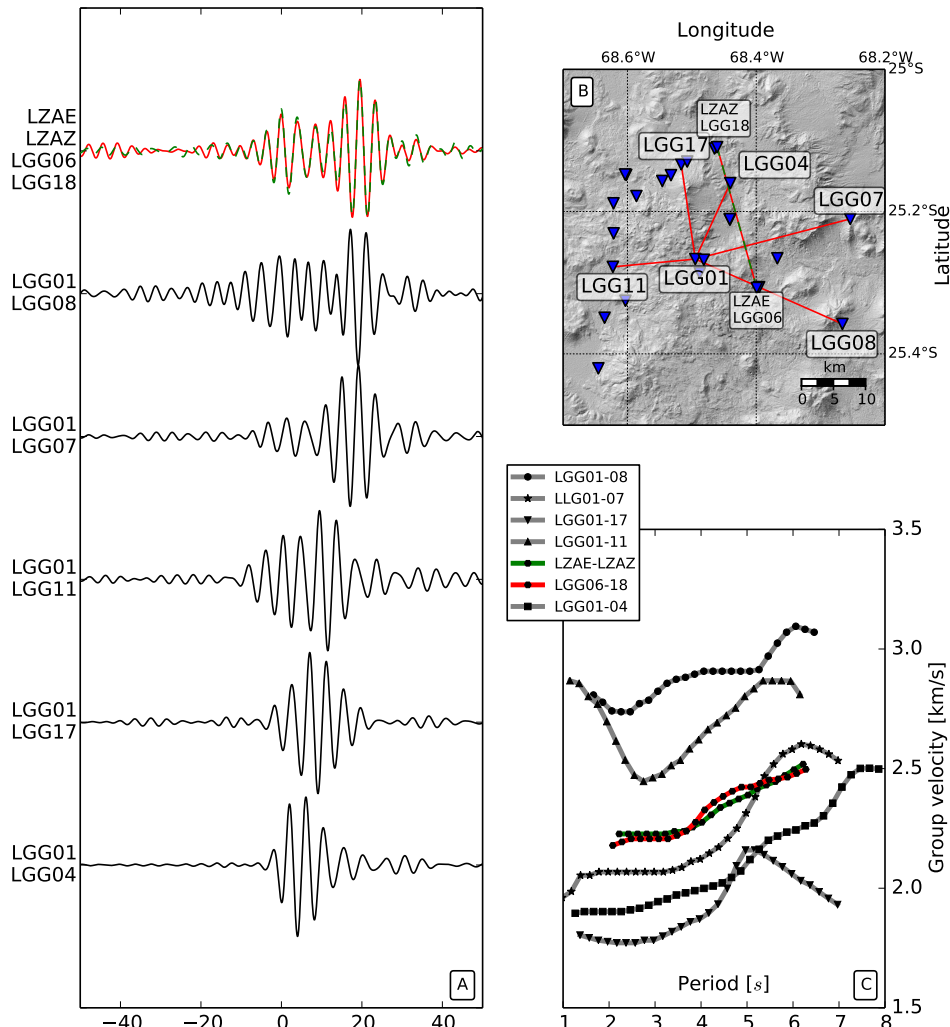
FIGURA 4.2: (a) Examples of EGFs filtered around 4 s for the paths presented in 2b. EGFs for station pairs LZAE-LZAZ and LGG06-LGG18 are superposed (red and green) since they cross the same path represented by the red-green line in 2b. (b) Map of the Lazufre volcanic zone and seismic station used in this study (reversed blue triangles). The red lines and the red-green line are the paths probed by measurements presented in 2a and 2c. (c) Dispersions curves associated to the EGFs presented in 2a. The maximum group velocity discrepancy observed between pairs LZAE-LZAZ and LGG06-LGG17 is equal to 0.05 km/s.

4.4.3. Group velocity measurements

The Rayleigh-wave fundamental mode dispersion curves were determined from each EGF via a frequency-time analysis (FTAN) [e.g., Dziewonski et al., 1969]. The FTAN technique consists of the application of a set of Gaussian filters with different central frequencies to the input signal spectrum. The group arrival times are estimated from the maxima of the time envelopes. It is known that the method leads to a systematic error in the group velocity estimates due to variations in the spectral amplitudes that cause a shift of the central frequency towards the origin of the filtered spectrum [Levshin et al., 1989]. This effect was corrected by computing the centroid frequency [Shapiro and Singh, 1999], which is the frequency where the filtered spectrum reaches its maximum. The resulting dispersion curves were manually selected, i.e., we kept these that vary smoothly in their period, and these for which the stations are separated by at least two wavelengths [Brenguier et al., 2007]. The maximum number of 128 ray paths was reached at a period of 4 s. Figure 4.2(c) gives examples of dispersion curves for the same ray paths presented in Figure 4.2(b), where the main energy is between 1 and 8 s. Figure 4.2(c) shows that the paths between pairs of stations at the vicinity of the Lastarria volcano have slower group velocities than those which do not cross the volcano area. This characteristic is well represented in Figure 4.3 where the variation of the group velocities around their mean for each path is shown. Figure 4.3(b) shows the propagation of the maximum of the envelope of the Rayleigh waves for each selected station pair as a function of inter-station distance for frequencies filtered around 3s. We find that the propagation of the Rayleigh wave packets have a different speed depending on the path. The paths passing close to the Northern area of the Lazufre volcanic zone and the Lastarria volcano have a Rayleigh wave train traveling with a velocity of about 1.5 km/s whereas the paths passing far from the volcano (mainly located at the Southern area of the Lazufre Volcanic Zone) have a higher velocity of about 2.1 km/s.

4.4.4. Selection of the dispersive curves

Three quality criteria have been applied in order to select the best dispersive curves: (1) selection of the best EGFs with a signal-to-noise ratio greater than 8; (2) separation of the stations by at least two wavelengths; and (3) clearness and continuity of the Rayleigh wave dispersion curves. Points (1) and (2) are done automatically whereas point (3) is
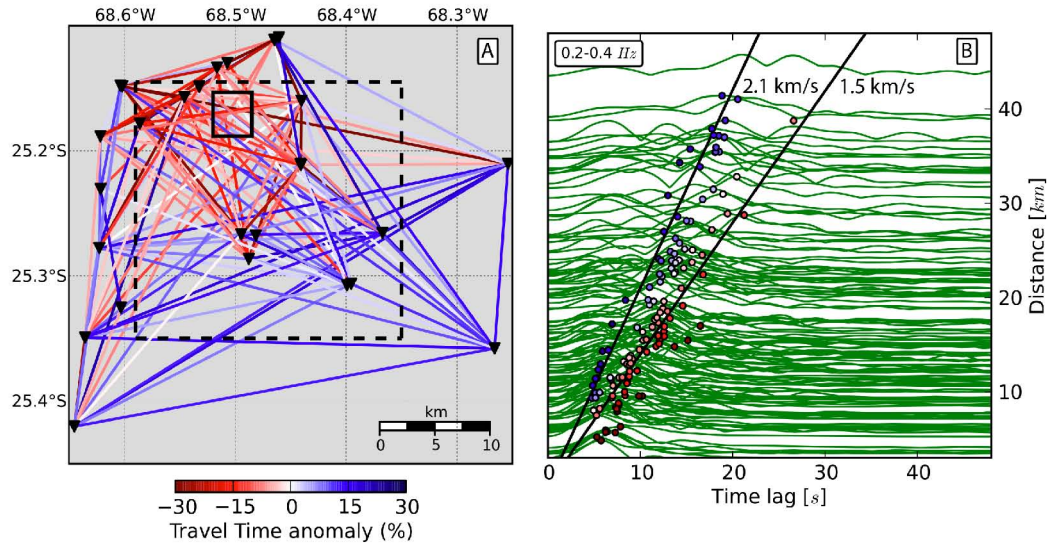
FIGURA 4.3: (a) Ray paths used in this study for the inversion along with the perturbations in travel times with respect to the average velocity observed at 3 s. (b) Envelopes of the ANT cross-correlations at 3 s for Rayleigh waves, plotted as a function of time and inter-station distance, the distance between each station pair. The peak of each envelope is shown as a colored circle whose colors refer to the velocity anomaly presented in (a). The plain line rectangle referred Lastarria's deformation. The dashed-line-square is the contour of the satisfactory-resolution-box.

done manually.

The maximum difference in the group velocity between similar inter-station paths (pairs LGG06-LGG18 and LZAE-LZAZ) is about 0.05 km/s, which can be considered as a good proxy for the estimation of the error done on the group velocity between the two networks.

4.4.5. Tomographic inversion

Rayleigh-wave group velocity tomographic maps were obtained from the picked travel times at different selected periods (1 to 8 s with a step of 0.2 s) by means of a non-linear iterative 2-D tomographic technique (Rawlinson et al., 2008). At each iteration, the ray paths between stations were updated so that the influence of their length was taken into account to compute theoretical arrival times. This step was carried out by the Fast Marching Method (FMM) (Sethian, 1996; Rawlinson and Sambridge, 2004). The FMM is a grid-based Eikonal solver that uses implicit wavefront construction and provides stable and robust solutions for wave propagation in highly heterogeneous media (e.g., Rawlinson and Sambridge, 2004; Rawlinson et al., 2008), as it is expected for volcanic environments. The inversion method then seeks for the perturbation of the model parameters that best
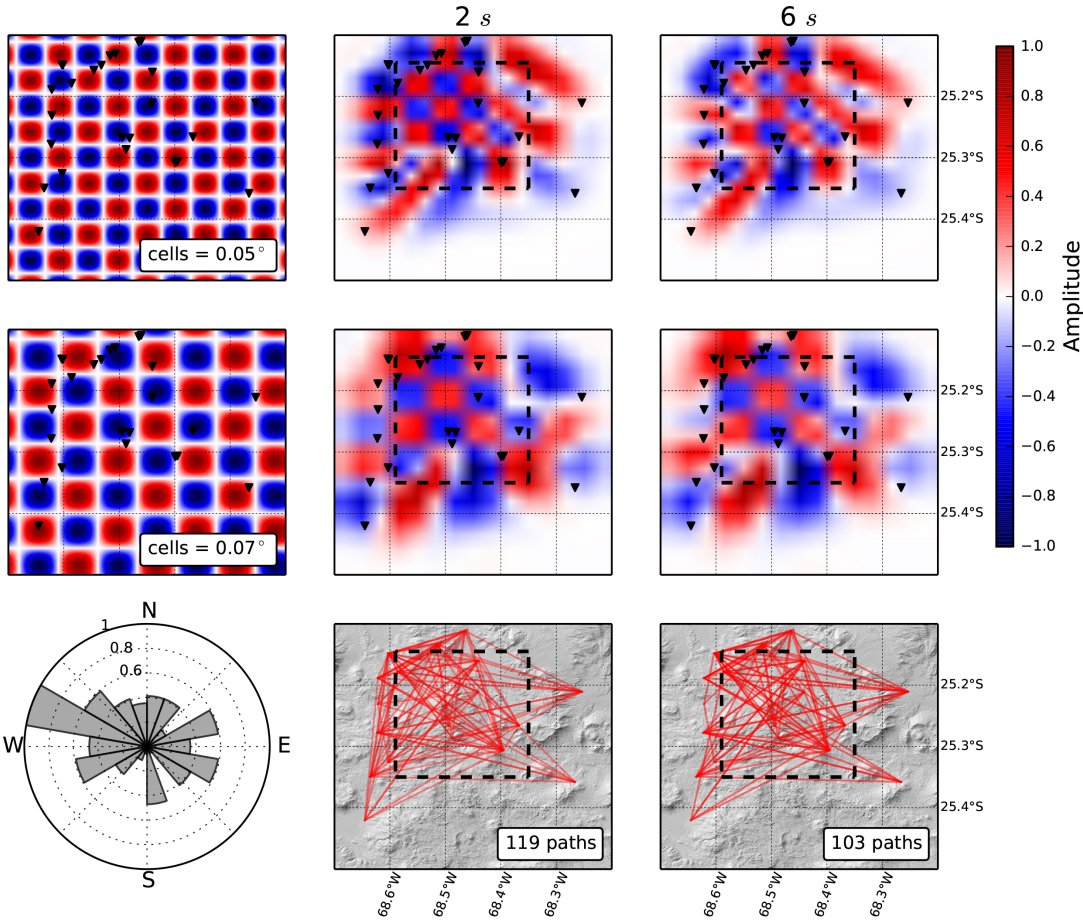
FIGURA 4.4: Resolution analysis of the tomographic inversion. The two first rows are the checkerboard tests showing the resolving capabilities of the inversion. On the left hand are two artificial input models, and the corresponding inversion results are shown for 2 and 6 s period. Resolution of the 2-D tomographic inversion is also assessed through the ray-path density presented on the third raw for 2 and 6 s period. The low left hand corner polar diagram depicts the normalized path density versus the azimuth at 4 s, where the maximum of 128 ray paths is reached. The dashed-line-squares are the contour of the satisfactory-resolution-box.

match the group velocity. Once the perturbations are estimated, the model is updated and the propagation paths are retraced using the FMM scheme. The Fast Marching Surface (wave) Tomography (FMST) code was used in this study [cf. Rawlinson et al., 2008]. The tomographic inversion was performed on a 0.016° by 0.016° (1.8 km by 1.8 km) grid at each period, which gave an optimum balance between resolution and recovery. As we perform here a 2-D tomography with respect to the period, we have no direct information on the depth. The depth resolution will be discussed in the next paragraph, while performing a 3-D inversion. The weight of the spatial smoothing and damping was estimated using standard L-curve analysis [e.g., Menke, 2012]. The inversions were carried out with a starting model of constant velocity equal to the mean group velocity observed

at each period. More specifically, the mean group velocity was chosen as the average of all the group velocities calculated using the FTAN method for every existing pair of stations for a given period. Synthetic checkerboard tests were performed in order to investigate the resolution of our results at different periods (Figure 4.4). Each checker model was assigned with alternating velocity perturbations of ±0.5 km/s. A "satisfactory-resolution-box" was then defined where the results can be interpreted with fair enough robustness (represented in Figures 4.1, 4.2, 4.4 and 4.5). The box excludes the areas of the model, where the smearing of the checkerboards is evident at all periods. Resolution of the 2-D tomographic inversions is also assessed through the ray-path density as presented in Figure 4.4.
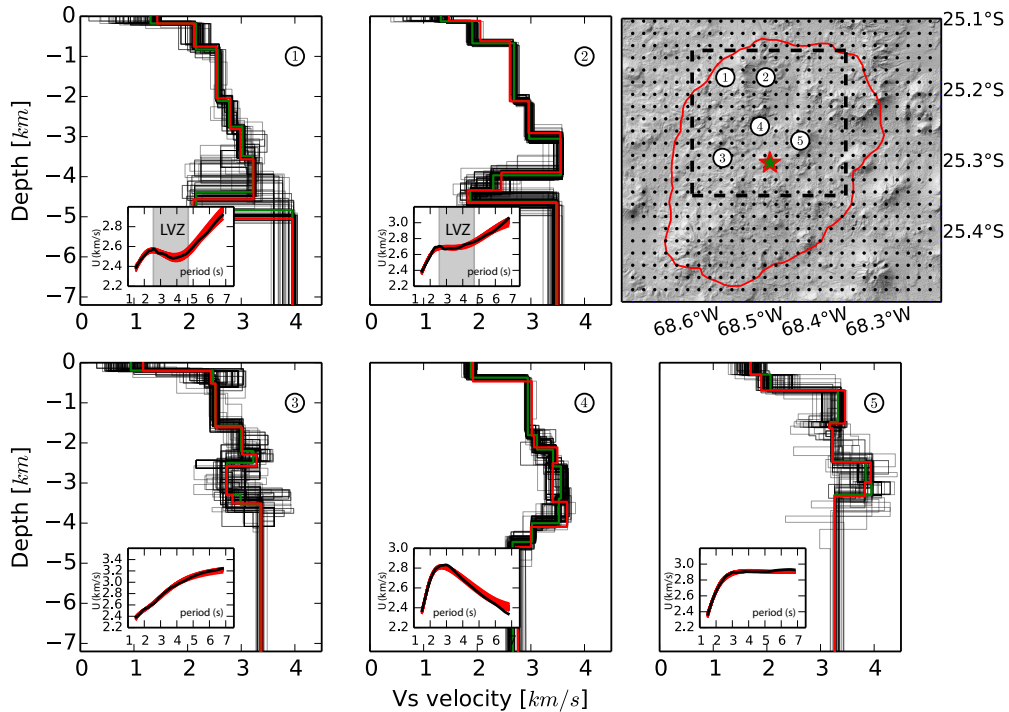
FIGURA 4.5: Selected examples for the V_S versus depth inversion and their location at Lazufre. 1-D velocity models are referred with a number that is reported on the map. Black lines are the 200 best models. Green lines are the averaged velocity model for the 200 best models obtained. The red lines are the last iteration's model (best misfit). Black dots on the map indicate inversion nodes used to obtain the 3-D shear wave velocity model described in the text and presented in Figures 4.6 and 4.7. The dashed-line-square is the contour of the satisfactory-resolution-box. The green star represents the center of the main InSAR anomaly and the red contour line represents the shape of the main InSAR anomaly.

4.4.6. Three-dimension shear-wave velocity model

First, we generated a one-dimensional velocity model. To accomplish this, "local" dispersion curves were constructed at each cell inside the satisfactory-resolution-box from the Rayleigh group velocity tomographic maps obtained at each of the previously mentioned periods. These curves were fit by polynomial functions and then inverted using a simulated annealing algorithm that minimizes the misfit value calculated as the semblance between the data (the local dispersion curve) and the synthetics [Iglesias et al., 2001]. The inversion was performed for thickness and S-wave velocity of eight layers overlying a half-space. The initial model at each cell was taken as the last output model of the previous inverted cell, providing a natural smoothing for the entire model. Finally, the 200 best models were averaged to produce a "local" 1-D S-wave velocity structure versus depth at each cell. All of the synthetic dispersion curves show a good fit to the observations (the local dispersion curve) with low mean value (0.11 km/s) of the misfit for all inversions. Examples of 1-D S-wave velocity models for selected cells are presented in Figure 4.5.

Second, a model showing a 3-D distribution of shear-wave velocities was generated from the inverted 1-D models for all the 195 cells (Figure 4.6, Figure 4.7). This model was constructed using a smooth bivariate spline approximation of three cell length in order to represent the structures smoothly. Figure 4.6 depicts six horizontal slices across the 3-D shear-wave velocity model at different depths (0.4, 1, 2, 4, 5 and 6 km). Figure 4.7 shows two vertical profiles crossing the Lastarria volcano (corresponding to $A - A'$ and $B - B'$ in figure 6(a)) across this model.
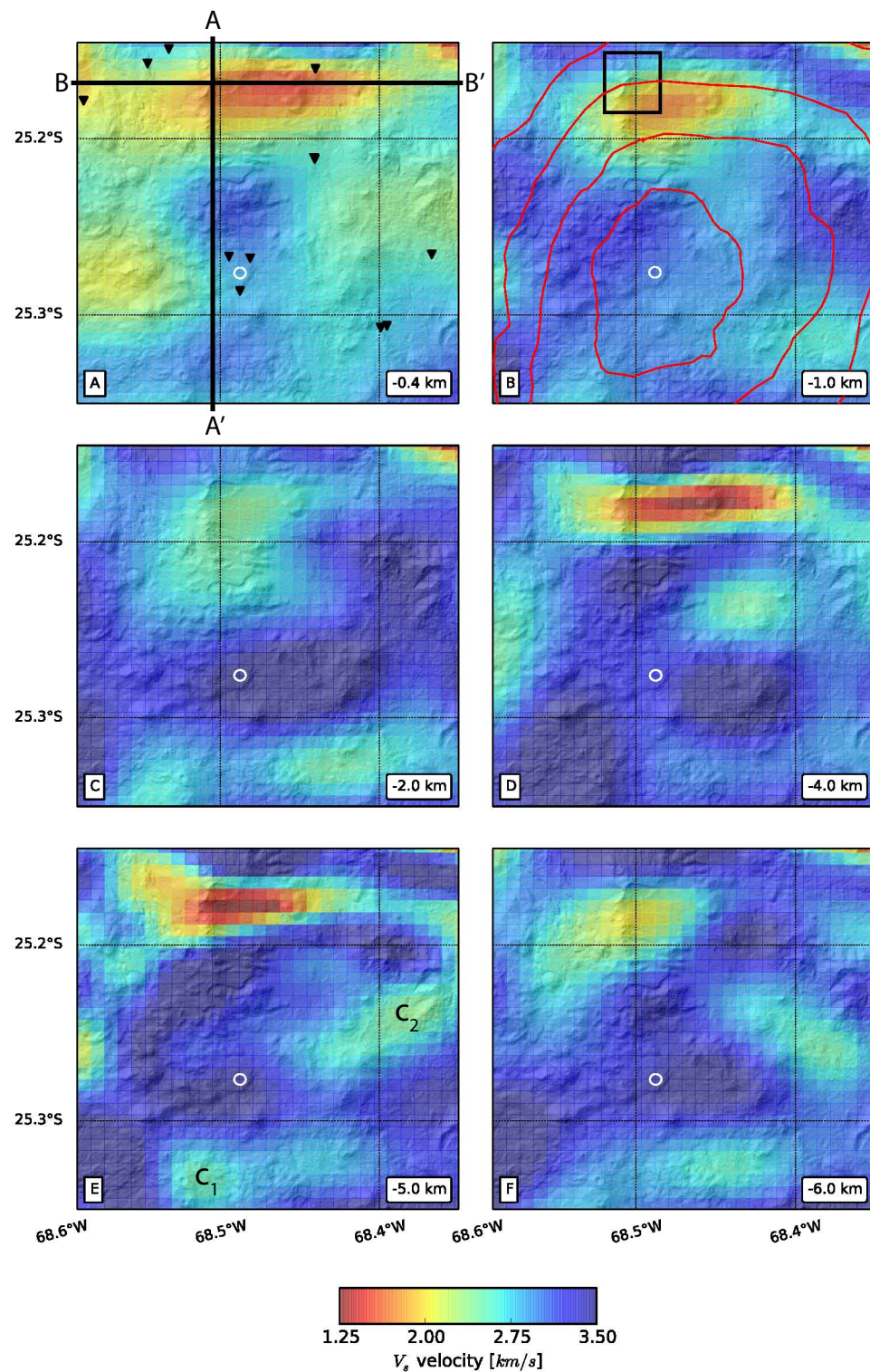
Figura 4.6: Horizontal slices through the 3-D Vs-velocity model inside the satisfactory-resolution-box. The black rectangle in (b) depicts the zone affected by the Lastarria uplift. The red lines in (b) represent the Lazufre uplift. The white dots present in all sections refer to the center of InSAR anomaly. Labels associated to velocity anomalies are referred in the text.
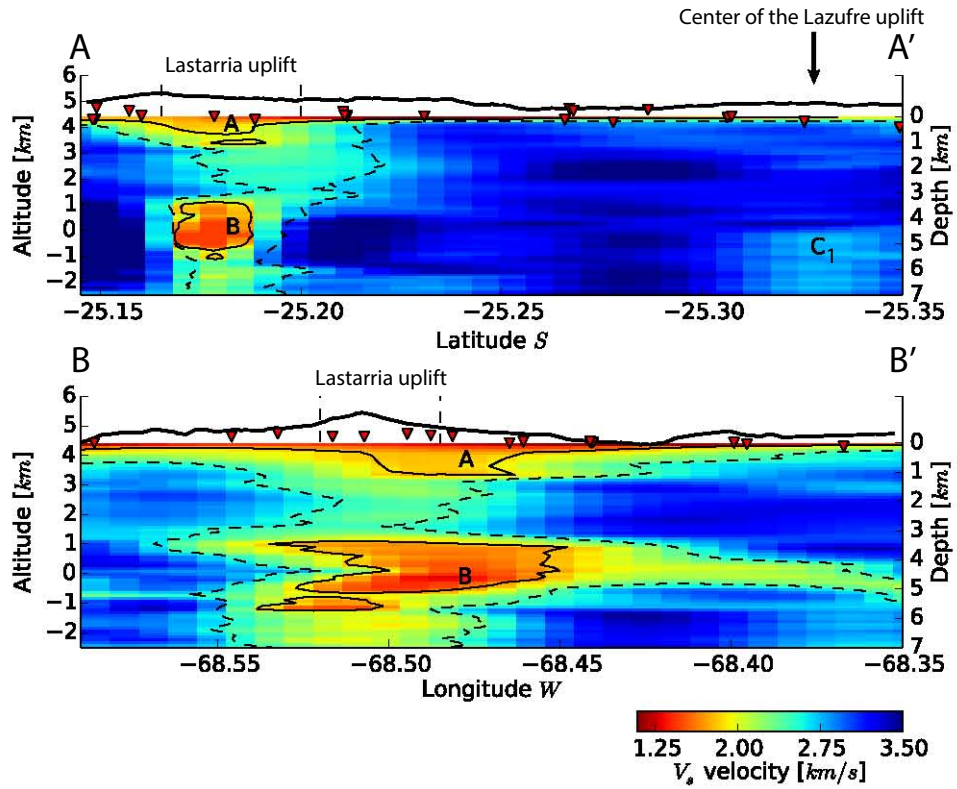
FIGURA 4.7: Vertical slices through the 3-D Vs-velocity model along the $A - A'$ and $B - B'$ profiles represented in Figure 4.6(a). Cross-section results are presented with no vertical exaggeration (1:1) along with the topography. The continuous black line represents the 1.8 km/s iso-velocity field and the dashed black line depicts the 2.53 km/s iso-velocity field. The topography is represented here but has not been taken into account in the inversion process. The reference altitude of 4300 m a.s.l. corresponds to the average between the highest at lowest seismometer altitudes. Labels associated to velocity anomalies are referred in the text.

4.5. Results and discussion

All models and inversions are performed in a half space, where the free surface is the mean elevation of 4.3 km above sea level. The depths values are given with respect to this reference level.

4.5.1. Identification of low velocity anomalies

Three S-wave velocity anomalies have been identified at Lazufre. The first one (A in Figure 4.7) has an S-wave velocity of about 1.6 km/s, corresponding to a velocity contrast of 54 % with respect to the surrounding S-wave velocity of about 3.5 km/s (Figure 4.7), which is a typical value of crustal rocks. This ultra low velocity zone (ULVZ) A is shallow, between 0 and 1 km depth, and has a funnel-like shape that is larger when close to the surface

and smaller at around 1 km depth. Its horizontal extension is slightly larger than the Lastarria volcano edifice, depending on the depths considered (Figures 4.6a and 4.6b). It has an extent of about 9 km in the EW direction, 4 km in the NS direction and 1 km in the vertical direction, at a depth of 0.4 km (Figures 4.6a and 4.6b). Considering its funnel-shape and the 1.8 km/s V_S iso-contour (this value corresponds to a 26 % melted magma as described after), the volume of this anomaly A is about 12 km^3. The ULVZ A is located just below a region of high fumarolic activity of Lastarria volcano [Aguilera et al., 2012, Naranjo, 1985]. The location of the ULVZ A, as well as its particular funnel-shape, strongly suggest the presence of a material rich in fluids, which would decrease the S-wave velocity. Hence, the funnel-like shape of the ULVZ A may be associated with a "classical" hydrothermal model [e.g., Ingebritsen and Sorey, 1985] where a central up-flow zone feeds various superficial hydrothermal features. The lateral outflows are probably regulated by some structural control of the permeability, but the important fracturing, heating and fluid migrations contribute to extend the hydrothermal system near the surface. The presence of fluids in the ULVZ A is also suggested by the hybrid character (combination of low and high frequencies) of many small shallow seismic events, some of them being monochromatic and others having several narrow frequency-peaks. Figure 4.8 illustrates an example of a hybrid event with two dominant frequencies and a long duration of more than 20 seconds, suggesting a persistent resonating phenomenon due to the presence of fluids.
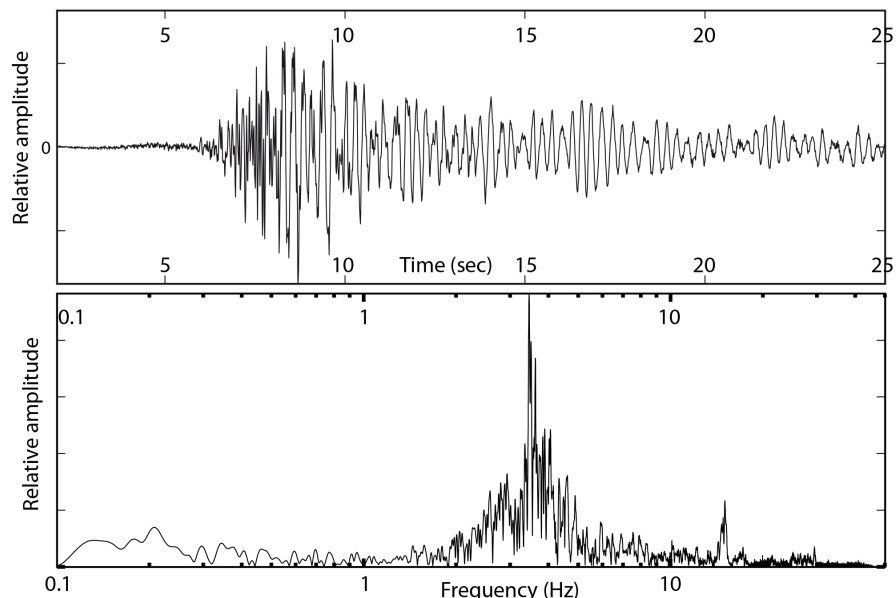
FIGURA 4.8: Example of a hybrid event (6 April 2006) observed at Lastarria volcano and filtered between 1 and 49 Hz recorded on the vertical component of a broadband seismometer (Guralp 40T). Many of such events are recorded at Lastarria (i.e. more than 100 in a week in April 2006).

The second anomaly (B in Figure 4.7) is also considered as an ULVZ, since it has an S-wave velocity of about 1.3 km/s, corresponding to a velocity contrast of 63 % with respect to the surrounding rock velocity. It is the smallest velocity found in the studied region. Anomaly B is located between a 3 and 6 km depth and has an oblate spheroidal-shape, elongated in an EW direction, in the same direction as the hydrothermal reservoir A. Although a detailed characterization of a body cannot be assessed only on its S-wave velocity, we assume that the ULVZ B, which coincides with the active Lastarria volcano, infers high temperatures and/or the presence of partial melting in the shallow crust [e.g., Christensen and Mooney, 1995, Lees, 2007, Masterlark et al., 2010]. These high temperatures found on Lastarria (up to 400°C; [Aguilera et al., 2012]) may be due to the presence of close magma, at a few kilometers of the surface. We speculate that the ULVZ B is a magma chamber combined with the presence of fluids generated by the partial degassing of this magma from 6 km depth until the surface. As the deepest part of the hydrothermal reservoir A, at 1 km depth, has the same shape as the magma reservoir B (Figure 4.7) and elongated in the same direction (E-W), we hypothesize that the latter feeds entirely or partly the former located just above. Hence, the magma reservoir B may explain part of the degassing observed in the Lastarria volcano and the presence of the hydrothermal system A located just at the top of it (Figure 4.7). Magma chamber B is probably smaller than the one imaged in Figure 4.7 because of the smoothing used in the S-wave maps. Considering a 1.8 km/s V_S iso-contour, the maximum size of anomaly B is 9 km in the E-W direction, 3 km in the N-S direction and 3 km for its vertical extension, consistent with a magma reservoir of 81 km^3. The choice of a contour 1.8 km/s is somehow artificial. In order to estimate the error done on the shapes of the reservoirs, we show two contours in Figure 4.7: one corresponding to 1.8 km/s and another one to 2.53 km/s. The choice of 2.53 km/s corresponds the smallest velocity for which we found a unique reservoir of S-wave velocities varying from about 1.25 km/s to 2.53 km/s (Figure 4.7). Following a theoretical relationship for a fluid-saturated granite at 800°C and a pressure of 0.1 GPa (corresponding to a depth of 5 km) as a function of porosity filled with different rhyolite melt and water-CO2 contents, the percentage of melted material is estimated to range between 31 % and 26 % [Chu et al., 2010]. Even though the V_P/V_S ratio is unknown, it can be estimated from the same theoretical relationship. In our case, it is equal to about 2.25. Although these values appear very high, they are similar to the one obtained for the magma reservoir underlying the Yellowstone caldera [Chu et al., 2010]. Note that the anomalies A and B are not clearly separated. We have a gradient of S-wave velocity from

A to B and not a strong contrast of velocity. The S-wave velocity between A and B is about 1.5-2.0 km/s, much smaller than the 3.5 km/s of the surrounding rock. If we chose a V_S iso-contour of 2.53 km/s instead of 1.8 km/s, we have a single anomaly and not a clear separation between the two anomalies A and B (Figure 4.7). Nevertheless, the difference of the two velocities (1.8 and 2.53 km/s) is strong enough to interpret it as due to two different materials, without saying that they are not related. Indeed we think that the anomaly A is related to the anomaly B, in the sense that the degassing in B migrates until the subsurface where fluids concentrate. Both anomalies are related to Lastarria volcano rather than Lazufre, with important implications as further discussed below.

The third low velocity anomaly (C_1, C_2 in Figure 4.6; C_1 in Figure 4.7) is not as strong as the previous ones. It consists of a patchwork of weak velocity zones with S-wave velocity of about 2.7 km/s, corresponding to a relative velocity contrast of 23 % with respect to the surrounding material. This is well observed between a depth of 5 to 7 km, located at the Southeastern part of the Lazufre volcanic zone (denoted by C_1 in Figure 4.7a), beneath the center of the main uplift deformation. As our model does not image features deeper than 7.0 km, the presence of a larger intra-crustal magma reservoir extending to greater depths [Anderssohn et al., 2009, Froger et al., 2007, Pritchard and Simons, 2002, 2004, Ruch et al., 2008, 2009] cannot be dismissed. Nevertheless, we can affirm that a large magma chamber located at depths less than 7 km is not imaged by our tomography under the main deformation anomaly. This information reduces the uncertainties on the depths of such a magma chamber proposed by Remy et al. [2014] and allows us to better estimate the volume of this source (thickness of the flat-topped magma chamber or of the sill). As a consequence, we suggest that this patchwork of low velocity zones may correspond to the upper limit of the deeper large magma reservoir mentioned before. The weak shear-wave velocity observed could result from a strong heating, an important fractured zone and/or a significant concentration of volatile at these depths. A strong degassing may also occur, resulting in a decrease of S-wave velocity.

4.5.2. Tectonic interpretation

The E-W direction of both reservoirs below Lastarria volcano is near the edge of the Lazufre inflation area. An EW trend is not compatible with the regional stress tensor

found by the study of regional fractures, dikes and the interpretation of the InSAR data [Ruch and Walter, 2010]. This E-W direction may rather be related a) to a local stress tensor which may be the superposition of the regional stress tensor modified by the local stress tensor generated by the main deformation anomaly, as observed at other volcanoes [e.g., Legrand et al., 2002] or b) to reactivated pre-existing structures. A large magma chamber deeper than 7 km depth below the main deformation at Lazufre explains the InSAR data and would generate radial fractures close to the top of this anomaly and circular fracture zones at the margin of this deformation zone, which is typical of a caldera formation. Inflation of a deep reservoir could generate a stress field favoring the generation of the anomaly detected in this study. The position of our anomalies A and B agrees with the location of a girdle of volcanoes encircling Lazufre area [Froger et al., 2007]. As far as the Lastarria volcano is located at the border of the main deformation anomaly, as well as other volcanic edifices [Froger et al., 2007], we conjecture that the E-W direction corresponds to an active part of this ring fracture zone around the main anomaly (Figure 4.9). Fracture studies will address the hypothesis compatible with a stress transfer model, which may explain geometry and positioning of the anomalies.

4.5.3. Integration with other studies

Our results are consistent with previous (1) geochemical, (2) geodetic, (3) seismological and (4) magneto-telluric studies at Lastarria but significantly add resolution and interpretation to the reservoir problem.

(1) A coupling of the shallow hydrothermal source to a deeper magmatic source was also deduced by the past geochemical analysis [Aguilera et al., 2012]. Effectively, the Lastarria volcano has four intense and continuous fumarolic fields [Naranjo, 1985] with outlet temperature from 80°C to over 408°C between 2006 and 2009 [Aguilera et al., 2012], located just above our hydrothermal reservoir A. It corresponds also to the magma reservoir B, where high degassing may exist (Figure 4.7) and may explain such high temperatures of about 400°C that a hydrothermal system alone could not explained. These superficial fumarolic fields seem to exist at least since the discovery of Lastarria volcano at the end of the 19th century [Aguilera et al., 2012]. The fluids emanating close to the volcanic conduit have chemical and isotopic compositions traducing both a magmatic and a hydrothermal source [Aguilera et al., 2012].
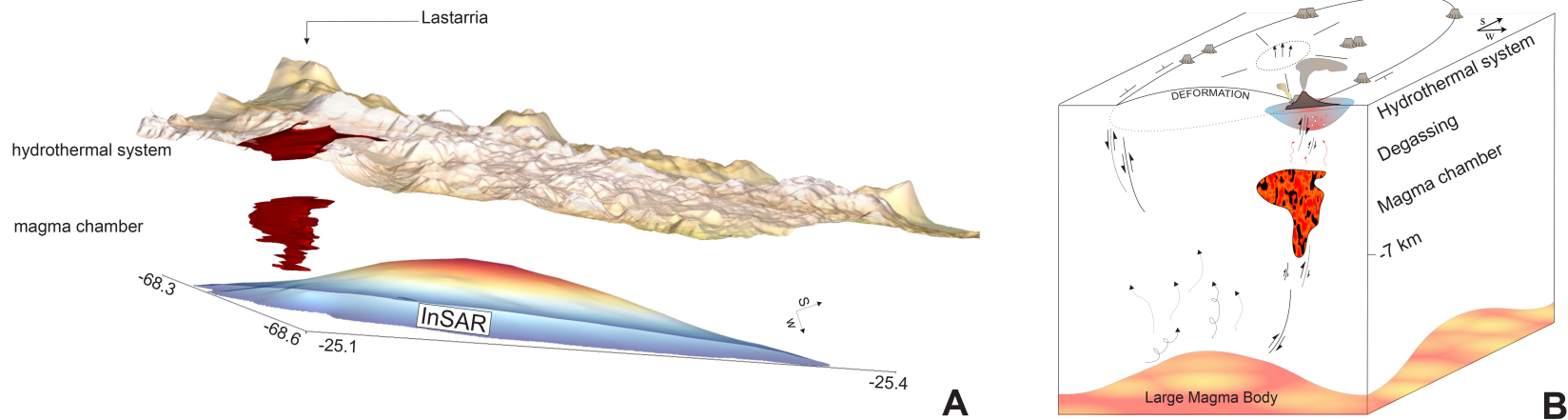
Figura 4.9: *S*-wave velocity anomalies under Lastarria volcano, topography and InSAR deformation (from Froger et al. [2007]). (a): 3-D view of the magma chamber and hydrothermal system beneath the topography. Magma chamber and hydrothermal systems are delimited by the 1.8 km/s V_S iso-contour. The blue-red relief represents the InSAR uplift measurements as in Figure 4.1. The magma chamber took place at the border of the uplift. Uplift might have produced a circular network of faults facilitating the magma intrusion from a deeper source as explained in B. (b): Cartoon representation of the volcanic system. Lastarria volcano is near the edge of the InSAR uplift [Froger et al., 2007]. The uplfitting episodes may have caused a fracture girdle (as at Uturuncu; Walter and Motagh [2014]) which could represent a preferential path-way for magma, resutling in the formation of the magma chamber imaged in this study (LVZ B). Deeper magma body may have feed the actual magma chamber. Deep magma may aslo cause an important degassing or an alteration of the upper crust (symbolized by the squiggly black arrows), which is may be reflected in our tomography by the LVZ C. The magma chamber's gases feed and warm up the hydrothermal system (symbolized by the red arrows).

One shows a main magmatic-source degassing process while the other indicates that the fluids are emanated from a superheated vapor at hydrothermal conditions that is later cooled and condensed at shallow depth, inhibiting the formation of a continuous aquifer at shallow depth [Aguilera et al., 2012]. Our results suggest that a possible magma reservoir is much closer to the surface (located 3-6 km below the surface) than previously assumed by Aguilera et al. [2012]. These significant fluid reservoirs may explain why Lastarria volcano is currently the most important gas source in the Chilean central volcanic zone (17°S to 26°S), with a total volatiles output (13,500 t/d; Tamburello et al. [2014]). The concentrations of HCl and SO_2 of the Lastarria gases found by these authors are too high to be originated at a depth higher of 10 km and should come from a shallower magmatic reservoir. Therefore, we interpret the anomaly B as a magmatic reservoir rather than a hydrothermal reservoir only. The presence of such quantities of gases come more likely from shallower depths, such as 3-6 km (our magma reservoir B), inferring a high-temperature open-vent system. The isotopic composition of the fluids also shows a low local precipitation origin, especially in this extremely dry region [Aguilera et al., 2012], confirming its magmatic origin instead of a meteoritic contribution. Hence, we propose that the gasses emitted at the Lastarria volcano and concentrated in the hydrothermal system A (Figure 4.7) may originate from the degassing of the magma chamber B (Figure 4.7) and not from the more distant (about 13 km) and deeper (7-15 km depth) magma reservoir below the LVZ C. Nevertheless a stress interaction between these different sources is likely, as proposed earlier [Ruch et al., 2009].

(2) The Lazufre's uplift was detected by InSAR measurements and has started sometime between 1997 and 2000 [Henderson and Pritchard, 2013, Pritchard and Simons, 2002, 2004]. Today, it has an extent of about 2,000 km^2 [Henderson and Pritchard, 2013, Pearse and Lundgren, 2013, Remy et al., 2014, Ruch and Walter, 2010]. The maximum ground deformation velocity is about 3.0 cm/yr for the March 2003-May 2010 period [Anderssohn et al., 2009, Remy et al., 2014, Ruch et al., 2008]. More recently, Remy et al. [2014] gave an estimation of the maximum uplift rate of 3.85 ±0.5 cm/yr in the LOS (line of sight) direction, combining information with GPS data. The precise nature of the process responsible for the observed uplift is still under debate. Several models of deformation sources, based on InSAR and GPS data inversion, have been proposed for the Lazufre. One of the difficulties in modeling the depth and size of these sources is related to the fact that InSAR data only consider one - and not three - directions of the displacement

field. The source-depth is particularly difficult to solve because of the classical trade-off between the velocity model, the geometry (sill, ellipse, oblate, prolate), the amplitude of the volume change and the depth itself [Froger et al., 2007, Pritchard and Simons, 2004, Remy et al., 2014, Walter and Motagh, 2014]. All aforementioned geodetic studies proposed the presence of an existing magma chamber inflating at depths ranging between 7 to 17 km to explain this large wavelength ground inflation, and they explored a large range of possible source geometries (e.g., spherical, prolate ellipsoid and penny-shaped crack). The source explaining the main deformation zone is at a depth between 10-12 km for Pritchard and Simons [2002], between 9-17 km for Pritchard and Simons [2004], between 7-15 km for Froger et al. [2007], between 8.5-13 km for Ruch et al. [2008], between 12-14 km for Ruch et al. [2009] and at 10 km for Ruch and Walter [2010] and Anderssohn et al. [2009]. All these depths have a reference level of 4 km a.s.l, which is the average altitude of the region. Ruch et al. [2008] and Anderssohn et al. [2009] proposed that the uplift observed during the 2003-2008 period was caused by a fast lateral expansion, up to 8 km/yr of a thin magmatic sill or a more extended reservoir. Nevertheless, Pearse and Lundgren [2013] and Remy et al. [2014], using different approaches, showed that the surface displacement measured at Lazufre could be explained without any need for significant lateral source expansion. Both studies lead to the conclusion that the surface displacements observed at Lazufre are related to a pressure increase in a sill or a large magma chamber located at depth between 2 and 14 km below ground surface. Nevertheless, while these two latter studies have greatly decreased the class of viable magma chamber shapes, the non-uniqueness of the solution using deformation data alone prevents the reduction of large uncertainties on both the shape of the source and its depth. For example, Remy et al. [2014] confirmed the observation by Ruch et al. [2008] that a large flat-topped magma chambers produced almost identical surface displacements to a thin sill. The position of the LVZ C on map views coincides with the center of the main InSAR uplift area (of about 3.0 cm/yr) and also with the deeper magma chamber found by these previous studies. As no ULVZ is detected below the main deformation anomaly between the surface and 7 km depth, this information may help in the modeling of InSAR and GPS data. Our seismic tomography only images the roof of the deep reservoir.

A second and smaller inflation region centered at the Lastarria volcano that started in 2003, has been identified by InSAR data [Froger et al., 2007]. The Lastarria is the unique active volcano of the area and is located at the Northwest margin of the Lazufre zone

(plain line rectangle in Figure 4.1). The deformation has an uplift rate of about 0.9 cm/yr in average, with a maximum rate of 2.5 cm/yr between March 2003 and June 2005, and affects a 6 km wide area [Froger et al., 2007]. The depth of a single point source of this deformation has been estimated at about 1 km [Froger et al., 2007] and at 0.6-0.9 km [Ruch and Walter, 2010] below the summit of Lastarria volcano, inside the volcanic edifice, suggesting a hydrothermal origin. The region of the small InSAR uplift of about 1 cm/yr at Lastarria volcano and of about 6 km width (Froger et al. [2007], Remy et al. [2014]; Figure 4.1) lies inside the LVZ A. The LVZ A is even larger than the deformation field, which is expected since the fluids located at the edges of the hydrothermal system may have a small influence on this InSAR deformation. In contrast, the fluids concentrated at the middle of the hydrothermal system A may contribute with a greater force to this uplift. The pressure increase inside the magma chamber B may also partly explain the Lastarria volcano deformation because it is also located just below the Lastarria volcano uplift. Froger et al. [2007] suggested a source depth at 1 km below the summit of the volcano to explain the Lastarria volcano deformation field. This depth roughly corresponds to the spatial average of the two sources we imaged (A and B), even though we have not shown it. Various modeling of the Lastarria deformation have to be performed to address the respective influences of these S-wave anomalies on Lastarria deformation.

(3) The deeper structure of the Lazufre system has been studied using P-wave travel time delay tomography by Heimann et al. [2013]. They find up to 40% P-wave velocity reductions between about 5 and 20 km depth under the Lazufre large-scale inflation area, a result that is compatible with our study. Stacked PS receiver functions from teleseismic and regional earthquakes confirm a strong S-wave velocity contrast in the center of the uplift at a depth of about 9 km (5 km below sea level [Heimann et al., 2013].

(4) Magneto-telluric tomographies performed in a small region around the Lastarria and with a good resolution to a depth of 10 km [Díaz and Zamudio, view], depict very similar features to our results. These authors observed a shallow resistivity anomaly (below 1 Ωm) between 0 and 1.5 km, as well as the existence of an anomaly (below 10 Ωm) to a depth of about 3-6 km oriented in an EW direction, which is in agreement with our ANT results. Both, the seismological and MT tomography, showed that the anomaly (i.e., magma reservoir) is not precisely below the summit but at a few km southward. MT tomography has been performed at a larger region by Budach et al. [2013] below the main

deformation zone, where they found a very large anomaly at depths between 20 and 70 km with offset and dips to the East.

4.5.4.　Comparison with the Uturuncu uplift

Studies have been realized at the Uturuncu uplift, in Bolivia, with a deformation anomaly similar to the Lastarria's one [e.g., Jay et al., 2012, Pritchard and Simons, 2002]. ANT performed by Jay et al. [2012] revealed a low-velocity zone at depths between 1.9 and 3.9 km below the center of the crater. These authors suggested that since the LVZ persists at 3.9 km depth, it could represent either the final pathway of ascending magma from greater depths or a zone of hydrothermal alteration. In another study, a large zone of low S-wave velocity of 2.5-2.9 km/s has been identified in the Altiplano-Puna volcanic complex below Uturuncu at depths between 10 and 20 km [Ward et al., 2014]. The 3-D tomography performed by these authors revealed a low-velocity zone with a diameter of 200 km and a thickness of 11 km, interpreted as a magmatic underpinnings associated to the 11–1 Ma ignimbrite flare-up. A deep (below 15 km) low S-wave velocity anomaly has been imaged at Lazufre by Ward et al. [2013]. This anomaly is interpreted as belonging to the Southern Puna Magma Body [e.g., Bianchi et al., 2013]. Such large body should be seen below the Lazufre volcanic complex, but it has not been imaged in our results because they are limited to the first 7 km. At Uturuncu volcano, a fracture girdle encircling the deformation region was found [Walter and Motagh, 2014] similarly to the volcanic edifices concentrated at the periphery of the Lazufre deformation zone.

4.6.　Conclusion

We show that the Lastarria volcano hosts a shallow (3 to 6 km depth) magma reservoir. This is therefore a new example of andesitic volcano with shallow magmatic chamber in a compressional context [Chaussard and Amelung, 2012]. We show that the source of the major uplifts observed at Lastarria volcano and Lazufre area is more complex than the one proposed in past studies [Aguilera et al., 2012, Froger et al., 2007, Ruch et al., 2009]. Three low S-wave velocity anomalies have been found at Lazufre. One (region A) is very shallow, between 0 and 1 km depth below the active Lastarria volcano, covering a zone of about 36 km^2 at 0.4 km depth, and is naturally interpreted as a hydrothermal system already

identified by previous geochemical and geophysical results. It is slightly larger than the intense and permanent fumarolic zone of the active Lastarria volcano. A second anomaly (region B) has a sill-shape oriented in an E-W direction, between 3 and 6 km depth. Both the depth and the shape of this second anomaly suggest a magmatic reservoir, even if we cannot exclude the presence of some magmatic fluids that are degassing at these depths. A third one, smaller in amplitude, is located under the center of the main deformation anomaly, at depths greater than 5 km. This smaller anomaly may be the upper manifestation of a deeper magmatic chamber that we cannot image with the frequency range of our study. Our results are in very good agreement with past magneto-telluric and earthquake tomographies, geodetic deformations, gas composition and observed temperatures at Lastarria volcano. Our work shows the shallow structure of Lazufre region using seismic records (without earthquakes) to a depth of 7 km. We still require detailed imaging of the deeper structure in this area to infer the depth and the size of a large and deep magma body that generates the Lazufre uplift. The results will help in future works to constrain the sources responsible of InSAR deformation and furnish a velocity model in order to locate earthquakes in the Lazufre area.

4.7. Acknowledgments

Velocity models and site effects at Kawah Ijen volcano and Ijen caldera (Indonesia) determined from ambient noise cross-correlations and directional energy density spectral ratios.

5.1. Resumen

El volcán Kawah Ijen se ubica en la caldera del Ijen, en la parte oriental de la isla de Java, Indonesia. El volcán tiene la particularidad de alojar el lago cratérico de aguas ácidas más grande del mundo, lo que atestigua su constante actividad. Durante los últimos años, el volcán Kawah Ijen volvió a ser uno de los volcanes más monitoreados de Indonesia. La red sísmica permanente está compuesta de 9 estaciones instaladas por el Observatorio Real de Bélgica, el *US Geological Survey* y el *Center for Volcanology and Geological Hazard Mitigation.* Sin embargo, no existe ningún modelo de velocidad de esta volcán, lo que hace difícil analizar, interpretar y/o localizar la gran variedad de señales sísmicas que se generan dentro del edifico volcánico. Además, la configuración geométrica de la red sísmica no es apropiada para realizar una tomografía como las otras realizadas en esta investigación. Por ello en este capítulo se presentan alternativas para poder obtener modelos de velocidad usando correlaciones del RSA.

Los modelos de velocidad promedio de la caldera del Ijen se obtuvieron para los 3 primeros kilómetros de profundidad, gracias a la inversión de la curvas de dispersión apiladas; las cuales se generaron por correlación cruzada del RSA. Los perfiles de velocidad locales y más superficiales se obtuvieron mediante la inversión del cociente espectral H/V, calculado a través de la auto-correlación del ruido ambiental; es decir, por la relación de densidad de energía direccional del RSA (DEDHVR). Estos modelos de velocidad se compararon con la geología del área de estudio y permitieron evidenciar discontinuidades geológicas importantes.

En este trabajo, se aplica por primer vez la técnica de inversión del DEDHVR en un entorno volcánico y se muestra que esta técnica tiene un gran potencial para calcular con precisión y rapidez modelos de velocidad en volcanes. Por otra parte, se elaboró un mapa de los efectos de sitio alrededor del cráter del volcán Kawah Ijen, gracias a las mediciones de los DEDHVR registradas en 87 sitios. La horizontalidad de las capas geológicas superficiales, el gran afloramiento del borde del cráter y el modelo de velocidad inferido para el volcán, facilitan la interpretación de los resultados. Usando una aproximación de primer orden, fue posible deducir el espesor de las capas geológicas más superficiales y correlacionarlas con la geología del cráter del Kawah Ijen. Uno de los resultados más relevante de este estudio es que a diferencia de otros estratovolcanes, el volcán Kawah Ijen presenta una estructura superficial notablemente homogénea.

5.2.   Abstract

Two different ambient seismic noise techniques allow the determination of velocity models at Ijen caldera and Kawah Ijen volcano. At Ijen caldera, two average velocity models are constrained down to a depth of 3 km by inverting the stacked dispersion curve obtained by ambient noise cross-correlation. In addition, four local velocity models were obtained by inverting the horizontal to vertical spectral ratio of the directional energy densities of ambient noise (DEDHVR) i.e., computed through auto-correlation of ambient noise. This set of velocity models is then compared to the geology of the caldera and the local discontinuities are evidenced. At Kawah Ijen volcano, a map of local dominant frequencies is provided by the DEDHVR measurements recorded at 87 sites around Kawah Ijen volcano. The horizontality of the shallow layers and the great outcrop of the crater rim facilitate the interpretation of the DEDHVRs. Furthermore, the inversion of several juxtaposed DEDHVRs provided a complete 2-D velocity model of the flank of the crater. Unlike others stratovolcanoes, the Kawah Ijen appears to have a remarkably homogeneous structure. The DEDHVR technique is used for the first time in a volcanic environment and shows a great potential for an accurate and fast computation of the velocity model on volcanoes.

5.3.   Introduction

Kawah Ijen (8.058°S 114.242°E, 2799 m) is an active basaltic-andesitic composite volcano located inside the Ijen caldera on the eastern region of Java Island, Indonesia (Fig. 5.1). The volcano hosts the worldwide largest acidic crater-lake (0.03 km^3, pH around 0.0) and presents an important and continuous degassing [Delmelle and Bernard, 1994, Delmelle et al., 2000, Takano et al., 2004]. Eruptions at Kawah Ijen are considered very hazardous since they could lead to lake drainage that may result in catastrophic acidic lahars. In addition to a daily crowd of tourists, about 200 miners are working daily inside the crater to extract the sulfur of one of the largest native sulfur pit in the world and around 10.000 people live inside the Ijen caldera.

Recently, Kawah Ijen presented several episodes of unrest that spurred local authority to prepare evacuation [Caudron et al., 2015a,b]. During such unrest periods, seismic analysis improved the general understanding of this volcano. Since 2011, 9 permanent seismometers

(Fig. 5.1, Table 5.3) have been installed around Kawah Ijen, making it one of the most well monitored volcanoes in Indonesia. These instruments have shown that the Kawah Ijen volcano has an important seismic activity with a great variety of signals such as monochromatic tremors, volcano-tectonic, high-frequency and long-period events [Caudron et al., 2015a]. Monochromatic tremors have a fundamental frequency lying in the range of 0.9–2 Hz . When the tremors are particularly energetic, they are no more monochromatic and few overtones are observed. Volcano-tectonic, high- and low-frequency events have a frequency band ranging from 1 to 12 Hz [Caudron et al., 2015b].

The knowledge of the structure of the surface wave velocity is important to understand part of the complexity of the volcanic events. Numerical simulations demonstrated that the waveforms of volcanic signals strongly depend on the velocity model used [Cesca et al., 2008, Jousset et al., 2004, 2003, O'Brien and Bean, 2009]. The near-surface structure, linked to the local site effects, strongly perturbs the seismic wavefield [Mora et al., 2001, 2006], especially when unconsolidated layers of ash or pumice are present since they generate strong wave scattering [e.g., Parsiegla and Wegler, 2008, Wegler, 2003, Wegler and Lühr, 2001]. Determining an accurate velocity model for the first kilometers of the crust allows a better location of the volcanic events [Bean et al., 2008] and therefore, a mitigation of the volcanic hazard. It also helps to understand the formation of a volcano [Perrier, 2011, Perrier et al., 2012] and in certain cases, allows the detection of major faults or discontinuities [Ventura et al., 1999, Wang et al., 2003, Zhang and Thurber, 2003]. Traditionally, velocity structures on volcanoes are determined through seismic tomography using P- and S-wave arrival times obtained from teleseismic, regional or local earthquakes [e.g., Jousset et al., 2011, Lees, 2007]. By using this technique, the horizontal resolution of the structures is limited to one or a few kilometers [e.g., Kuznetsov and Koulakov, 2014, Prôno et al., 2009] and could not detect features deeper than a few tenths of kilometers [e.g., De Luca et al., 1997]. Active seismic experiments are also a common way to deduce the P-wave velocity model and allow recovering the structures in a shallower range of depths [e.g., Aoki et al., 2009, Zollo et al., 1998]. However active experiments are expensive and sometimes impossible to achieve on active volcanoes. Others techniques, such as the inversion of the dispersion curves extracted from regional and teleseismic earthquakes [e.g., De Barros et al., 2008], or a combination of these two last techniques [Battaglia et al., 2008], are also employed to image the shallow crust. Nonetheless, the shallower parts (<5 km) of the crust often lack a good resolution due to inadequate ray coverage and consequently, traditional techniques fail to detect small objects or thin layers [e.g.,
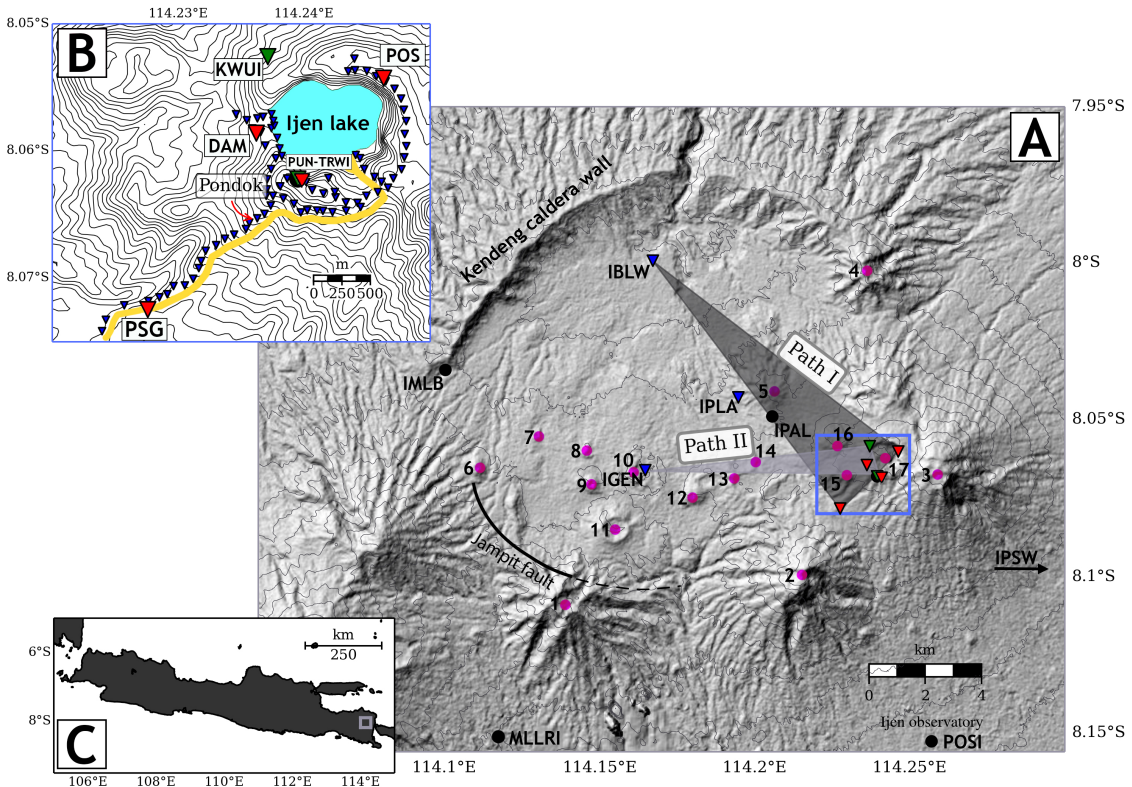
FIGURA 5.1: A) Map of the Ijen caldera. Inverted triangles symbolize the seismic stations used in this study. Red: ROB permanent network; Blue: ROB temporary network; Green: USGS permanent network; Black dots symbolize other seismic stations installed but not used for velocity models calculation owing to quality control imposed by ambient seismic noise cross-correlation [e.g., Bensen et al., 2007], HVSR [e.g., Bard, 1999], or because they lay outside the region of interest (i.e. the Ijen caldera). Stations IPSW lays outside the map boundaries. See Table 5.3 for a complete description of the network. The gray shaded areas are the mean paths probed for the velocity models using ambient noise cross-correlation between pairs of seismic stations. The pink dots point the different volcanoes: 1-Jampit; 2-Ranteh; 3-Merapi; 4-Ringgih; 5-Blau; 6-Cemara; 7-Melaten; 8-Lingker; 9-Anyar; 10-Genteng; 11-Pendil; 12-Gelawan; 13-Kukusan; 14-Telaga Weru; 15-Widodaren; 16-Papak; 17-Kawah Ijen. B) Zoom zone on the Kawah Ijen volcano and locations of the permanent seismic network (inverted triangles with same color code as describe in A) and HVSR 20 minutes measurements (blue inverted triangles). The yellow line symbolized the path of major anthropic activity (mining and tourism). Others details are given on Fig.5.8. C) The location of the Ijen caldera on Java Island is given by grey square.

Shapiro et al., 2005]. To constrain the near-surface velocity structure, techniques based on micro-tremors correlation using small-aperture arrays such as the spatial autocorrelation (SPAC) [Aki, 1957] or frequency-wavenumber methods (f-k) [Capon, 1969, Lacoss et al., 1969] are largely employed [e.g., Chouet et al., 1998, De Luca et al., 1997, Ferrazzini et al., 1991, Perrier et al., 2012, Petrosino et al., 2012]. Depending on the aperture of the array, these techniques can recover the local 1D velocity structure for the first hundreds of meters below one point at the surface. In general, such techniques have poor horizontal resolution

due to difficulties in repeating the array measurements on an active volcano. There is therefore a trade-off between the recovery of the deep and the shallow velocity structure using traditional imaging techniques.

The ambient seismic-noise correlation techniques have overcome this limitation, particularly in the absence of earthquakes. Both deep and shallow structures can be imaged and the horizontal resolution depends mainly on the spatial distribution of the seismometers [Mordret et al., 2013a, Shapiro and Campillo, 2004, Shapiro et al., 2005, Stehly et al., 2009, Weaver, 2005]. The most recent theoretical developments in the ambient noise seismology framework have also led to link the geological structure with the records of ambient noise at a single station of 3 components [Sánchez-Sesma et al., 2011].

Actually, the horizontal to vertical spectral ratio (H/V) of the auto-correlated signal, computed slightly differently from its original version [Nakamura, 1989], has been found to be proportional to the ratio of the imaginary parts of the Green's functions at an observed location [Sánchez-Sesma et al., 2011]. Following this recent approach, the experimental H/V can be compared to its theoretical counterpart obtained from the calculation of theoretical Green's functions related to a layered elastic media. This allows considering the H/V inversion and then assessing local velocity structure [Sánchez-Sesma et al., 2011].

In this study, shallow and near-surface velocity models of the caldera were inferred performing cross-correlations of ambient seismic noise between pairs of stations and by applying the DEDHVR inversion. DEDHVR dominant-frequencies mapping also allows the characterization of the near-surface geology around Kawah Ijen crater.

This paper begins with a description of the main geological features of the Ijen caldera and the Kawah Ijen volcano. Subsequently, the data set and methods are detailed, and finally, the results are discussed in the light of previous studies.

5.4. Geological setting

5.4.1. The Ijen caldera complex

The Ijen Caldera Complex (ICC) belongs to the Sunda arc, which extends from Northwestern Sumatra to Flores. It is a consequence of the subduction of the Indo-Australian oceanic plate below the Eurasian continental plate [Handley et al., 2007, Lüschen et al., 2011, Smyth et al., 2007, Syracuse and Abers, 2006, Vigouroux-Caillibot, 2011]. The ICC

is a Pleistocene caldera of about 210 km^2 formed at least 50,000 years ago, after the collapse of the Old Ijen stratovolcano [Sitorus, 1990, Sujanto et al., 1988]. The caldera is bounded to the North by the Kendeng caldera wall and to the South by 3 post-caldera volcanoes (the Jampit, the Ranteh and the Merapi) aligned along the ICC's south circular rim and following the trend of the Jampit fault at the South-West of the ICC [Handley et al., 2007, van Hinsberg et al., 2010b] (Fig. 5.1). The Northern half of the caldera has no volcanic activity while the Southern part of the caldera contains 16 post caldera volcanic edifices globally aligned along an East-West trend extending from the Gunung Cemera volcano to the Kawah Ijen volcano. This lineation, almost parallel to the tectonic lineament, suggests a migration of the volcanic activity from West to East [Carn, 1999]. The Kawah Ijen volcano, sitting on the Western flank of the Merapi volcano, is located at the intersection between both, the circular rim volcano trend and the East-West post caldera volcanic lineament. Kawah Ijen is the youngest edifice and also the only presently active volcano of the Ijen caldera [Berlo, 2001, Sujanto et al., 1988, van Hinsberg et al., 2010a]. To the North, the presence of lacustrine sediments attests of the previous existence of a lake, today drained by a fault-bounded gap in the Kendeng caldera wall [Sujanto et al., 1988]. The main hydrological structure of the caldera is the Banyu Pahit acidic river, which takes its source several meters below the Kawah Ijen crater-lake.

5.4.2. Kawah Ijen crater features

Kawah Ijen crater has a regular elliptical shape (about 1.2 km by 1 km), probably resulting of two interlocking craters [Scher, 2012, van Hinsberg et al., 2010b]. The acidic crater-lake is bordered by steep cliffs rising 250 meters high, except on the western side where a break in the crater rim extends almost to the lake level [van Hinsberg et al., 2010b] and where a dam was constructed in the early 20th century [van Hinsberg et al., 2010a] in order to avoid the lake overflowing. Fig. 5.2 depicts the North crater walls along with a schematic log. The wall consists of thick lava flows covered by layered phreato-magmatic pyroclasts and air fall deposits interbeded with thin (about 1 to 7 meters) lava flows. The southeast inner flank of the crater has a gentler slope that exposes thicker lava flows and thinner horizontal pyroclastic layers [Delmelle and Bernard, 1994, Delmelle et al., 2000, G.G.L., 1921, Scher et al., 2013, Takano et al., 2004, van Hinsberg et al., 2010b]. Silica lacustrine superficial sediments cover an important part of the crater walls and attest to a former higher elevation of the lake.
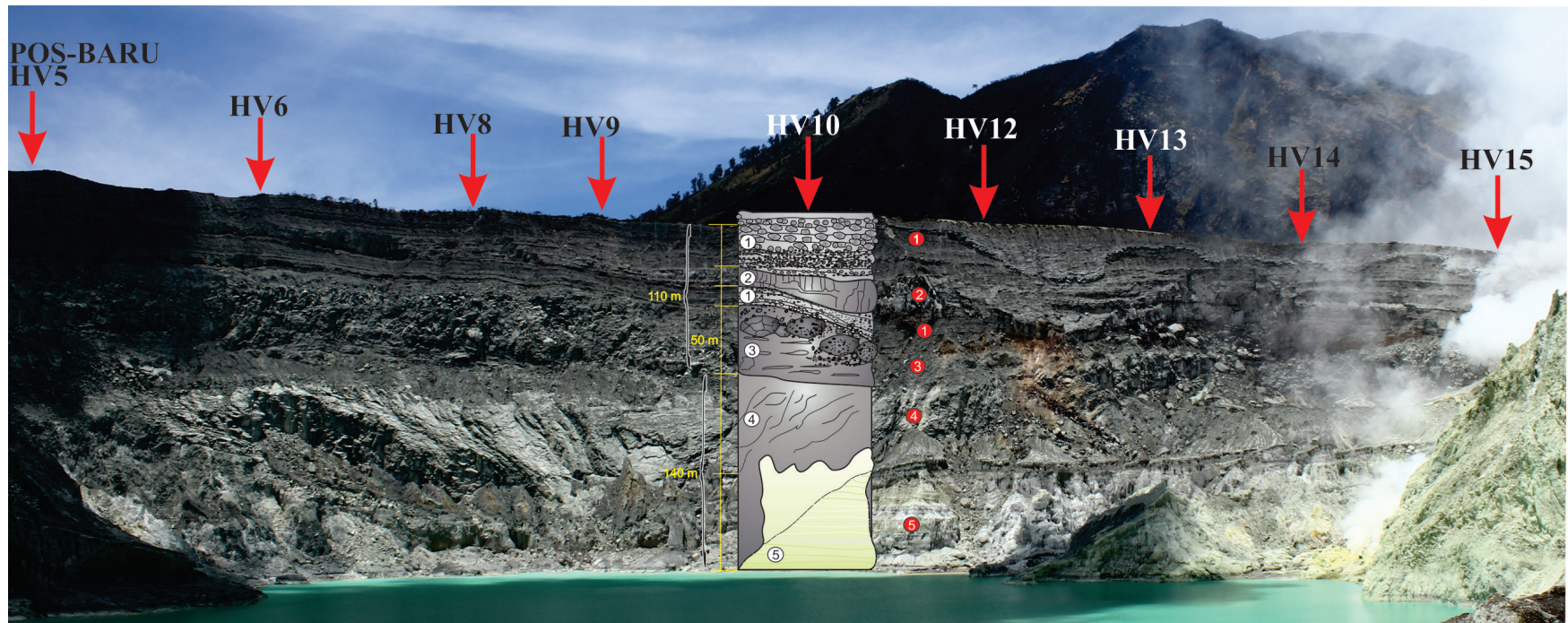
FIGURA 5.2: Kawah Ijen northern crater wall (POSBABU) profile and associated lithology 1) airfall deposits and scorias covered by a veneer of consolidated sulfur-bearing mud; 2) interbeded thin lava flow; 3) unconsolidated phreato-magmatic deposits; 4) Thick lava flows; 5) Silica lacustrine sediments. Red arrows indicate the place of the DEDHVR measurements on that part of the crater.

A veneer of consolidated sulfur-bearing mud, derived from recent fumarolic activities, covers the entire crater rim [van Hinsberg et al., 2010b]. On the outer slope of the volcano, a series of large and thick lava flows descends towards the northwest and bypasses the flanks of the Blau volcano [van Hinsberg et al., 2010a]. Between these lava flows, a layer of phreato-magmatic deposit is observed suggesting that the lake was present before the setting of the topmost lava flows [van Hinsberg, pers. com.]. Altered and fresh ballistics are abundant on the slopes of the volcano and flat summit areas. The path that leads up on the outer flank from Pondok (Fig. 5.1; shelter of sulfur minors, also named Kanteen) to the crater rim crosscuts scoria layers and small lava flows (up to 1 m thickness). Close to the rim it also crosscuts altered phreatic and phreatomagmatic materials lying discordantly on top of magmatic deposits [van Hinsberg et al., 2010b].

5.5. Instrumentation and data

5.5.1. Continuous recordings

Continuous recordings come from four different seismic networks (Fig. 5.1, Table 5.3). 1) The Indonesian Center for Volcanology and Geological Hazard Mitigation (CVGHM) permanent seismic network is composed by two Kinemetrics stations. One is installed in the south part of the crater rim and the other is close to the Raung volcano. None of these stations were used in this study due to strong band-pass filter on the data, probably between 1-10 Hz [Caudron, 2013]. 2) The Royal Observatory of Belgium (ROB) permanent seismic network is composed of three Trillium 120P broadband seismometers installed around Kawah Ijen volcano's crater since October 2010. A sampling rate of 100 Hz was chosen until July 2012 and was then increased to 200 Hz . 3) The ROB temporary network was composed of four Le-3Dlite sensors (natural period = 1 s) connected to a data acquisition system designed at ROB with a sampling rate of 125 Hz . These stations were installed inside and outside the caldera at six different sites for a few months. 4) The U.S. Geological Survey permanent seismic network (Volcano Disaster Assistance Program) is operational since May-June 2011 with four Mark seismometers (one L22-D three components sensor and three vertical component L4 sensor). A sampling rate of 100 Hz was used. All the permanent stations are telemetered to the Kawah Ijen observatory and all stations were GPS time synchronized. In this study, only the seismic stations located inside the caldera

were used since our goal is to obtain velocity models of the caldera or of the Kawah Ijen volcano.

5.5.2. DEDHVR survey

Temporal recordings of ambient seismic noise were also used in this study. They were performed by moving a single seismic station between October 8th and 24th 2010. A three-component Lennartz LE-3D with natural period of 5 seconds and a CITYSHARK digital acquisition system with a sampling rate of 100 Hz were used. When the sensor was installed on soft ground, a 1.2 cm buried-concrete plate was used in order to optimize the soil-sensor coupling [Bard and SESAME-team, 2004]. All recordings were performed during 20 minutes at the exception of the near fumarole sites where they were performed during 15 minutes. 87 measurements were achieved on different sites, all approximately spaced by 100 meters (Figs. 5.1 and 5.2). Recordings were acquired at the most convenient sites on the volcanic edifice (crater rim, large and narrow pathways). In order to minimize the anthropogenic noise contributions, measurements along the pathway to the crater rim (yellow path in Fig. 5.1) were performed on the quietest periods, i.e., on Friday (rest day for the miners) or late in the afternoon.

5.6. 4. Properties of background seismic noise at Kawah Ijen

Detailed temporal characterization of the noise background has been performed by the mean of continuous spectral seismic energy measurement and polarization analysis by Caudron [2013]. He concludes that, unless during volcanic crises, the tremor intensity, spectral contents, polarization and wavefield composition do not significantly change at Kawah Ijen volcano. Based on seismic energy release, three unrest periods have been identified at Kawah Ijen: during July-September 2010 (the first days of October were also affected), May 2011 and March 2012 [Caudron et al., 2015a]. Then, the field experiment has been conducted just at the end of the 2010 volcanic crisis when seismic activity was at its quiet background level.

At Kawah Ijen volcano, ambient seismic noise comes from anthropogenic and natural sources, as observed on the contrasting time pattern of noise amplitude calculated at permanent seismic stations PSG and PUN (Fig. 5.3). The noise amplitude was calculated
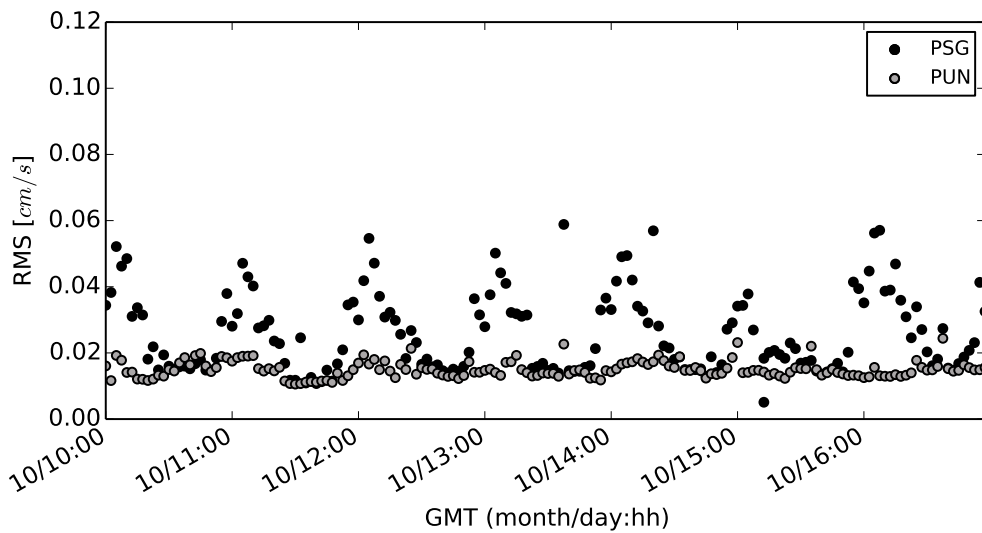
FIGURA 5.3: RMS of the noise background at seismic station PSG and PUN during the first week of the DEDHVSR experiment (October 2010). On Friday 15/01:10 lower amplitude of noise is observed. The signals used for this analysis were concomitant with the signals used for H/Vs spectral ratios. Refer to the text for details.

using the root mean square (RMS) over a moving window of 1-h long, previously filtered in the 0.5-20 Hz frequency band [Krischer et al., 2015]. On one hand, RMS noise amplitude at PSG clearly shows a 24-h periodicity with a daytime amplitude 3 times larger than nighttime. On the other hand, RMS noise amplitude at PUN presents an almost constant level between day and night. The periodicity observed at PSG is related to its vicinity with the most taken pathway that yields to the crater rim (yellow path in Fig. 5.1). The RMS noise amplitude is lower on Friday (sixth peak), which corresponds to the rest day for the miners at Kawah Ijen. The relative quietness observed at PUN is due to its distant position (more than 1 km) from any human activities. Same analysis for different frequency bands, showed that the contribution of anthropogenic sources is higher above 5 Hz (as in Bonnefoy-Claudet et al. [2006b]). Comparable PSG day-night pattern with comparable RMS amplification values have been observed at the Solfatara volcano, Italia [Petrosino et al., 2012] where ambient noise has been used to compute detailed HVSR studies.

5.7. Methods

Under an equipartitioned regime, the Green's function (GF) retrieval stems from averaging cross-correlations of recorded motions [e.g., Campillo and Paul, 2003, Gouédard et al.,

2008, Lobkis and Weaver, 2001, Sánchez-Sesma and Campillo, 2006, Wapenaar, 2004, Weaver, 2005]. Today, the GF retrieval from cross-correlation is henceforth a well-established method. Its principal application, the measure of surface wave velocities between two receivers, is described in the next subsection.

Historically, the computation of the horizontal to vertical spectral ratios (HVSR) from noise signals has been developed empirically [e.g., Bard, 1999]. Recent advances have shown that these ratios could also be computed following the same theoretical background used for retrieving GF from noise correlation [Sánchez-Sesma et al., 2011]. As a consequence, the computation of the experimental H/V ratios from GF is slightly different from the traditional HVSR computation. These discrepancies will be detailed in the section 5.7.2. Besides, the recent approach allows comparing the experimental H/V with their theoretical counterpart, H/V ratios obtained from the semi-analytical calculation of Green's functions related to a layered media allows, and then conducting the inversion of the experimental HVSR.

5.7.1. Ambient seismic noise cross-correlations

The main application of the ambient noise cross-correlation method is to retrieve the surface wave response between pair of stations and subsequently determine the surface wave velocity distribution of the subsurface (e.g., Strollo et al., 2015). Therefore, the ambient noise cross-correlation approach has been widely applied to compute surface-wave (Rayleigh and Love) tomography with dense seismic networks [e.g., Lin et al., 2008, Saygin and Kennett, 2010, Shapiro et al., 2005, Spica et al., 2014, Stehly et al., 2009]. However, when only few seismometers are available, as it is generally the case on volcanoes, the technique could rather be used to determine a 1-D S-wave velocity profile from the inversion of surface wave dispersion curves. Despite the presence of lateral heterogeneities, the 1-D velocity profile carries information about the average properties of the crust and can be considered as a good approximation of the velocity structure [e.g., Dziewonski and Hales, 1972, Ekström et al., 1997].

5.7.1.1. Cross-correlation functions

Cross-correlation functions (CCFs) were obtained by calculating the cross-correlation of the vertical component for daily time series of all concomitant station pairs installed
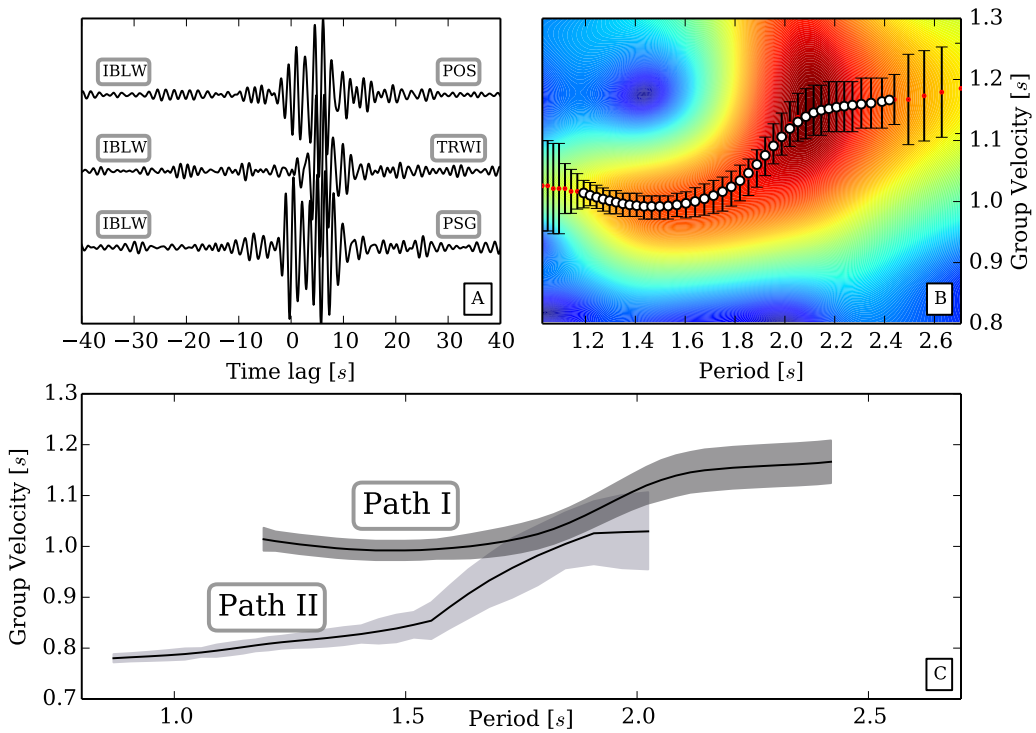
FIGURA 5.4: A) cross-correlation functions used for path I. B) Stacked FTAN diagram obtained for path I. C) Stacked dispersion curves and standard deviation for the two paths considered. Refer to the text for details.

inside the caldera. Since different sensor types were used (i.e., broadband and narrow-band seismometers), correction for instrumental responses was applied to the data. Each daily records was demeaned, detrended and downsampled to 20 Hz. Then, a temporal (1-bit) and spectral (whitening) normalization were applied [e.g., Bensen et al., 2007]. To enhance the signal-to-noise ratio (SNR), the daily cross-correlation functions were stacked over a time period ranging for 2 to 3 months depending on the data availability. Since only the vertical components of the seismograms were cross-correlated, the final CCFs are dominated by Rayleigh waves (Fig. 5.4A). CCFs (causal and anticausal) were finally folded in two on the middle and averaged to further enhance the SNR and to reduce the effect of source heterogeneity [e.g., Bensen et al., 2007, Sabra et al., 2005a]. The SNR is the ratio between the maximum amplitude of each CCF and the root-mean-square of its noisy part. Only CCFs with SNR superior to 8 were retained for dispersion measurements (i.e., 55 % of the CCFs).

5.7.1.2. Dispersion measurements

A Frequency Time Analysis (FTAN) [e.g., Dziewonski et al., 1969, Levshin et al., 1972] was computed in order to extract the group-velocity information of the fundamental mode of the Rayleigh wave as a function of frequency. It is known that the method can be biased by a systematic error [Levshin et al., 1989]. The resulting dispersion curves were selected manually, i.e., keeping these that vary smoothly in their period, and these for which the stations are separated by at least two wavelengths [Brenguier et al., 2007, Luo et al., 2015]. As our goal is to obtain mean velocity models of the caldera, a logarithmic stacking [Campillo et al., 1996, Shapiro et al., 1997] was applied to dispersion curves. This provides an improved measurement as it gathers the information from different records. Additionally, it allows calculating a standard deviation at each computed periods. Then, only dispersion curves that share similar proprieties (i.e., similar group velocities for a similar path) were selected. Since the strong heterogeneity of the caldera induces a great variety of measurements, and because of the strong quality criterion imposed (i.e., (1) selection of the best CCFs with a SNR greater than 8; (2) separation of the stations by at least two wavelengths; and (3) clearness, continuity and similarity of the Rayleigh wave dispersion curves), only 5 dispersion curves were retained for the stacking procedure. Fig. 5.4B and C show the stacked dispersion curves for the paths presented in Fig. 5.1. For path I (respectively path II), the inter stations distance is about 11 km (respectively 8 km) and the dispersion curve frequency band ranges from 0.4 to 0.8 Hz (respectively 0.5 to 1.15 Hz).

5.7.1.3. 1-D shear-wave velocity inversion

The shear wave velocity models were estimated from the stacked dispersion curves. Each stacked dispersion curve was inverted following the method proposed by Iglesias et al. [2001]. A simulated annealing algorithm was used to minimize the misfit value between observed and synthetic dispersion curves. The parameters considered for the inversion are the S-wave velocity and the thickness of the layers. Since no gravity map of the Ijen caldera exists, a classical crustal Poisson coefficient of 0.25 was supposed for all layers [Christensen, 1996] and the density ρ was computed from the following relation: $\rho = 0{,}32 V_P + 0{,}77$; where ρ is in g/cm^3 and the P-wave velocity V_P is in km/s [Berteussen, 1977]. The 100 best acceptable models are averaged to produce the final V_S model (Fig. 5.5).

In order to assess the sensibility of the surface wave to one of those models (path I), the

sensitivity kernels for the Rayleigh-wave fundamental mode were computed for the periods shown in Fig. 5B [Herrmann, 1996].

5.7.2. DEDHVR

Usual HVSR [Nakamura, 1989] is a widely-used method to determine the natural frequency of a site and to estimate simple velocity model of the subsurface (one layer over a half-space). However, the reason why this method gives good results has always been controversial due to the absence of clear theoretical basis and the lack of clarity on its interpretation. Actually, many studies on HVSR have been realized in order to clarify its strengths and limitations [e.g., Arai and Tokimatsu, 2004, Cara et al., 2010, Guéguen et al., 2007, Lachetl and Bard, 1994, Lermo and Chávez-García, 1993, Mucciarelli, 1998]. For example, it is not clear which waves compose the noise field that contributes to the H/V peak frequencies [e.g., Bonnefoy-Claudet et al., 2008, Malischewsky and Scherbaum, 2004, Nakamura, 2000].

A theoretical description of H/V ratios has been recently proposed [Sánchez-Sesma et al., 2011] using the diffuse field formalism. It is suggested that the HVSR recorded at a receiver could also be computed in terms of the imaginary part of the GF. By definition, the H/V ratio corresponds to the energy of the wavefield in the horizontal plane over the energy in the vertical direction in the frequency domain. At an observed location, these spectral energies, also designed as directional energy densities $\rho\omega^2|u_i(x,\omega)|^2$ (DED in Perton et al. [2009]), are proportional to the autocorrelation of the observed diffuse wavefield component for a given direction $|u_i(x,\omega)|^2$, which in turn are proportional, after average, to the imaginary part of the GF $Im(G_{ii}(x,x,\omega)) \propto \langle|u_i(x,\omega)|^2\rangle$. Here $G_{ii}(x,x,\omega)$ is the component of the GF corresponding to the displacement spectrum component $u_i(x,\omega)$ along the direction i generated by a source applied on direction i when source and receiver are superimposed at x and for frequency $f = 2\pi\omega$. Im refers to the imaginary part of the GF; the symbol $\langle\rangle$ corresponds to the average over several time windows. The directions 1 and 2 belong to the horizontal plan while component 3 is the vertical direction. The H/V ratio calculated from the DED are denoted in that case as the DEDHVR in order to differentiate it from classical HVSR. They can be expressed as follow:

$$\frac{H}{V}(x,\omega) = \sqrt{\frac{Im(G_{11}(x,x,\omega)) + Im(G_{22}(x,x,\omega))}{Im(G_{33}(x,x,\omega))}} = \sqrt{\frac{\langle|u_1(x,\omega)|^2\rangle + \langle|u_2(x,\omega)|^2\rangle}{\langle|u_3(x,\omega)|^2\rangle}},$$

(5.1)

Here, the equation requires that the averaging is done separately for all the components. By denoting the horizontal energy in a time window as $H_w = \rho\omega^2(|u_1(x,\omega)|^2 + |u_2(x,omega)|^2)$ and the vertical energy as $V_w = \rho\omega^2|u_3(x,\omega)|^2$, the equation (1) lets identify that the DEDHVR corresponds to the ratio of the averages: $H/V = \langle H_w\rangle/\langle V_w\rangle$. In that sense, it is different from the calculation of the usual HVSR [Nakamura, 1989] that corresponds to the average of the ratios: $H/V = \langle H_w/V_w\rangle$. Evaluating the ratio first allows the source deconvolution in each time window but remove the link with the GF. This deconvolution has also the disadvantage to create instabilities that should be overcame by applying a smoothing of V_w. In the DEDHVR, the source deconvolution is rather realized in each time window by applying the spectral whitening. This process is very stable and allows discussing the H/V ratios reliability with the same argument as for the reliability of the Green's function retrieved.

5.7.2.1.   Computation of the DEDHVRs

As for the calculation of GFs from cross-correlation, each time series of ambient noise was demeaned, detrended, bandpass filtered (0.1 to 10 Hz) and spectrally whitened. Since it has been observed that the 1-bit normalization does not allow retrieving the absolute amplitude of the GF [Larose et al., 2007], no 1-bit normalization was applied. Therefore this process slightly differs from the one applied for surface wave velocity assessment by cross-correlation. Then, the time series were sliced in window of 40 s duration with an overlap of 60 %, resulting in 70 windows for the 20 minutes measurement and in 52 windows for the 15 minutes measurements. Each window was tapered by a 5 % cosine function in order to prevent strong frequency leakage. Then, DEDHVR were finally calculated as indicated by the eq. 5.1. DEDHVR were also calculated with continuous recording from the ROB's networks (for stations PSG, IGEN, IPLA and IBLW). In that case, one day of continuous and quiet seismic noise (i.e., not during a volcanic crisis; Caudron et al. [2015a]) was selected. Same processing was applied but with 80 s windows in order to retrieve lower frequencies.

5.7.2.2. 1-D velocity inversion

DEDHVR are related to GF from eq. 5.1 and can be consequently inverted. We assumed here that GFs model the response at a source applied at the top free-surface of a stack of 1D elastic and boundless layers over a half-space. A method has been recently developed to calculate efficiently the DEDHVR for that geometrical configuration [García-Jerez et al., 2013]. It is used here for inversion in order to assess the local soil properties (V_P and V_S) and the thicknesses of the layers (h). Contrary to other DEDHVR inversions [Ducellier et al., 2013, Kawase et al., 2011], where GF are representative of body waves contribution only, the full wave field, surface and body waves, is here considered. The inversion method used a simulated annealing algorithm because of the numerous local minima and because of the relatively high cost that can be encountered with gradient method [Piña-Flores, 2015, Piña-Flores et al., 2014]. The cost function for n points in the spectrum is as follow:

$$\varepsilon = \sqrt{\frac{1}{n} \sum_{i=1,n} ([H/V]_{exp}(\omega_i) - [H/V]_{th}(\omega_i))^2} \tag{5.2}$$

When the full wave field is considered, simulations show that each peak of the DEDHVR corresponds to an impedance contrast so that the number of layers are taken to be approximately the number of peak plus one [Piña-Flores, 2015].

As for ambient noise cross-correlation measurements, only the seismic stations inside the Ijen caldera were used. Therefore, only 4 stations (Fig. 5.1) were considered for 1-D inversion. The others seismic stations have unreliable DEDHVR (i.e. no clear fundamental frequency peak) or have their location close to important lateral or topographical effect, such as at the rim of the crater (i.e. stations DAM, PUN, TRWI, POS, KWUI, IMLB; Fig. 5.1). As the direct problem used [García-Jerez et al., 2013] is set up for a stack of 1-D boundless layers, these measurements were not inverted [Matsushima et al., 2014]. The inversion of the DEDHVR measurements close to the crater rim would require an integration of this geometrical problem and therefore, is out of the scope of this contribution.

5.7.2.3. 2-D velocity profile

DEDHVR computed for the sites of the profile A-C were inverted (Fig. 5.8). The first 1-D velocity model was parameterized with a number of layers equal to the number of frequency peak plus one, but with the *a priory* layers thickness given by the observation of the

geology inside the crater rim (Fig. 5.2). This allows limiting the range of parameters used and therefore, the trade-off between velocity and layer thickness. Then, the best output model was used as the input model of the next inversion, providing a natural smoothing for the entire 2-D profile [e.g., Spica et al., 2015].

5.7.3.   Comparison with Nakamura's method

Since the method described in 5.7.2 is recent and involves a different data processing, a comparison with the well-established Nakamura's technique is proposed in the next section. For the Nakamura technique, each record was processed following the recommendations of the SESAME consortium [Bard and SESAME-team, 2004]. First, transients were removed from the time series using an anti-triggering module (STA/LTA). Then, the Fourier spectra were computed using 40 s non-overlapping time-windows tapered with a 5 % cosine function and smoothed using a logarithmic window function [Konno and Ohmachi, 1998] of 40 % relative bandwidth. Finally, the geometric means of the HVSR were calculated in the 0.1–10 Hz frequency band:

$$\frac{H^N}{V}(x,\omega) = \left\langle \frac{\sqrt{u_1^2(x,\omega) + u_2^2(x,\omega)}}{|u_3(x,\omega)|} \right\rangle. \tag{5.3}$$

5.8.   Results

5.8.1.   Ijen caldera

5.8.1.1.   1-D velocity models inferred from stacked dispersion curves inversion

For paths I and II, a five-layer (overlying a half-space) model was found to satisfactorily fit the observed group velocities. Fig. 5.5C and D display the obtained S-wave velocity models and the corresponding modeled dispersion curves are shown in Fig. 5.5A. For both paths, the fit between the observed and calculated dispersion curve are good (misfit <10-3). Both S-wave velocity profiles show some common similar characteristics. They present (1) a first layer with V_S of 870-970 m/s, followed by second layer that reach 530-820 m depth with velocities of 1230-1330 m/s. Then (2), it was found a block of three layers with V_s ranging between 1750 to 2240 m/s on top of (3) a half-space starting from 2830-3100 m depth that present V_S equal to 3300-3510 m/s. The main discrepancy between these
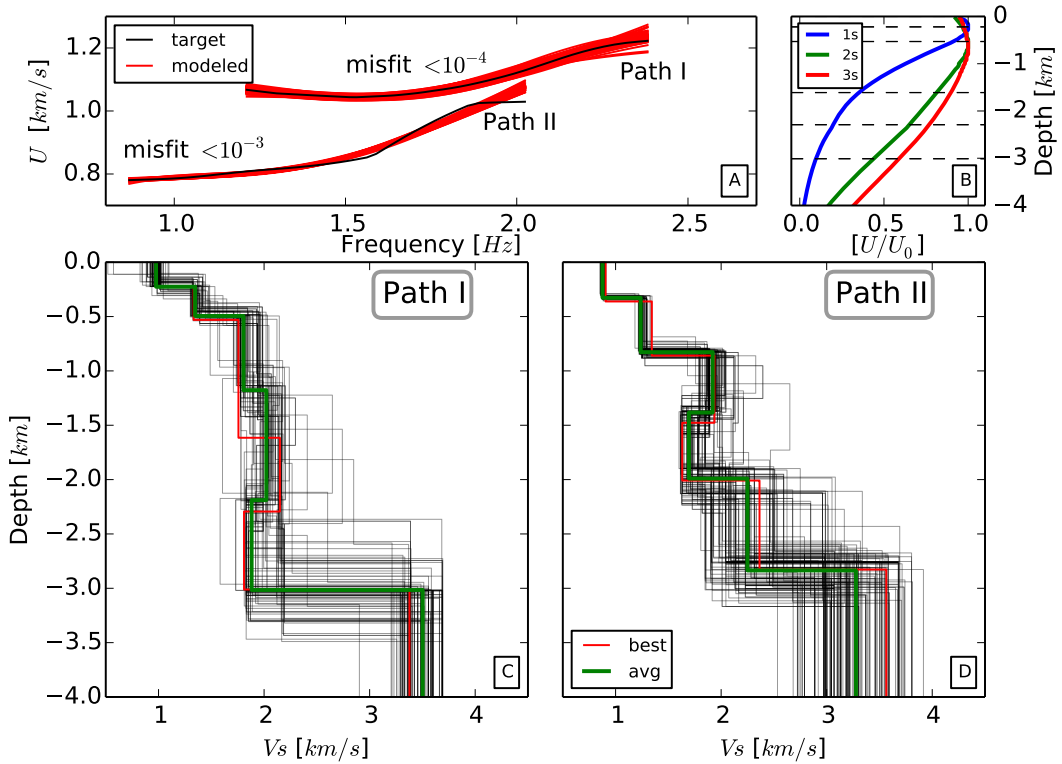
FIGURA 5.5: Results of the inversion of the dispersion curves obtained by ambient noise cross-correlation for path I and path II. A) 100 best modeled (red) and the measured (black) dispersion curves along with their minimum misfit values. The misfit value is calculated as the semblance between the synthetic and the data as in Iglesias et al. [2001]. B) Sensitivity kernels for the Rayleigh-wave fundamental mode calculated for the velocity model presented in C (path I) for 1, 2 and 3 s periods. C) and D) shear waves velocity models as a function of depth obtained by the inversion of the dispersion curves calculated for path I, II. Black lines are the 100 best models. Green line is the averaged velocity model for the 100 best models obtained. The red line is the last iteration's model (best misfit). Refer to the text for details.

models is observed at about 2000 m depth where a difference of about 500 m/s is detected for the S-wave velocity. Table 5.1 summerizes these observations.

5.8.1.2.   1-D velocity models inferred from DEDHVR

Fig. 5.6 presents the DEDHVR for the 4 stations selected along with their deduced velocity profiles and their misfit values, which are all inferior to 0.5. The depth of the last resolved layers reaches 250 m, except for PSG where a 3 km depth model was constrained. As the natural period of the stations IGEN, IPLA and IBLW is equal to 1 Hz , no low frequency

| Depths (km) | | V_S(km/s) | | |
Path I	Path II	Path I	Path II	*geological interp.*
0.22	0.32	0.97	0.87	Holocene Post-caldera deposits: tephra de-
0.53	0.82	1.33	1.23	posit composed mainly of ash fall and py-
				roclastic flow deposits with variable degree
				of consolidation.
1.61	1.38	1.75	1.97	Pleistocene Old Ijen: pre-caldera compo-
2.29	1.99	2.14	1.69	site cone stratified pyroclastic flows, lava
				flows and air fall deposits.
3.01	2.83	1.88	2.24	Miocene Basement rocks: clastic limesto-
∞	∞	3.3	3.51	nes interbeded with sandstone, clay and
				minor conglomerate.

CUADRO 5.1: Velocity models obtained from the inversion of stacked Rayleigh dispersion curves (Path I and Path II in Fig. 5.1). The last column refers to the geological interpretation described in the section 5.9.1 and based on Sujanto et al. [1988].

peak was considered to be representative to a velocity contrast during the inversion. Therefore, only the first 1000 of meters are shown. On the other hand, the broadband PSG's DEDHVR presents low frequency peaks of weak amplitude. One of these peaks was constrained by the inversion procedure. This led to model the interface with the half space at 2.8 km depth (Fig. 5.6).

All the velocity models present a very thin superficial layer of low velocity ranging between 350 and 600 m/s for the S-waves and between 600 and 1300 m/s for the P-waves. The thicker superficial layer, of about 18 m, is observed at IBLW, which is at the north of the caldera. IBLW profile is the only one to present a strong inversion of P-wave velocity between 100 and 250 m. This profile is also the more scattered for the P-wave velocity while the residual of the associated DEDHVR stays constant. This suggests that the V_p parameter may then be less constrained by the inversion procedure. We decided to not consider this velocity model for further interpretation.

The three velocity models obtained for the south part of the caldera (PSG, IGEN and IPLA) present similar pattern (Fig. 5.6), especially for the S-wave velocities. This pattern is characterized by a very thin superficial layer (about 10 m thick) of velocities inferior to 650 m/s, followed by a layer of 30-40 m thick (only for PSG, IPLA) with V_s velocity of 600-850 m/s, located above of 100-150 m thick layer with V_s ranging between 950-1300 m/s and on the top of a layer of 1450-1900 m/s. PSG also present a V_s contrast at about 240 m depth. This pattern is not as well repeated for the P-wave velocities that present greater variability through depth.
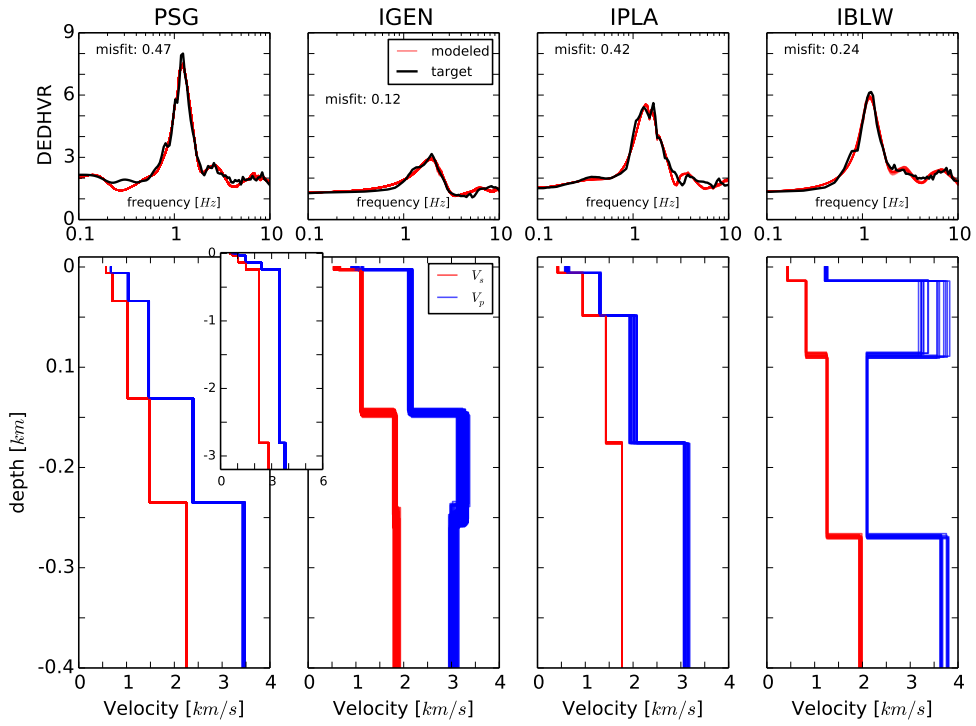
FIGURA 5.6: Results of the inversion of the DEDHVRs for stations PSG, IGEN, IPLA, IBLW (cf. Fig. 5.1). Top panels: measured (black line) and modeled DEDHVRs (red lines). Down panels: Best 30 V_s (red) and V_p (blue) velocity models obtained by the inversion process. Refer to the text for details.

5.8.2. Kawah Ijen volcano

5.8.2.1. Site effect analysis

The reliability of the DEDHVR curves and the clarity of each DEDHVR peaks were systematically controlled using the criterions proposed by Bard and SESAME-team [2004]. On 87 DEDHVRs sites, only 7 measurements were considered as unreliable and rejected. Examples of reliable and unreliable DEDHVR are presented in Fig. 5.7. It is also depicted that certain DEDHVRs present two important frequency peaks (f_0 and f_1) that according to Bonnefoy-Claudet et al. [2006a], Field and Jacob [1995] and Bard and SESAME-team [2004], correspond to distinctive resonant frequency of the site, respectively. In this case, both peaks are supposed to reveal a strong lithological interface at depth. 14 DEDHVRs present a secondary peak and 9 of them are observed at the beginning of the path that lead to the crater next to the seismic station PSG. A map of the DEDHVR fundamental peaks is presented on Fig. 5.8. All the unreliable measurements symbolized by a red cross are located on the path descending from the crater rim to the lake (near the fumarole) or near
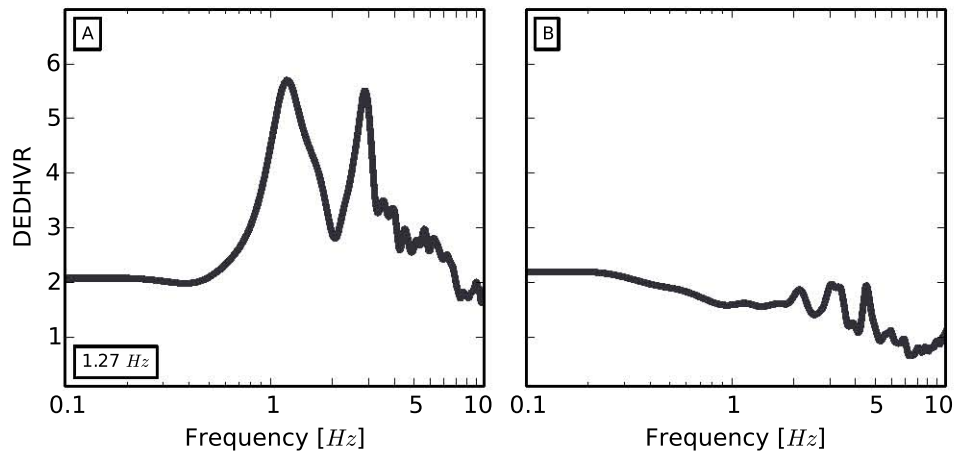
Figura 5.7: Examples of reliable (left) and unreliable (right) DEDHVR measurement. The reliable measurement refers to hv87 on the end of the A-C profile (Fig. 5.8) near PSG station. The unreliable measurement corresponds to hv61 near the sulfur fumarole (yellow star in Fig. 5.8). Refer to the text for details.
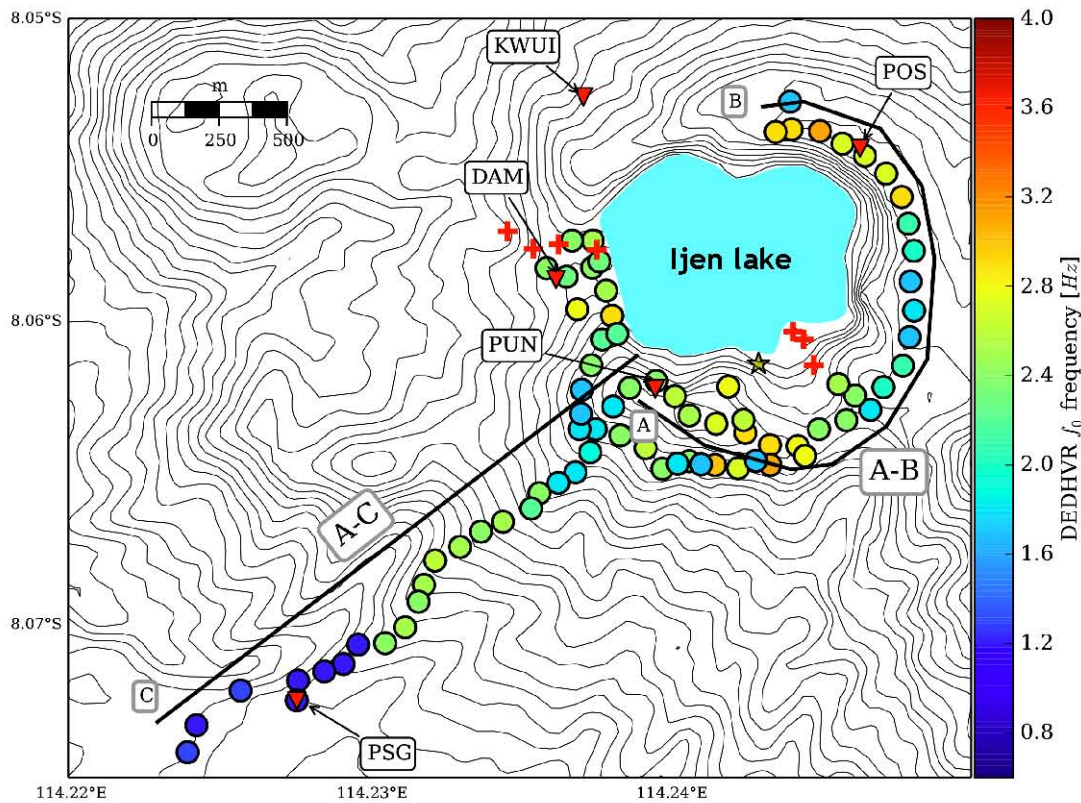
Figura 5.8: Site effect map at Kawah Ijen volcano. Colored dots symbolize DEDHVR measurements with their associate dominant frequency (Hz) reported on the color bar. Red crosses indicate unreliable measurements. Red inverted triangles represent permanent seismic stations. The yellow star symbolizes the sulfur fumarole. The dark lines symbolize profile A-B and A-C. Refer to the text for details.

the dam. They are interpreted as an important topographic effect [e.g., Chávez-García et al., 1997, 1996, Panzera et al., 2011] and/or an important concentration of water within the volcanic sediments. Indeed, both zones present chaotic topography and are located close to the Kawah Ijen crater-lake or directly up of a spring (great gypsum cascade) [e.g., Caudron et al., 2015a, Spica, 2011, van Hinsberg et al., 2010b]. The local non-horizontality of the lithological layers may also have led to unreliable measurements. However, this hypothesis is less likely as the great crater outcrop shows sub-horizontal layers at least near the crater rim (Fig. 5.2).

The fundamental resonance frequencies observed in Fig. 5.8 vary smoothly from one site to another except nearby PSG station where an important variation of the fundamental frequency is observed. This shift appears where DEDHVRs start to have two frequency peaks of high amplitude (see Figs. 5.7 and 5.8, Table 5.2). On the rim, above the fumarole, the pattern is slightly more complicated. Fig. 5.9 is a histogram of the fundamental resonance frequencies measured at Kawah Ijen volcano.

It shows a range of amplification for frequencies varying from 1.2 to 3.1 Hz with two dominant frequencies on 1.7 and 2.5 Hz. The amplitudes of the DEDHVR peaks are distributed in a range of 3.1 to 17, and most of them (58.6 %) are in the range 4–8, 20.7 % in the range 8–12, 10.3 % in the range 3-4 and 2.3 % above 12. No strong correlation between the peak frequency and its amplitude has been established. Table 5.2 summarizes these results along with the location of the measurements.
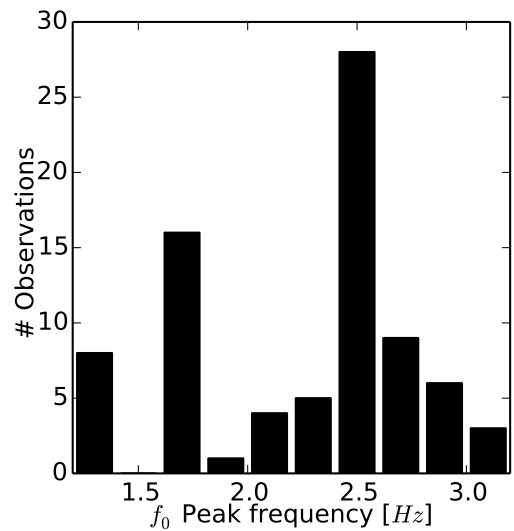
FIGURA 5.9: DEDHVR frequency dominant peak's histogram at Kawah Ijen volcano. Refer to the text for details.

5.8.2.2. 2-D model

Fig. 5.10 presents a 2-D velocity profile obtained by inverting 23 DEDHVRs along the path that yield to the crater (profile A-C in Fig. 5.8). This profile was created by juxtaposing all the 1-D velocity models both for V_s and V_p and no lateral smoothing was applied. No model has misfit value higher than 0.46 (see Fig. 5.6 for misfit illustration). All the 1-D

velocity models were determined down to a depth of 400 m and show three layers over a half-space. The superficial layer, 13 to 42 m thick, presents the lower velocities, 400–1100 m/s for the V_s and 560–1650 m/s for V_p. The second layer, 20 to 105 m thick, shows a distribution of the V_s velocities between 900 and 1450 m/s and V_p velocities between 1370 and 2220 m/s. The third layer presents the stronger variation both in thickness (60 to 250 m) and velocities (1220-2220 m/s and 1760-3170 m/s for V_s and V_p, respectively). The half-space presents velocities comprised between 2300-2760 m/s and between 3210-4010 m/s for the *S*- and *P*-waves respectively. The scattering of the velocities (σ) through the different models is higher for V_p than for V_s and always stays beneath 250 m/s.

5.8.3. Stability of DEDHVR and its consistency with the Nakamura's technique

Both for inversion and site effect characterization it is required to verify if a 20 minute long time series can be considered as a representative sample for the entire process and attest that daily cyclic variation of noise amplitude or small changes in the frequency content do not affect the stability of the DEDHVR. In other words: verifying if a 20 minutes recording ensures the statistical stabilization of the signal. Fig. 5.11 presents several DEDHVRs computed using 20 minutes of measurements every 4 hours during the first week of field experiment at PSG and PUN permanent stations. PSG (respectively PUN) has a fundamental frequency peak at 1.2 Hz (respectively 2.4 Hz) with average peak amplitude of 7.4 (respectively 12.3). Slight variations of these values occurred within a standard deviation interval of 0.02 and 0.16 % for the frequency peak and of 0.9 and 1.2 % for the peak amplitude for PSG and PUN respectively. Consequently, even if noise signals present clear variations, the short duration of the signal samples (20 minutes) does not affect the DEDHVR results and confirms the good stability of the measurements through time.

Fig. 5.12 illustrates the consistency between DEDHVR and Nakamura's method. It depicts 12 measurements along the POS profile (Fig. 5.2; profile A-B in Fig. 5.8), ordered row-wise from the north to south (clockwise in Figs. 5.2 and 5.8). All H/Vs (DEDHVR and Nakamura's) present a clear fundamental peak with amplitude superior or equal to 4. Fig. 5.13 illustrates the measurement differences due to the two methods for all the measurements for both the fundamental peak frequency and the amplitude.
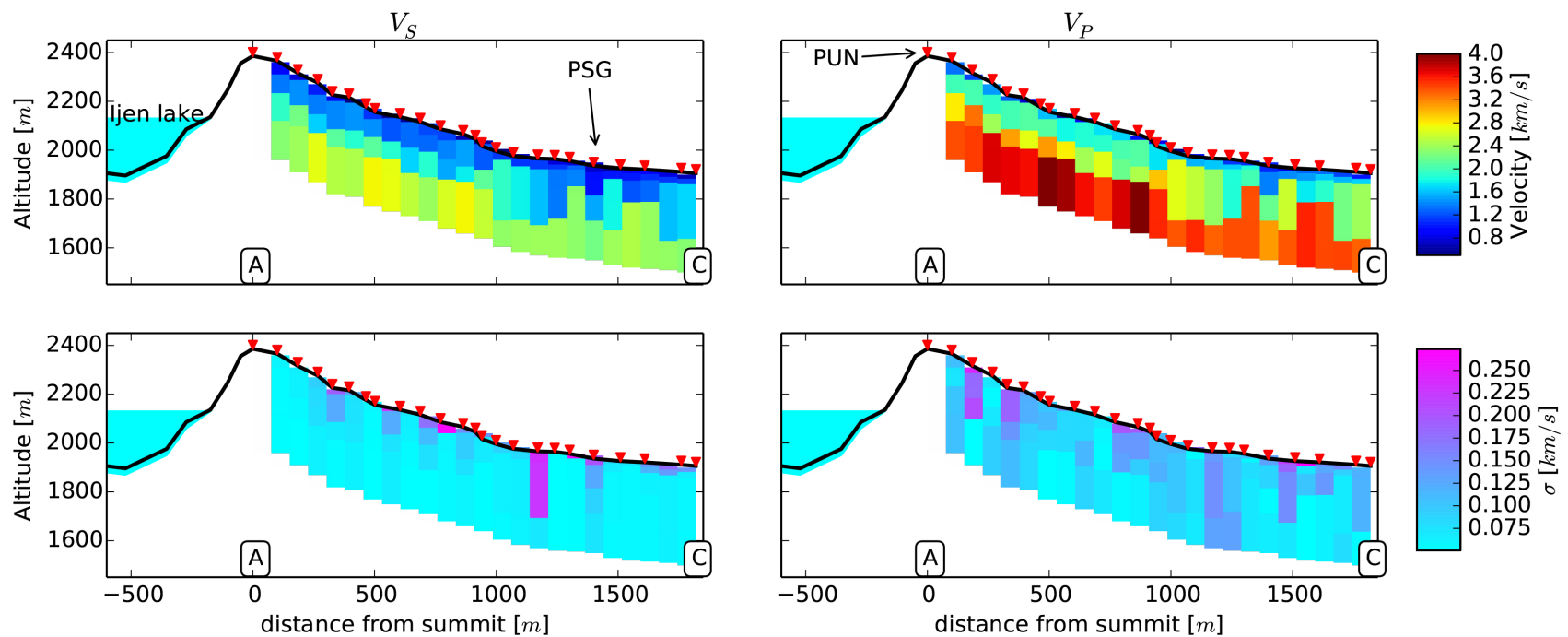
FIGURA 5.10: 2-D velocity profile obtained by inverting 23 DEDHVRs, all spaced by 100 m along the profile A-C (see Fig. 5.8). The two top panels depict the V_s (left) and V_p (right) velocity models. The corresponding velocity (color bar) is given respect to the lower misfit model for each site. The two down panels depict the variance in velocity between the 30 best models obtained, for each layer. The red inverted triangles symbolize the site where ambient seismic noise was recorded during 20 minutes.
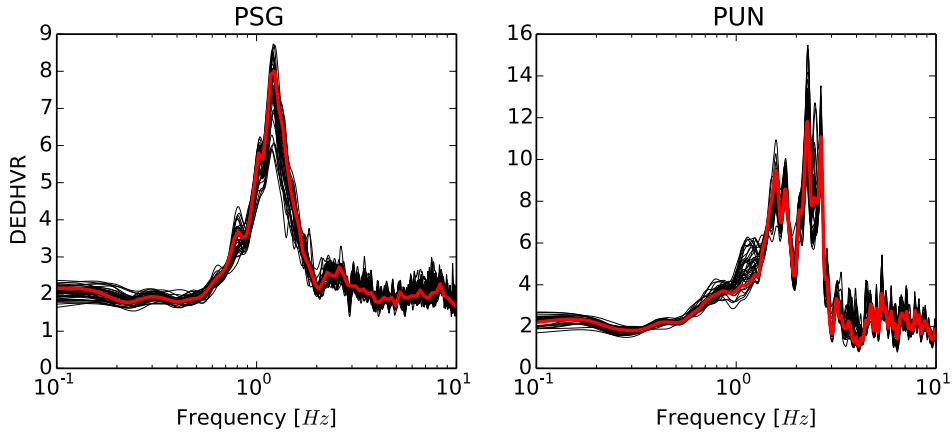
FIGURA 5.11: Stability of the DEDHVR expressed by the reproducibility of the measurements during the first week of the field experiment in October 2010 (cf., Fig. 3). Black DEDHVR are calculated using 20 minutes of measurements every 4 hours. Red DEDHVR is equal to the ratio of the mean all H on the mean all V (eq. 1). Refer to the text for details.

The fit between measurements obtained by both methods is good for the fundamental peak frequency values. It ranges in a 5 % error interval, which is smaller than the threshold values for stability conditions proposed by Bard and SESAME-team [2004] for equivalent frequency bands. Then, the frequency values calculated by DEDHVR can be considered as a reliable estimate of the fundamental frequency just as HVSR calculated by the Nakamura's technique. Regarding the amplitude, most of the measurements (76 %) calculated by DEDHVR have higher amplitude than those calculated by the Nakamura's technique. A comprehensive analysis of these discrepancies implies the full integration of all parameters affecting the H/V spectral ratios [e.g., Piña-Flores, 2015], which is out of the scope of this contribution.

5.9. Interpretations and Discussion

5.9.1. Caldera mechanical properties

The sensitivity kernels analysis illustrates that the models calculated from stacked dispersion curves are well resolved at least until 3 km depth where the sensibility of the surface wave is still superior to 50 % of its maximum at periods of 2 and 3 s. Beneath 3 km depth, the sensibility significantly decreases which likely explains the scattering of the model and could suggest a wrong assignation of the S-wave velocities from that depth. Furthermore, the exact location of the interfaces and the precise V_s velocity, cannot be perfectly resolved

by the inversion procedure because of the averaging imposed by the logarithmic stacking and the length of the paths crossed. Besides, the models derived from DEDHVR inversion
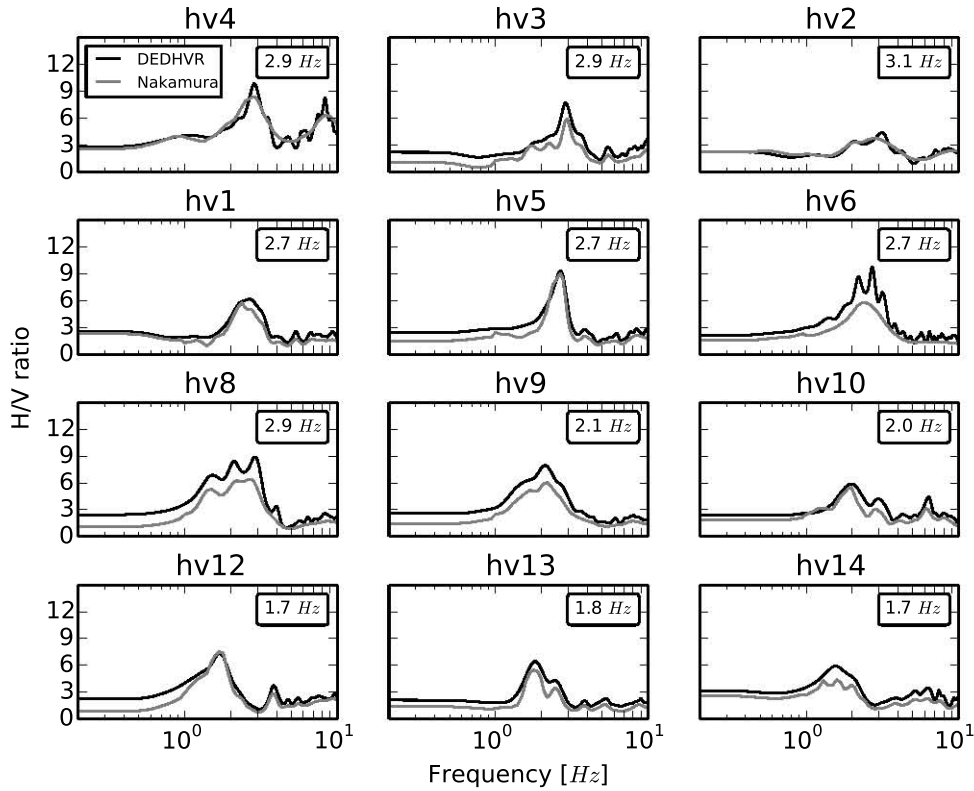
FIGURA 5.12: Consistency between the methods. The Black lines represent the DEDHVR measurements for the North crater wall (POS) profile; part of profile A-B in Fig. 8. The gray lines represent the HVSR computed by the traditional Nakamura's technique at the same sites. Refer to the text for details.

might help to give more confidence, and/or details to certain results obtained by dispersion curve's inversion. Even if a full 3-D velocity model or other geophysical observations would be required for a comprehensive interpretation, the different 1-D models obtained help to constrain the local volcanic structure. Based on these models, a refinement of the poorly known geological structure of the caldera [Sujanto et al., 1988] can be proposed (Table 5.1).

(1) A very thin (about 10 m) layer is observed at the three DEDHVR sites inside the caldera. Generally superficial volcanic stratums have very low V_s velocities (typically less than 500 m/s; i.e., Christensen [1982], Perrier et al. [2012] due to the presence of ash and unconsolidated air-fall deposits. It may therefore rely with the most resent volcanic activity inside the caldera.

(2) Both velocity models obtained from stacked dispersion curves and from DEDHVR

depict high V_s velocity for the shallow layers (i.e., with V_s ranging from 0.9 km/s to 2 km/s; Figs 5.5 and 5.6). The quick rise of the velocities suggests that consolidated materials such as lava flows, compacted scoria or phreatic deposits might dominate the shallow geology around the measured points. However, V_s structures obtained from DEDHVR are faster than those obtained from dispersion curves. The latter relies with the trade-off between resolution and sensitivity for each method. Indeed, stacked dispersion curves provide mean velocity models probed over several kilometers, while DEDHVR give local velocity models. Therefore, DEDHVR might highlight local high velocity body i.e., such as basaltic lava flows [e.g., Christensen, 1982]. Therefore, these shallow deposits might be interpreted as the Holocene post-caldera deposits, resulting from the last volcanic activities inside the caldera [Sujanto et al., 1988]. It is likely that

FIGURA 5.13: Differences between HVSR calculated from auto-correlation and from traditional Nakamura's technique for the fundamental frequency peaks and their amplitude. The frequency peaks are stable between the two methods while amplitudes show a more complicated pattern. Refer to the text for details.

those deposits have a thickness ranging between 500 to 800 m. The thinner thickness observed along path I model comparing to path II model is coherent with the caldera's geology and topography since volcanic deposits are less abundant on the Northern part of the caldera than on the Southern. Path I also includes most of the Kawah Ijen crater lake, which likely influences the thickness and/or the velocities of these layers.

(3) A block of 3 layers (overlying the half-space in Fig. 5.5) can be considered as a unique geological unit since the V_s contrasts between layers are weak. A constant velocity layer overlying the half-space at station PSG (Fig. 5.6) equally supports this interpretation. This unit can be related to the Pleistocene Old Ijen pre-caldera stratovolcano deposits. Small variation in the velocity (i.e., slight velocity inversion in Fig. 5.5) may result from the diversity of the deposits, alternating from stratified pyroclastic flows, lava flows or air falls. Sujanto et al. [1988] assumed that the pre-caldera deposits have a thickness of about 800 m. These present results suggest rather a thickness ranging from 1900 to 2400 m, which is comparable to the elevation of the Old Ijen volcano.

(4) The two velocity models obtained for path I and II present an interface with the half

space at about 2900 m depth. Such deep interface is also constrained by the inversion of DEDHVR at station PSG. This layer (Figs. 5.5 and 5.6), with the highest velocities (V_s velocities ranging from 2.9 to 3.5 km/s), is probably related to the Miocene basement rock. It consists of clastic limestone interbedded with sandstone, clay and minor conglomerate [Sujanto et al., 1988]. The average V_s velocity of such sedimentary layer at these depths is consistent with this interpretation [e.g., Christensen, 1982].

Although poor sensitivity of the surface wave at that depth for the periods inverted, the interface at 3 km depth is confirmed by two independent methods. This suggests that modeling DEDHVR low frequency might be meaningful even it is commonly accepted that usual H/V ratio measurements are only sensitive to the shallower layers [e.g., Bard, 1999, García-Jerez et al., 2007]. In such case, the depth resolution of the DEDHVR method is controlled by both, the geological structure itself (i.e., with strong velocity contrasts at depth) and the instrument capabilities.

5.9.2. Kawah Ijen shallow structure

Interpretations of the structures at Kawah Ijen volcano are based on DEDHVR measurements. For the path that yields to the crater, DEDHVRs were inverted allowing a quantitative discussion of the velocity structure. Instead, certain DEDHVRs were not inverted due to technical limitations; i.e., effects of the lateral heterogeneity inside the crater. In that case, the interpretation of the structure can solely be based over a qualitative site effect point of view.

We show in the next section that the vertical walls of the crater help to explain the site effects observed and that 2-D velocity profile can partially be explained by the same geological configuration.

5.9.2.1. Volcano crater shallow layers thickness estimate

At Kawah Ijen volcano, most of the DEDHVR measurements have a sharp peak with an amplitude factor superior or equal to 4 (e.g., Figs. 5.11 and 5.12, Table 5.2), supposing to indicate a strong horizontal impedance contrast [Bard, 1999, Bonnefoy-Claudet et al., 2006a]. Based on Fig. 5.2, the stronger impedance contrast should be observed at the interface between the phreatic/superficial deposits lying on the lava flows (layer 3 over layer 4 in Fig. 5.2). In fact, phreato-magmatic, pyroclasts and air fall deposits have slower V_s

than the denser lava flows [e.g., Christensen, 1982]. Additionally, the DEDHVR fundamental frequency peaks vary smoothly over short distances, letting assume a continuous thickness variation of the sub-horizontal lithological discontinuity. Because of the observed continuity of the geological stratum in Fig. 5.2, we suppose the velocity variation to be unimportant comparing with the thickness variation. If representing the whole structure
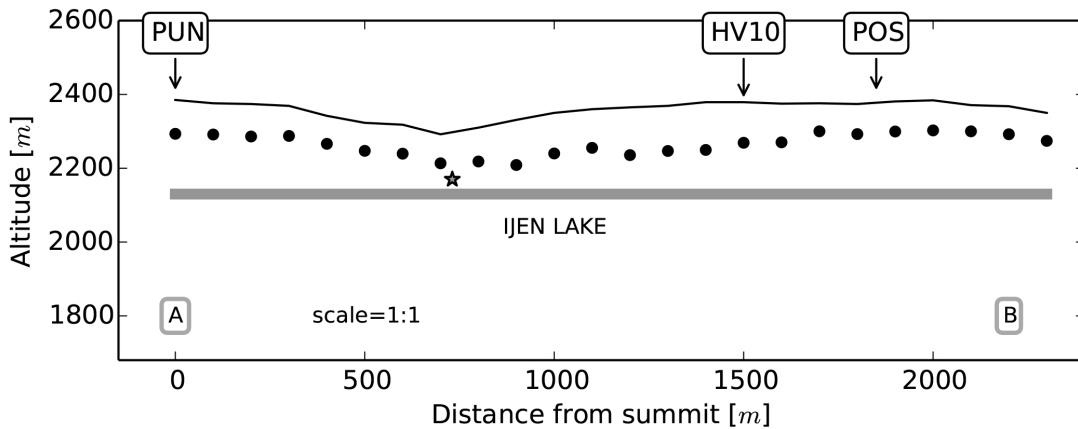
FIGURA 5.14: Interpolation of the superficial deposit along profiles A-B (top) and A-C (down). Using a first order approximation, the dominant frequency observed at each DEDHVR along the profiles and considering a shear wave velocity of 880 m/s, the black dots are drawn beneath the Kawah Ijen topography. These black dots are supposed to represent the depth of a lithological interface of strong impedance. The white dots are the representation at depth of a secondary peak using a similar approximation and a velocity (Vm) equal to 1100 m/s. On the top panel, the star symbolizes the sulfur fumarole and the horizontal grey line represents the height of the Kawah Ijen acidic lake. Both profiles are at scale 1:1. Refer to the text for details.

by a single layer on top of a half-space, the DEDHVR dominant frequency may be approximated by $F_0 = V_s/4H$, with H the layer thickness and V_s its shear-wave velocity [Ibs-von Seht and Wohlenberg, 1999, Parolai et al., 2002, Yamanaka et al., 1994]. Since the shallow sediment thickness beneath station hv10 is equal to 110 m (Fig. 5.2) and the DEDHVR peak frequency is equal to 2.0 Hz (Fig. 5.12, Table 5.2), the average V_s of the uppermost sediments is deduced to be equal to 880 m/s. This value is very consistent with the result obtained by inversion of the DEDHVR at the first station of the profile A-C (i.e., 850 m/s; Fig. 5.10), which is the closest from the crater rim. Similar superficial V_s have been also encountered inside the Ijen Caldera and are comparable with the work of Almendros et al. [2004] at Teide volcano, Spain.

Assuming the inferred velocity at hv10 is valid for all the stations around the crater, the lateral variation of the sediment thickness can be estimated. Fig. 5.14 depicts one profile inferred from those observations (A-B in Fig. 5.8).

For profile A-B, it can be deduced that the sediment thickness is fairly constant all around

the crater although it decreases slightly near the saddle above the sulfur fumarole. This observation is consistent with the crater geology since the topmost layers (overlying the lava flows) are thinner in that region.

For profile A-C, one peak (at about 2.4-2.8 Hz) is present from summit until 1000 m away. Then, a second peak arises (at about 1.2-1.3 Hz) and becomes at 1100 m the higher amplitude peak until the end of the profile (see Fig. 5.7, Table 5.2). The origin of the second peak (lower frequency) is due to the fact that along the end section of the A-C profile, the slopes of the volcano are almost horizontal and then almost parallel to the caldera floor. Because of this geometrical configuration, strong impedance contrast at deeper depth can be guessed.

This simple representation of the subsoil is fairly in agreement with the velocity models calculated by the inversion of DEDHVR as discussed in the next section.

5.9.2.2.   Volcano flank mechanical properties

Parameterization of the first 1-D velocity model (i.e., nearest PUN) was based on the crater s geology, limiting the uncertainty of this model. The layer thickness of the three first layers stayed close (+- 15 m) to the initial parameterization during the inversion. Therefore, the interpretation of the shallow structure can start from Fig. 5.2.

Considering the three first layers of the first 1-D model from a geological point of view, they may represent distinct volcanic deposits. As in the crater, it is likely that they correspond to the following sequence: airfall deposits over unconsolidated phreato-magmatic deposits, laying over a thick lava flow (Fig. 5.2). Over this model, the higher impedance contrast is observed between the phreato-magmatic deposits and the lava flow. This observation supports previous interpretation made in term of site effects (cf. 5.9.2.1). Although the half-space is characterized by the higher velocities, the impedance contrast with the overlying layer is weak. It likely means that the lava flow, visible inside the crater, lays over a body of similar physical proprieties (i.e., an other thicker lava flow).

Same pattern is repeated from the summit to 1000 m away from the crater. The latter lets assume that the geological sequence describe (Fig. 5.2) continues over part of the south flank of the Kawah Ijen crater. Some variations in layers thickness and velocities may be due to local heterogeneity slightly changing the shape of the DEDHVR over the profile. The velocity contrast between the third layer and the half-space becomes stronger away from the crater (especially for the V_p). It may be explained by a smaller influence of the

hydrothermal system, affecting the rock composition and porosity, on that part of the profile.

500 m before station PSG, DEDHVRs shape significantly change and secondary frequency peaks arise. Therefore, inversion results depict completely different 1-D models. No clear pattern can be identified likely meaning that the geological structure is more heterogeneous. Globally, the interface with the half-space has lower velocities than higher in the profile and, except for three models, its altitude is fairly constant. The mean elevation of the half-space on that part of the profile is coherent with the mean elevation of the caldera floor (i.e., about 1800 m). Therefore, this layer likely images the Holocene post-caldera deposits [Sujanto et al., 1988].

5.9.2.3.   Comparison with other volcanoes and limitations

Structure assessment from H/V spectral ratios interpretation is generally difficult to conduct in volcanic environments, which are normally characterized by strong geological heterogeneity. For example, Almendros et al. [2004] showed that the S-wave velocity and the layer thickness change considerably from site-to-site spaced by less than 300 m at Las Cañadas caldera (Spain). The H/V ratio measurements were difficult to interpret even with the help of detailed sub-surface geological studies because the layer thickness and the S-wave velocity have to be considered simultaneously. Others H/V studies that focused on volcanoes (or volcanic environments) evidenced short scale heterogeneities in spatial distribution of dominant frequency and therefore, were confronted to the same problem [Chávez-García et al., 2007, Mora et al., 2001, 2006, Nardone and Maresca, 2011, Tramelli et al., 2010]. Kawah Ijen volcano contrasts with these studies since the horizontality and homogeneity of the superficial layers (Figs. 5.2 and 5.10) allow taking full advantage of the method. Indeed, both Nakamura-like interpretation of the DEDHVRs and analysis of the 2-D model, conducted to similar conclusions. Although a composite volcano, certain parts of the Kawah Ijen crater likely present well defined bedding of the volcanic deposits, with only small local heterogeneities.

However, presuming that the layers of the volcano are actually horizontal and homogeneous is maybe an excessive simplification. For example, Fig. 5.10 clearly depicts that geological layers cannot be flat and that at some points the slope are quite pronounced. Furthermore, some sites are close to the crater rim, inducing strong lateral velocity contrast. In this particular case, a stack of 1-D elastic and boundless layers over a half-space is not the best

assumption. However, the stability of the main frequency peak along the profile as well as the great consistency of the results with the crater s geology give confidence to our results and interpretation.

5.10.   Conclusion

By applying a combination of two ambient seismic noise methods, several mechanical properties of the Ijen caldera and Kawah Ijen volcano have been revealed at different depths. Deep velocity profiles were obtained for the first three kilometers of the caldera by using the ambient seismic noise cross-correlation technique and the inversion of stacked dispersion curves. Shallow velocity models were also estimated using DEDHVR inversion both, at four seismometers inside the caldera and along a 2-D profile at Kawah Ijen volcano.

Inside the caldera, the quick rising of V_s velocities through depth suggest that consolidated volcanic materials might dominate the superficial geology, especially in the South of the caldera. The two methods do not provided consistent velocity models in terms of velocities or layer thicknesses. This is explained by the different sensibility of the methods: while stacked dispersion curves average the structure over several kilometer inside of the caldera, the DEDHVRs provide local velocity models. However, a deep interface at a depth of about 2900 m has been constrained by both methods. These models are used to improve the knowledge of the geological structure of the caldera.

The structure of the Kawah Ijen crater was first appreciated from the interpretation of the DEDHVR dominant frequencies. The relative simplicity of the geology and the horizontality of the superficial layers at Kawah Ijen crater allowed appreciating correctly the shallow structure of the crater. Then similar geological interpretation was used to partially explain the 2-D velocity model obtained for the flank of the Kawah Ijen volcano. Results suggest a simple volcanic structure with mostly smooth lateral variations. These results contrast with previous H/V studies on others stratovolcanoes, where measurements were difficult to interpret due to important short-distance heterogeneities.

This work represents the first application of the inversion of DEDHVR on a volcanic environment and shows the feasibility, under certain conditions, to constrain the structure down to a depth of 3 km. The method is very promising for the future of seismo-volcanology as most volcanoes observatories around the world do not have extended seismic network and therefore, are almost unable to assess for a reliable velocity model. This study showed

that the obtaining of a shallow velocity profile is feasible with only one three-components record of ambient noise and considering the full wavefield. Results also demonstrated that 20 minutes of ambient noise recording are stable enough to accurately determine the DEDHVR' just as the Nakamura's method. This opens new possibilities in regard to the imaging capabilities of the method. Indeed, as in this study, short recording could be repeated on several places around a volcano in order to constrain its detailed shallow velocity structure (2-D or 3-D).

5.11. Acknowledgments

5.12. Supplementary material

Name	Lat	Lon	Alt $_{(m)}$	F_0 $_{DEDHVR}$	A $_{DEDHVR}$	F_0 $_{Nakamura}$	A $_{Nakamura}$
.hv1.	-8.054123	114.245718	2384	2.7	6.2	2.6	5.
.hv2.	-8.05371	114.244973	2375	3.1	5.1	3	3.9
.hv3.	-8.053651	114.244032	2368	2.9	7.7	2.9	5.9
.hv4.	-8.053739	114.243499	2350	2.9	9.8	2.9	8.3
.hv5.	-8.054527	114.246466	2381	2.7	9.3	2.6	8.6
.hv6.	-8.055111	114.247168	2374	2.7	9.7	2.6	5.8
.hv8.	-8.05588	114.247688	2376	2.9	8.9	2.8	6.2
.hv9.	-8.056759	114.247908	2375	2.1	7.9	2.1	6.
.hv10.	-8.057652	114.248091	2379	2.	6.8	1.9	5.7
.hv12.	-8.058663	114.247977	2379	1.7	7.3	1.7	7.5
.hv13.	-8.059617	114.248102	2369	1.8	6.7	1.7	8.9
.hv14.	-8.060494	114.24710	2365	1.7	5.9	1.7	9.
.hv15.	-8.061435	114.247723	2362	2.1	6.5	2.1	5.5
.hv16.	-8.062143	114.247076	2350	2.	7.	2.	6.6
.hv17.	-8.062888	114.246652	2331	1.8	6.	1.8	5.5
.hv18.	-8.063229	114.245846	2310	2.4	7.1	2.4	7.1
.hv19.	-8.06408	114.244231	2318	2.8	7.	2.7	5.
.hv20.	-8.064051	114.243306	2323	2.9	12.	2.8	11.
.hv21.	-8.063646	114.242494	2342	2.9	15.	2.8	17.
.hv22.	-8.063223	114.242431	2339	2.6	7.7	2.6	5.9
.hv23.	-8.062124	114.241928	2323	2.8	6.2	2.8	5.4
.hv24.	-8.063348	114.241522	2369	2.7	8.2	2.7	9.1
.hv25.	-8.063073	114.240633	2387	2.5	8.9	2.7	7.1
.hv26.	-8.062442	114.240151	2376	2.6	7.1	2.5	7.6
.hv27.	-8.061937	114.239532	2379	2.4	10.	2.4	7.9
.hv28.	-8.062164	114.238648	2365	2.4	9.	2.5	7.1
.hv29.	-8.062779	114.238097	2314	1.8	9.	1.8	7.6
.hv30.	-8.063524	114.237521	2269	1.8	9.	1.7	10.
.hv31.	-8.063524	114.236983	2248	1.8	15.	1.8	10.
.hv32.	-8.06302	114.237029	2247	1.7	7.2	1.6	8.6
.hv33.	-8.062227	114.237056	2236	1.7	7.4	1.8	6.3
.hv34.	-8.061421	114.237373	2262	2.4	5.2	2.5	5.2
.hv35.	-8.060572	114.237742	2253	2.2	5.8	2.2	8.
.hv36.	-8.05979	114.238061	2231	2.9	5.4	2.9	7.4
.hv37.	-8.060388	114.238233	2247	2.2	4.	2.2	10.
.hv38.	-8.059577	114.236905	2197	2.8	9.4	2.8	4.
.hv39.	-8.058963	114.237871	2200	2.5	4.3	2.6	3.9
.hv40.	-8.058206	114.237403	2207	2.4	9.7	2.4	4.
.hv41.	-8.058505	114.236552	2210	2.3	8.4	2.3	4.9

Name	Lat	Lon	Alt (m)	F_0 DEDHVR	A DEDHVR	F_0 Nakamura	A Nakamura
.hv44.	-8.057316	114.237418	2160	2.5	9.4	2.4	3.6
.hv45.	-8.057316	114.2367	2190	2.4	7.8	2.4	4.1
.hv46.	-8.057436	114.236282	2157	nan	nan	nan	nan
.hv48.	-8.064287	114.237339	2142	1.9	6.2	1.8	10.
.hv49.	-8.063731	114.238345	2117	2.4	7.7	2.5	7.6
.hv50.	-8.06415	114.239184	2215	2.6	3.5	2.6	3.2
.hv51.	-8.064831	114.239729	2220	2.4	5.3	2.5	3.5
.hv52.	-8.06458	114.240626	2230	2.4	4.1	2.4	4.1
.hv53.	-8.064707	114.241482	2264	3.	4.5	3.	3.8
.hv54.	-8.06481	114.242246	2273	2.7	5.4	2.6	4.8
.hv55.	-8.064703	114.243324	2272	3.1	6.8	2.9	7.9
.hv56.	-8.064404	114.244473	2292	2.8	10.	2.7	8.3
.hv57.	-8.063524	114.244933	2250	2.4	5.2	nan	nan
.hv58.	-8.062419	114.246141	1997	2.4	5.	2.4	4.8
.hv59.	-8.062042	114.24558	2300	2.5	5.1	2.4	4.4
.hv60.	-8.061418	114.244767	2307	nan	nan	nan	nan
.hv61.	-8.060565	114.244429	2286	nan	nan	nan	nan
.hv62.	-8.06031	114.244083	2247	nan	nan	nan	nan
.hv63.	-8.064945	114.236846	2176	1.8	9.5	1.7	10.
.hv64.	-8.052741	114.243981	2130	1.7	6.8	1.6	6.
.hv65.	-8.064566	114.242847	2131	1.6	5.	1.6	4.2
.hv66.	-8.064566	114.242847	2130	1.7	4.7	1.7	2.8
.hv67.	-8.064684	114.241024	2134	1.7	6.7	1.7	3.9
.hv68.	-8.06466	114.240241	2210	1.8	7.3	1.8	6.6
.hv69.	-8.065293	114.236272	2345	1.8	3.9	1.8	7.4
.hv70.	-8.065633	114.235638	2290	2.4	6.5	2.4	5.8
.hv71.	-8.066135	114.235376	2271	2.2	5.5	2.2	5.9
.hv72.	-8.057622	114.237558	2269	nan	nan	nan	nan
.hv73.	-8.05758	114.23544	2267	nan	nan	nan	nan
.hv74.	-8.05711	114.234589	2169	nan	nan	nan	nan
.hv75.	-8.066575	114.234434	2149	2.5	6.2	2.4	5.1
.hv76.	-8.066899	114.233706	2132	2.4	6.4	2.5	4.9
.hv77.	-8.067403	114.233009	2164	2.5	6.9	2.4	6.4
.hv78.	-8.067849	114.232176	2145	2.5	4.7	2.8	3.7
.hv79.	-8.038352	114.231814	2122	2.6	6.	2.5	3.7
.hv80.	-8.069206	114.231632	2108	2.4	6.1	2.5	4.9
.hv81.	-8.070048	114.231186	2146	2.5	3.5	2.5	4.1
.hv82.	-8.070571	114.230522	2111	2.4	3.5	2.4	4.
.hv83.	-8.070621	114.229623	2083	1.2	4.2	1.2	4.5
.hv84.	-8.071261	114.229134	2063	1.2	4.5	1.2	5.
.hv85.	-8.071503	114.22850	2038	1.2	5.5	1.2	5.5
.hv86.	-8.071801	114.227625	2030	1.2	5.	1.2	4.1
.hv87.	-8.07213	114.225715	2015	1.3	5.3	1.3	5.1
.hv88.	-8.073271	114.224253	1997	1.2	3.5	1.2	4.2
.hv89.	-8.074163	114.223952	1995	1.3	3.4	1.3	5.7
.psgr.	-8.072455	114.227588	1853	1.2	7.4	1.2	4.

CUADRO 5.2: HVSR results (from DEDHVR and the Nakamura's method) obtained for the 87 sites around the Kawah Ijen volcano (Figs 5.1 and 5.8).

Network	Sta code	Loc	Lon	Lat	Alt	Instrument	Comp	Start	Stop
CVGHM	POS	Pos Licin	114.257	-8.1468	730	Kinemetrics	Z		
CVGHM	RNG	Raung volcano	114.1195	-8.1531	1370	Kinemetrics	Z		
ROB tmp	IBLW	Blawan	114.1672	-7.9933	1021	LE-3Dlite	Z-E-N	26/09/11	25/12/11
ROB tmp	IPSW	Pesaweran	114.2792	-7.9915	651	LE-3Dlite	Z-E-N	08/12/11	14/12/11
ROB tmp	IMLB	Malabar	114.1003	-8.0253	1530	LE-3Dlite	Z-E-N	29/09/11	19/11/11
ROB tmp	IPLA	Plalangan	114.1948	-8.037	1450	LE-3Dlite	Z-E-N	11/11/11	9/7/12
ROB tmp	IGEN	Genteng	114.1648	-8.0603	1500	LE-3Dlite	Z-E-N	07/12/11	5/4/12
ROB tmp	IPAL	Paltuding N	114.2057	-8.0548	1600	LE-3Dlite	Z-E-N	26/09/11	14/07/12
ROB tmp	IKLS	Robusta	114.2112	-8.059	600	LE-3Dlite	Z-E-N	28/09/11	29/09/11
ROB	POS	Posbaru (crater)	114.2463	-8.0543	2379	Trillium 120P	Z-E-N	10/10/10	
ROB	PSG	Crater flank	114.2276	-8.0725	1853	Trillium 120P	Z-E-N	06/10/10	
ROB	PUN	Puncak (crater)	114.2395	-8.0622	2330	Trillium 120P	Z-E-N	17/10/10	
ROB	DAM	Dam (crater)	114.2362	-8.0526	2208	Trillium 120P	Z-E-N	06/10/10	
USGS	TRWI	Puncak (crater)	114.2395	-8.0622	2330	L22D	Z-E-N	31/05/11	
USGS	MLLRI	Raung volcano	114.1195	-8.1531	1370	L4	Z	31/05/11	
USGS	POSI	Pos Licin	114.257	-8.1468	730	L4	Z	31/05/11	
USGS	KWUI	North crater	114.2371	-8.0526	2140	L4	Z	31/05/11	

Cuadro 5.3: Specifications of the different seismic instruments installed at Kawah Ijen.

Conclusiones generales

Se obtuvieron modelos de velocidad para las áreas volcánicas de Colima (Edo. de Colima, México), del Lazufre (Chile-Argentina) y del Ijen (Indonesia). En cada uno de los casos de estudio, los modelos de velocidad se obtuvieron mediante diferentes aplicaciones de las técnicas de correlación del RSA.

Para la zona del volcán de Colima, se elaboraron mapas tomográficos 2-D de velocidades de grupo de las ondas de Rayleigh a diferentes periodos, gracias a la extracción de las funciones de Green obtenidas por correlación cruzada del RSA y para diferentes pares de estaciones. La disposición de las estaciones sísmicas permitió evaluar las estructuras geológicas de los $\sim$30 primeros kilómetros de profundidad, con una resolución sin precedentes para esta zona. Esta investigación contrasta con los estudios previos, que solo pudieron obtener imágenes de la estructura profunda ($>\sim$60 km) de la zona, por medio de diversas técnicas sismológicas. En efecto, la parte más somera, donde ocurren la mayor parte de los fenómenos relacionados con la actividad volcánica, fue analizada por primera vez en esta investigación, gracias al potencial que ofrecen las técnicas de correlación del RSA. Los mapas obtenidos mostraron varias zonas de baja velocidad. Algunas de estas zones fueron asociadas a la actividad volcánica regional, como la cámara magmática del volcán de Colima, dentro de los $\sim$7 primeros km de la corteza o los depósitos eruptivos en superficie y presentes a lo largo de la franja volcánica trans-mexicana. También, se encontró una relación interesante entre las edades de los depósitos volcánicos y las profundidades de las anomalías de velocidad. Otras anomalías de baja velocidad más profundas se interpretaron como la cuña del manto a $\sim$35 km de profundidad o bien como la parte superior de las placas de Cocos y Riviera que subducen debajo de la placa Norteamérica, permitiendo confirmar que la placa de Cocos subduce con un ángulo mayor a la placa de Riviera.

En la área volcánica del Lazufre, se obtuvieron los mismos mapas tomográficos 2-D a diferentes periodos, los cuales se utilizaron para regionalizar las curvas de dispersión. Dichas curvas regionalizadas se invirtieron para construir un modelo de velocidad 3-D de las ondas S. En este caso, el uso de dos redes sísmicas diferentes, instaladas durante periodos de tiempo distintos, permitió aumentar la resolución alrededor del volcán Lastarria. El modelo 3-D obtenido, aunque con menor resolución en el sector Sur de la zona de estudio, permitió caracterizar la cámara magmática del volcán Lastarria. Para esta misma zona, otros estudios tomográficos que usaron los tiempos de arribo de ondas P o el análisis de función de receptores (*receiver functions*) no lograron obtener imágenes de la parte más superficial de la corteza y por tanto no fueron capaces de definir la ubicación de la cámara

magmática del volcán Lastarria [ver Heimann et al., 2013].

En el modelo 3-D, se identificaron dos anomalías de baja velocidad y de gran amplitud ubicadas entre la superficie y 7 km de profundidad debajo del volcán Lastarria, el único volcán activo del área. Estas anomalías fueron interpretadas como una cámara magmática que alimenta un reservorio hidrotermal rico en gases. La forma elongada a lo largo de un eje E-W de ambas anomalías y su ubicación justo en la orilla de la zona de levantamiento cortical, llevó a proponer un nuevo modelo para explicar la geodinámica local y como se formó la cámara magmática en este contexto. Una tercera zona de baja velocidad se interpretó como una posible consecuencia de la presencia de magma a mayor profundidad de la que se alcanzó a cartografiar y al origen del levantamiento de gran amplitud que sigue deformando la corteza terrestre en esta zona.

En la caldera del Ijen, tanto las curvas de dispersión obtenidas entre diferentes pares de estaciones, como el cociente espectral H/V calculado por auto-correlación del RSA se invertieron para obtener varios modelos de velocidad 1-D. Se mostró que una sencilla medición del ruido sísmico de apenas 20 minutos es suficiente para obtener un modelo de velocidad 1-D. Este resultado tiene importantes implicaciones para la sismología volcánica, ya que la mayor parte de los volcanes del mundo no disponen de un modelo de velocidad, haciendo difícil o imposible el análisis de las señales sísmicas para fines de monitoreo sísmico.

Los resultados principales del estudio consisten en la aplicación exitosa de métodos de correlación de ruido sísmico originales en un entorno volcánico y no tanto en la interpretación de las propiedades mecánicas de la zona estudiada. Los modelos de velocidad obtenidos se validaron gracias a la comparación con los afloramientos geológicos en el volcán, pudiéndose identificar varias estructuras geológicas importantes, tanto en el ámbito de la caldera como en el edificio volcánico. Por otra parte, la obtención de un mapa de efectos de sitio, permitió evidenciar las estructuras más someras del volcán Kawah Ijen. Así, a partir del estudio realizado, el volcán Kawah Ijen, uno de los más monitoreado de Indonesia, tiene su propio modelo de velocidad, el cual constituirá un punto de partida para investigación futuras enfocadas al análisis de la gran variedad de señales sísmicas registradas en esta zona.

Hasta la fecha, muy pocos trabajos se focalizaron en la aplicación de los métodos de correlación del RSA para la caracterización de volcanes. Los tres estudios de esta investigación permitieron demostrar que estos métodos presentan un amplio conjunto de ventajas para caracterizar áreas geológicamente complejas, con relación a técnicas tradicionales: (i) una

mejor resolución espacial que la obtención en estudios tomográficos realizados por análisis de terremotos; (ii) un mejor alcance para la obtención de imágenes de las estructuras volcánicas, especialmente en las partes más someras de la corteza donde suelen yacer los cuerpos magmáticos; (iii) necesidad de menor cantidad de datos y (iv) capacidad de obtención de imágenes de alta resolución de la corteza terrestre a varias escalas.

Por todo ello, se confirma que las técnicas de correlación del RSA son herramientas valiosas para complementar los estudios geofísicos y geológicos en zonas volcánicas.

Tanto para la elaboración de la herramientas numéricas utilizadas en esta investigación como para el acceso a los datos registrados y la divulgación de los resultados, se llevaron a cabo diversas colaboraciones entre centros de investigación de varios países: el Instituto de Ingeniería de la UNAM (México), el Observatorio Real de Bélgica, el *Institut de recherche pour le développement* (France), el GFZ (Potsdam, Alemania) y la *Université de Savoie* (Chambéry, France). Como resultado de estas colaboraciones quedan capacidades instaladas (técnicas y de computo) en el Instituto de Geofísica de la UNAM que podrán ser mejoradas y utilizadas para estudios futuros. De hecho, actualmente están siendo utilizadas.

Independientemente del resultado de los estudios en curso, las principales conclusiones de los estudios realizados en la presente investigación muestran que el RSA es una señal valiosa y práctica que presenta una gran cantidad de ventajas para poder caracterizar de manera fiable las estructuras corticales, desde las capas geológicas más superficiales hasta decenas de kilómetros de profundidad. Las técnicas de ruido son métodos versátiles con grand potencial para producir diversos resultados interesantes para la sismología volcánica y lo volcanología en general.

La información obtenida por el conjunto de técnicas aplicadas y desarrolladas es relevante para diversos especialistas de ciencias de la Tierra que trabajan en volcanes. En efecto, los resultados sobre la estructura interna de las zonas volcánicas estudiadas permitien aportar las bases para la comprensión de los procesos que pueden desarrollarse en el interior de los sistemas volcánicos, contextualizar estas características y por tanto facilitar los trabajos de monitoreo volcánico futuros los cuales permitirán evaluar el peligro y riesgo volcánico.

Procesamiento de datos

A.1. Correlación cruzada

Cuando se correlacionan series temporales de ruido se asume que para tiempos de observación largos, la distribución de las fuentes de ruido se promedia hacia una distribución aceptable con respecto a las espectativas teóricas discutidas en el capítulo 2 [e.g., Campillo et al., 2014, Sánchez-Sesma and Campillo, 2006]. Por lo tanto, uno de los mayores desafíos es el de disminuir la influencia de las fuentes locales de fuerte amplitud. Estas fuentes, generalmente « transitorias », pueden ser grandes terremotos, tormentas o varias otras fuentes en función de la gama de frecuencias considerada. El procesamiento de datos ha sido objeto de varios estudios y se han desarrolladas diversas estrategias para tratar de mejorar las correlaciones de ruido [e.g., Baig et al., 2009, Bensen et al., 2007, Lecocq et al., 2014, Poli et al., 2012b, Roux, 2009, Sabra et al., 2005a, Seats et al., 2012, Stehly et al., 2011]. No obstante, el procesamiento que se aplicará a los datos crudos depende de las finalidades deseadas (e.g., tomografía, monitoreo, atenuación, etc.).

Para mejorar la « estacionaridad » temporal de los registros, antes de correlacionarlos, la estrategia más intuitiva es la de remover todas las ventanas de tiempo que contienen terremotos. En efecto, las ondas directas de fuerte energía pueden contribuir a la generación

de una señal desprovista de sentido físico dentro de las correlaciones [Campillo et al., 2014]. Típicamente, la extracción de los terremotos de las series de tiempo se hace a través de un catálogo completo y/o con un algoritmo de detección tipo STA/LTA. Sin embargo, la implementación de este algoritmo puede ser difícil en un entorno volcánico ya que la mayoría de los eventos sísmicos no tienen ondas directas bien definidas. Además, la coda generada por estas ondas es una información valiosa para reconstruir la FG [e.g., Campillo and Paul, 2003], por lo tanto, un procesamiento de datos eficiente debe incluir esta parte de la señal. La solución es entonces normalizar la señal.

Campillo and Paul [2003] propusieron la normalización 1-bit, ya que permite equilibrar el decaimiento exponencial temporal de la intensidad de la coda. Desde entonces, la normalización 1-bit ha sido utilizada en numerosos estudios tomográficos que usan el ruido sísmico ya que es fácil de implementar y porque conserva la información de la fase [e.g., Brenguier et al., 2007, Cupillard et al., 2011, Kim et al., 2012, Saygin and Kennett, 2010, Shapiro and Campillo, 2004, Shapiro et al., 2005, Yang et al., 2007, Yao et al., 2006]. Cupillard et al. [2011] mostraron a través de simulaciones numéricas que la normalización 1-bit puede utilizarse también para estudios de atenuación. Además, diferentes autores propusieron otras normalizaciones temporales. Sabra et al. [2005a] por ejemplo introdujeron un procedimiento de recorte para limitar la contribución de los transitorios de gran amplitud; Bensen et al. [2007] aconsejaron usar un « running average » y Lecocq et al. [2014] propusieron usar un winsorizing [Tukey, 1962].

Bensen et al. [2007] sugieren usar ventanas de tiempo de 24 horas para calcular las correlaciones. Por otro lado, Prieto et al. [2011] y Poli et al. [2012b] proponen utilizar ventanas de tiempo cortas, de tan sólo 1 hora, de forma que los transitorios pueden eliminarse después de un análisis estadístico de la amplitud de la señal en todas las ventanas. Este último procesamiento evita sobre todo afectar los datos con un procesamiento no lineal.

Como el ruido sísmico no es plano en el dominio de la frecuencia (muestra picos claros en la banda del microsísmo; cf. capítulo 1, Fig 1.2), es importante también introducir un blanqueo espectral [e.g., Bensen et al., 2007, Shapiro et al., 2006]. Algunos autores intentaron mejorar la calidad del blanqueo usando un procesamiento elaborado de la señal [e.g., Baig et al., 2009, Schimmel et al., 2011, Stehly et al., 2011, Weemstra et al., 2014]. Generalmente, el blanqueo espectral es la operación más costosa computacionalmente.
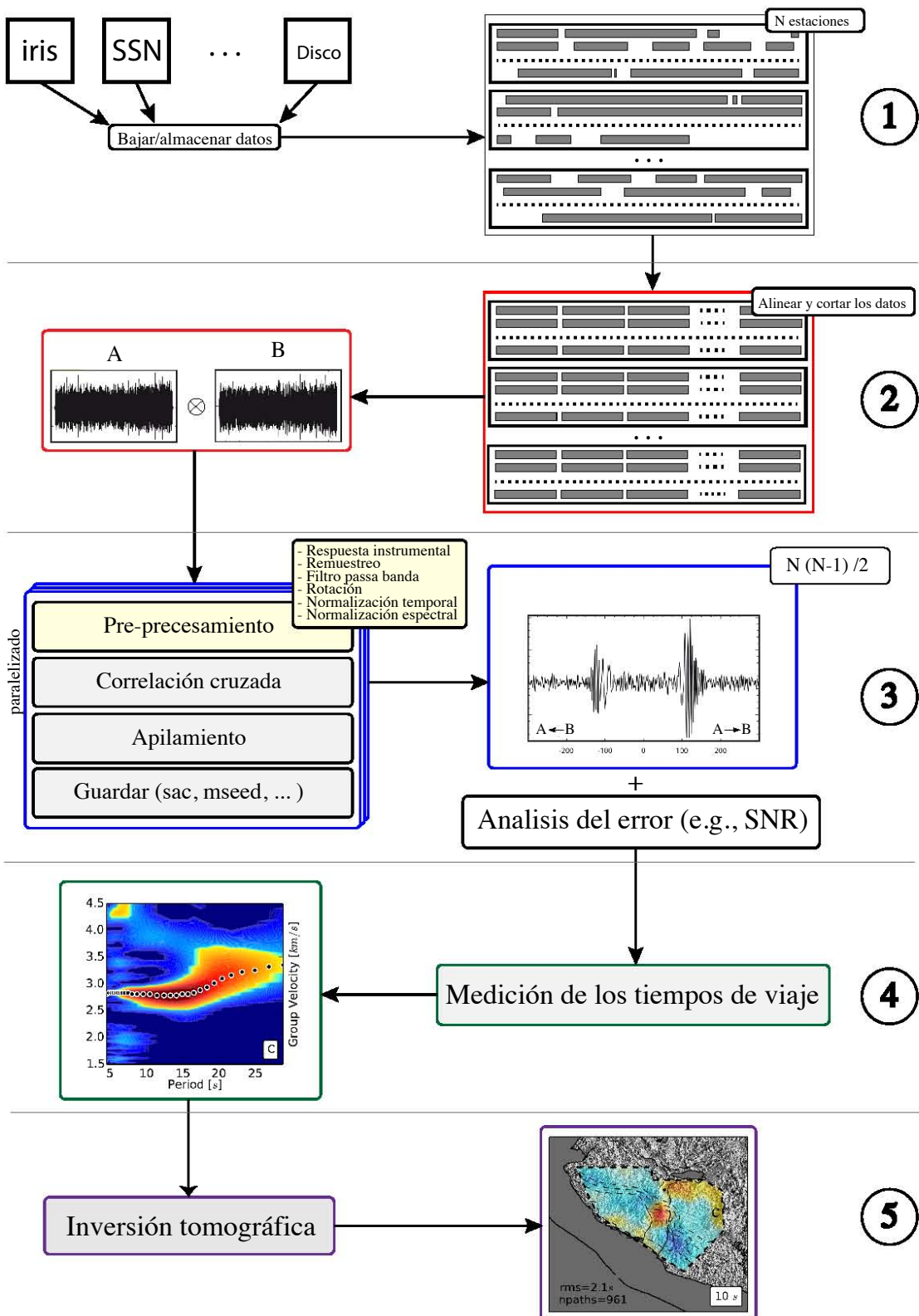
Figura A.1: Organigrama de las etapas del procesamiento de datos necesarias para obtener imágenes tomográficas. (1) Almacenamiento de los datos en una base de datos. (2) Alineamiento y recorte de los datos en archivos de x segundos. (3) Pre-procesamiento, correlación cruzada entre cada par de estaciones y análisis del error. (4) Cálculo de los tiempos de viaje entre cada par de estaciones. (5) Inversión tomográfica e interpretación de las imágenes. Una segunda inversión puede plantearse para obtener el campo de velocidad 3-D con las curvas de dispersión regionalizadas (cf. A.3).

A.1.1. El cálculo de las correlaciones

El cálculo de las correlaciones se realizó con un programa en lenguaje *Python* que se desarrolló a lo largo de esta tesis (con la ayuda inicial de Sebastian Heimann). El programa permite pasar de los datos crudos a las funciones de correlación finales (i.e., apiladas), sin etapas intermedias. El programa desarrollado puede utilizarse de manera intuitiva y fácil ya que lee casi cualquier tipo de archivo sísmico sin tomar en cuenta la arquitectura de clasificación de datos. Debido a que el procesamiento de correlación de ruido con redes densas necesita procesar una gran cantidad de datos, así como efectuar muchas operaciones, diversas funciones del programa fueron implementadas en paralelo para poder correr en un « cluster ». El procesamiento usado se acerca a lo propuesto por Bensen et al. [2007]. La figura A.1 resume las diferentes etapas necesarias para obtener el resultado final deseado; i.e. la tomografía.

En esta sección se describen las etapas realizadas por el programa de correlación - (3) en Figura A.1 - y en las secciones posteriores se comentarán las etapas (4) y (5).

En su versión más sencilla el código solo necesita una línea de comando y un fichero de entrada:

```
green_maker.py stations.txt
```

Dentro del código `green_maker.py` pueden modificarse manualmente varios argumentos. Los más importantes son:

Argumentos:	Funciones:
`stations = ['PPIG', PNIG']`	list of stations to compute
`components = ['ZZ', 'RR', 'TT']`	list of components to compute
`sampling_rate = 20`	goal sampling rate (Hz)
`win_lenght = 200`	window length (s)
`tmp_norm = '1bit'`	1-bit, winsorizing, normal_mean or None
`paz = True`	False | True instrumental response
`output_format = 'sac'`	sac, mseed, seisan, segy, etc...

El fichero `stations.txt` contiene la información siguiente:

net.sta	lat	lon	height	depth	instrument
LZ.LGG01.	-25.26690	-68.49464	4730	0	CMG3ESP
LZ.LGG15.	-25.18848	-68.62169	4287	0	T40
XP.LZAE.	-25.3074	-68.3992	4427	0	LZAE

Es importante mencionar que la última columna del fichero se refiere al tipo de sismómetro usado. Si

Bibliografía

Abbott, E. R. (2014). *Shallow seismicity patterns in the northwestern section of the Mexico subduction zone.* M.s. thesis, Miami University, Miami, Florida.

Aguilera, F., Tassi, F., Darrah, T., Moune, S., and Vaselli, O. (2012). Geochemical model of a magmatic–hydrothermal system at the lastarria volcano, northern chile. *Bulletin of Volcanology*, 74(1):119–134.

Aki, K. (1957). Space and time spectra of stationary stochastic waves, with spectral reference to microtremors. *Bull. Earthq. Res. Inst.*, 35:415–456.

Aki, K. (1969). Analysis of the seismic coda of local earthquakes as scattered waves. *Journal of geophysical research*, 74(2):615–631.

Aki, K. and Chouet, B. (1975). Origin of coda waves: source, attenuation, and scattering effects. *Journal of geophysical research*, 80(23):3322–3342.

Aki, K. and Richards, P. (2002). *Quantitative seismology.* University Science Book.

Almendros, J., Luzón, F., and Posadas, A. (2004). Microtremor analyses at teide volcano (canary islands, spain): Assessment of natural frequencies of vibration using time-dependent horizontal-to-vertical spectral ratios. *Pure and Applied Geophysics*, 161:1579–1596.

Anderssohn, J., Motagh, M., Walter, T. R., Rosenau, M., Kaufmann, H., and Oncken, O. (2009). Surface deformation time series and source modeling for a volcanic complex system based on satellite wide swath and image mode interferometry: The lazufre system, central andes. *Remote Sensing of Environment*, 113(10):2062–2075.

Andrews, V., Stock, J., Vázquez, C. A. R., and Reyes-Dávila, G. (2011). Double-difference relocation of the aftershocks of the tecomán, colima, mexico earthquake of 22 january 2003. *Pure and Applied Geophysics*, 168(8-9):1331–1338.

Aoki, Y., Takeo, M., Aoyama, H., Fujimatsu, J., Matsumoto, S., Miyamachi, H., Nakamichi, H., Ohkura, T., Ohminato, T., Oikawa, J., et al. (2009). P-wave velocity structure beneath asama volcano, japan, inferred from active source seismic experiment. *Journal of Volcanology and Geothermal Research*, 187(3):272–277.

Arai, H. and Tokimatsu, K. (2004). S-wave velocity profiling by inversion of microtremor h/v spectrum. *Bulletin of the Seismological Society of America*, 94(1):53–63.

Arroucau, P., Rawlinson, N., and Sambridge, M. (2010). New insight into cainozoic sedimentary basins and palaeozoic suture zones in southeast australia from ambient noise surface wave tomography. *Geophysical Research Letters*, 37(7).

Asten, M. W. (1978). Geological control on the three-component spectra of rayleigh-wave microseisms. *Bulletin of the Seismological Society of America*, 68(6):1623–1636.

Audet, P., Bostock, M. G., Christensen, N. I., and Peacock, S. M. (2009). Seismic evidence for overpressured subducted oceanic crust and megathrust fault sealing. *Nature*, 457(7225):76–78.

Baig, A. M., Campillo, M., and Brenguier, F. (2009). Denoising seismic noise cross correlations. *Journal of Geophysical Research: Solid Earth (1978–2012)*, 114(B8).

Bandy, W. L., Hilde, T. W. C., and Yan, C. Y. (2000). The rivera-cocos plate boundary: Implications for rivera-cocos relative motion and plate fragmentation. *Geological Society of America Special Papers*, 334:1–28.

Bard, P. Y. (1999). Microtremor measurements: a tool for site effect estimation. *The effects of surface geology on seismic motion*, 3:1251–1279.

Bard, P.-Y. and SESAME-team (2004). Guidelines for the implementation of the h/v spectral ratio technique on ambient vibrations measurements, processing and interpretations, SESAME european research project EVG1-CT-2000–00026, deliverable d23.12, available at http://sesame-fp5.obs.ujf-grenoble.fr.

Barmin, M., Ritzwoller, M., and Levshin, A. (2001). A fast and reliable method for surface wave tomography. In *Monitoring the Comprehensive Nuclear-Test-Ban Treaty: Surface Waves*, pages 1351–1375. Springer.

Battaglia, J., Zollo, A., Virieux, J., and Dello Iacono, D. (2008). Merging active and passive data sets in traveltime tomography: The case study of campi flegrei caldera (southern italy). *Geophysical Prospecting*, 56(4):555–573.

Bean, C., Lokmer, I., and O'Brien, G. (2008). Influence of near-surface volcanic structure on long-period seismic signals and on moment tensor inversions: Simulated examples from mount etna. *Journal of Geophysical Research: Solid Earth (1978–2012)*, 113(B8).

Bensen, G., Ritzwoller, M., and Yang, Y. (2009). A 3-d shear velocity model of the crust and uppermost mantle beneath the united states from ambient seismic noise. *Geophysical Journal International*, 177(3):1177–1196.

Bensen, G. D., Ritzwoller, M. H., Barmin, M. P., Levshin, A. L., Lin, F., Moschetti, M. P., Shapiro, N. M., and Yang, Y. (2007). Processing seismic ambient noise data to obtain reliable broad-band surface wave dispersion measurements. *Geophysical Journal International*, 169(3):1239–1260.

Bensen, G. D., Ritzwoller, M. H., and Shapiro, N. M. (2008). Broadband ambient noise surface wave tomography across the united states. *Journal of Geophysical Research: Solid Earth*, 113(B5):B05306.

Berlo, K. (2001). *The magmatic evolution of the Ijen caldera, East Java, Indonesia*. Unpublished MSc. thesis, University of Utrecht.

Berteussen, K. A. (1977). Moho depth determinations based on spectral-ratio analysis of NORSAR long-period p waves. *Physics of the Earth and Planetary Interiors*, 15(1):13–27.

Beyreuther, M., Barsch, R., Krischer, L., Megies, T., Behr, Y., and Wassermann, J. (2010). ObsPy: A python toolbox for seismology. *Seismological Research Letters*, 81(3):530–533.

Bianchi, M., Heit, B., Jakovlev, A., Yuan, X., Kay, S., Sandvol, E., Alonso, R., Coira, B., Brown, L., Kind, R., et al. (2013). Teleseismic tomography of the southern puna plateau in argentina and adjacent regions. *Tectonophysics*, 586:65–83.

Bonnefoy-Claudet, S., Cornou, C., Bard, P.-Y., Cotton, F., Moczo, P., Kristek, J., and Fah, D. (2006a). H/v ratio: a tool for site effects evaluation. results from 1-d noise simulations. *Geophysical Journal International*, 167(2):827–837.

Bonnefoy-Claudet, S., Cotton, F., and Bard, P.-Y. (2006b). The nature of noise wavefield and its applications for site effects studies: A literature review. *Earth-Science Reviews*, 79(3–4):205–227.

Bonnefoy-Claudet, S., Köhler, A., Cornou, C., Wathelet, M., and Bard, P.-Y. (2008). Effects of love waves on microtremor h/v ratio. *Bulletin of the Seismological Society of America*, 98(1):288–300.

Bostock, M. G., Hyndman, R. D., Rondenay, S., and Peacock, S. M. (2002). An inverted continental moho and serpentinization of the forearc mantle. *Nature*, 417(6888):536–538.

Brenguier, F., Campillo, M., Takeda, T., Aoki, Y., Shapiro, N., Briand, X., Emoto, K., and Miyake, H. (2014). Mapping pressurized volcanic fluids from induced crustal seismic velocity drops. *Science*, 345(6192):80–82.

Brenguier, F., Clarke, D., Aoki, Y., Shapiro, N. M., Campillo, M., and Ferrazzini, V. (2011). Monitoring volcanoes using seismic noise correlations. *Comptes Rendus Geoscience*, 343(8):633–638.

Brenguier, F., Shapiro, N. M., Campillo, M., Ferrazzini, V., Duputel, Z., Coutant, O., and Nercessian, A. (2008). Towards forecasting volcanic eruptions using seismic noise. *Nature Geoscience*, 1(2):126–130.

Brenguier, F., Shapiro, N. M., Campillo, M., Nercessian, A., and Ferrazzini, V. (2007). 3-d surface wave tomography of the piton de la fournaise volcano using seismic noise correlations. *Geophysical Research Letters*, 34(2):L02305.

Budach, I., Brasse, H., and Díaz, D. (2013). Crustal-scale electrical conductivity anomaly beneath inflating lazufre volcanic complex, central andes. *Journal of South American Earth Sciences*, 42:144–149.

Bussat, S. and Kugler, S. (2011). Offshore ambient-noise surface-wave tomography above 0.1 hz and its applications. *The Leading Edge*, 30(5):514–524.

Calò, M., Kinnaert, X., and Dorbath, C. (2013). Procedure to construct three-dimensional models of geothermal areas using seismic noise cross-correlations: application to the soultz-sous-forêts enhanced geothermal site. *Geophysical Journal International*, page ggt205.

Campillo, M., Margerin, L., and Shapiro, N. (1999). Seismic wave diffusion in the earth lithosphere. In *Diffuse waves in complex media*, pages 383–404. Springer.

Campillo, M. and Paul, A. (2003). Long-range correlations in the diffuse seismic coda. *Science*, 299(5606):547–549.

Campillo, M., Roux, P., Romanowicz, B., and Dziewonski, A. (2014). Seismic imaging and monitoring with ambient noise correlations. *Treatise on Geophysics*, pages 256–271.

Campillo, M., Singh, S. K., Shapiro, N. M., Pacheco, J., and Herrmann, R. (1996). Crustal structure of the mexican volcanic belt, based on group velocity dispersion. *Geofísica Internacional*, 35(4):361–370.

Capon, J. (1969). High-resolution frequency-wavenumber spectrum analysis. *Proceedings of the IEEE*, 57(8):1408–1418.

Cara, F., Giulio, G. D., Milana, G., Bordoni, P., Haines, J., and Rovelli, A. (2010). On the stability and reproducibility of the horizontal-to-vertical spectral ratios on ambient noise: Case study of cavola, northern italy. *Bulletin of the Seismological Society of America*, 100(3):1263–1275.

Carn, S. A. (1999). Application of synthetic aperture radar (SAR) imagery to volcano mapping in the humid tropics: a case study in east java, indonesia. *Bulletin of Volcanology*, 61(1-2):92–105.

Caudron, C. (2013). *Multi-disciplinary continuous monitoring of Kawah Ijen volcano, East Java, Indonesia*. Unpublished PhD thesis, Université Libre de Bruxelles, Brussels, Belgium.

Caudron, C., Lecocq, T., Syahbana, D. K., McCausland, W., Watlet, A., Camelbeeck, T., and Bernard, A. (2015a). Stress and mass changes at a'wet'volcano: example during the

2011–2012 volcanic unrest at kawah ijen volcano (indonesia). *Journal of Geophysical Research: Solid Earth*.

Caudron, C., Syahbana, D. K., Lecocq, T., Van Hinsberg, V., McCausland, W., Triantafyllou, A., Camelbeeck, T., Bernard, A., et al. (2015b). Kawah ijen volcanic activity: a review. *Bulletin of volcanology*, 77(3):1–39.

Cesca, S., Battaglia, J., Dahm, T., Tessmer, E., Heimann, S., and Okubo, P. (2008). Effects of topography and crustal heterogeneities on the source estimation of LP event at kilauea volcano. *Geophysical Journal International*, 172(3):1219–1236.

Chaussard, E. and Amelung, F. (2012). Precursory inflation of shallow magma reservoirs at west sunda volcanoes detected by insar. *Geophysical Research Letters*, 39(21).

Chávez-García, F. J., Domínguez, T., Rodríguez, M., and Pérez, F. (2007). Site effects in a volcanic environment: A comparison between hvsr and array techniques at colima, mexico. *Bulletin of the Seismological Society of America*, 97(2):591–604.

Chávez-García, F. J. and Luzón, F. (2005). On the correlation of seismic microtremors. *Journal of Geophysical Research: Solid Earth*, 110(B11):n/a–n/a.

Chávez-García, F. J., Rodríguez, M., Field, E. H., and Hatzfeld, D. (1997). Topographic site effects. a comparison of two nonreference methods. *Bulletin of the Seismological Society of America*, 87(6):1667–1673.

Chávez-García, F. J., Rodríguez, M., and Stephenson, W. R. (2005). An alternative approach to the spac analysis of microtremors: Exploiting stationarity of noise. *Bulletin of the Seismological Society of America*, 95(1):277–293.

Chávez-García, F. J., Sánchez, L. R., and Hatzfeld, D. (1996). Topographic site effects and HVSR. a comparison between observations and theory. *Bulletin of the Seismological Society of America*, 86(5):1559–1573.

Chouet, B., De Luca, G., Milana, G., Dawson, P., Martini, M., and Scarpa, R. (1998). Shallow velocity structure of stromboli volcano, italy, derived from small-aperture array measurements of strombolian tremor. *Bulletin of the Seismological Society of America*, 88(3):653–666.

Christensen, N. I. (1982). Seismic velocities. *Handbook of physical properties of rocks*, 2:1–228.

Christensen, N. I. (1996). Poisson's ratio and crustal seismology. *Journal of Geophysical Research: Solid Earth*, 101(B2):3139–3156.

Christensen, N. I. and Mooney, W. D. (1995). Seismic velocity structure and composition of the continental crust: A global view. *Journal of Geophysical Research: Solid Earth (1978–2012)*, 100(B6):9761–9788.

Chu, R., Helmberger, D. V., Sun, D., Jackson, J. M., and Zhu, L. (2010). Mushy magma beneath yellowstone. *Geophysical Research Letters*, 37(1):L01306.

Claerbout, J. F. (1968). Synthesis of a layered medium from its acoustic transmission response. *Geophysics*, 33(2):264–269.

Clarke, D., Zaccarelli, L., Shapiro, N., and Brenguier, F. (2011). Assessment of resolution and accuracy of the moving window cross spectral technique for monitoring crustal temporal variations using ambient seismic noise. *Geophysical Journal International*, 186(2):867–882.

Cowan, M., Page, J., and Weitz, D. (2000). Velocity fluctuations in fluidized suspensions probed by ultrasonic correlation spectroscopy. *Physical review letters*, 85(2):453.

Cox, H. (1973). Spatial correlation in arbitrary noise fields with application to ambient sea noise. *Journal of the Acoustical Society of America*, 54(5):1289–1301.

Cruz-Atienza, V. M., Pacheco, J. F., Singh, S. K., Shapiro, N. M., Valdés, C., and Iglesias, A. (2001). Size of popocatepetl volcano explosions (1997–2001) from waveform inversion. *Geophysical Research Letters*, 28(21):4027–4030.

Cupillard, P., Stehly, L., and Romanowicz, B. (2011). The one-bit noise correlation: a theory based on the concepts of coherent and incoherent noise. *Geophysical Journal International*, 184(3):1397–1414.

De Barros, L., Pedersen, H. A., Métaxian, J.-P., Valdés-Gonzalez, C., and Lesage, P. (2008). Crustal structure below popocatépetl volcano (mexico) from analysis of rayleigh waves. *Journal of Volcanology and Geothermal Research*, 170(1–2):5–11.

de Kool, M., Rawlinson, N., and Sambridge, M. (2006). A practical grid-based method for tracking multiple refraction and reflection phases in three-dimensional heterogeneous media. *Geophysical Journal International*, 167(1):253–270.

De Luca, G., Scarpa, R., Del Pezzo, E., and Simini, M. (1997). Shallow structure of mt. vesuvius volcano, italy, from seismic array analysis. *Geophysical Research Letters*, 24(4):481–484.

de Ridder, S. and Dellinger, J. (2011). Ambient seismic noise eikonal tomography for near-surface imaging at valhall. *The Leading Edge*, 30(5):506–512.

de Ridder, S., Papanicolaou, G., and Biondi, B. (2009). Kinematics of iterative interferometry in a passive seismic experiment. In *79th Annual Meeting, Society of Exploration Geophysicists, Houston, USA, Expanded Abstracts*, volume 28.

Delmelle, P. and Bernard, A. (1994). Geochemistry, mineralogy, and chemical modeling of the acid crater lake of kawah ijen volcano, indonesia. *Geochimica et Cosmochimica Acta*, 58(11):2445–2460.

Delmelle, P., Bernard, A., Kusakabe, M., Fischer, T. P., and Takano, B. (2000). Geochemistry of the magmatic–hydrothermal system of kawah ijen volcano, east java, indonesia. *Journal of Volcanology and Geothermal Research*, 97(1–4):31–53.

DeMets, C. and Traylen, S. (2000). Motion of the rivera plate since 10 ma relative to the pacific and north american plates and the mantle. *Tectonophysics*, 318(1–4):119–159.

Denolle, M., Dunham, E., Prieto, G., and Beroza, G. (2013). Ground motion prediction of realistic earthquake sources using the ambient seismic field. *Journal of Geophysical Research: Solid Earth*, 118(5):2102–2118.

Denolle, M., Dunham, E., Prieto, G., and Beroza, G. (2014). Strong ground motion prediction using virtual earthquakes. *Science*, 343(6169):399–403.

Derode, A., Larose, E., Campillo, M., and Fink, M. (2003a). How to estimate the green's function of a heterogeneous medium between two passive sensors? application to acoustic waves. *Applied Physics Letters*, 83(15):3054–3056.

Derode, A., Larose, E., Tanter, M., Rosny, J. d., Tourin, A., Campillo, M., and Fink, M. (2003b). Recovering the green's function from field-field correlations in an open scattering medium (l). *The Journal of the Acoustical Society of America*, 113(6):2973–2976.

Díaz, D. and Zamudio, F. (under review). 3-d resistivity model of the lastarria volcano (northern chile) and evidences of a large scale conductive anomaly beneath the back-arc. *Geophys. Res. Lett.*

Dougherty, S. L., Clayton, R. W., and Helmberger, D. V. (2012). Seismic structure in central mexico: Implications for fragmentation of the subducted cocos plate. *Journal of Geophysical Research (Solid Earth)*, 117:9316.

Draeger, C., Cassereau, D., and Fink, M. (1995). Time reversal of ultrasonic waves in solids: Theory and experiments. *The Journal of the Acoustical Society of America*, 98(5):2875–2875.

Ducellier, A., Kawase, H., and Matsushima, S. (2013). Validation of a new velocity structure inversion method based on horizontal to vertical (h/v) spectral ratios of earthquake motions in the tohoku area, japan. *Bulletin of the Seismological Society of America*, 103(2A):958–970.

Duputel, Z., Ferrazzini, V., Brenguier, F., Shapiro, N., Campillo, M., and Nercessian, A. (2009). Real time monitoring of relative velocity changes using ambient seismic noise at the piton de la fournaise volcano (la réunion) from january 2006 to june 2007. *Journal of Volcanology and Geothermal Research*, 184(1):164–173.

Duvall, T. L., Jeffferies, S. M., Harvey, J. W., and Pomerantz, M. A. (1993). Time–distance helioseismology. *Nature*, 362(6419):430–432.

Dziewonski, A., Bloch, S., and Landisman, M. (1969). A technique for the analysis of transient seismic signals. *Bulletin of the Seismological Society of America*, 59(1):427–444.

Dziewonski, A. and Hales, A. (1972). Numerical analysis of dispersed seismic waves. *Seismology: surface waves and earth oscillations*, 11:39–85.

Dzurisin, D. (2006). *Volcano deformation: new geodetic monitoring techniques*. Springer Science & Business Media.

Ekström, G., Abers, G. A., and Webb, S. C. (2009). Determination of surface-wave phase velocities across usarray from noise and aki's spectral formulation. *Geophysical Research Letters*, 36(18).

Ekström, G., Tromp, J., and Larson, E. W. F. (1997). Measurements and global models of surface wave propagation. *Journal of Geophysical Research: Solid Earth*, 102(B4):8137–8157.

Fan, Y., Snieder, R., Slob, E., Hunziker, J., Singer, J., Sheiman, J., and Rosenquist, M. (2010). Synthetic aperture controlled source electromagnetics. *Geophysical Research Letters*, 37(13).

Fang, L., Wu, J., Ding, Z., and Panza, G. F. (2010). High resolution rayleigh wave group velocity tomography in north china from ambient seismic noise. *Geophysical Journal International*, 181(2):1171–1182.

Ferrari, L., Orozco-Esquivel, T., Manea, V., and Manea, M. (2011). The dynamic history of the trans-mexican volcanic belt and the mexico subduction zone. *Tectonophysics*, 522–523:122–149.

Ferrari, L., Pasquaré, G., Venegas-Salgado, S., and Romero-Rios, F. (2000). Geology of the western mexican volcanic belt and adjacent sierra madre occidental and jalisco block. *Geological Society of America Special Papers*, 334:65–83.

Ferrari, L., Petrone, C. M., and Francalanci, L. (2001). Generation of oceanic-island basalt–type volcanism in the western trans-mexican volcanic belt by slab rollback, asthenosphere infiltration, and variable flux melting. *Geology*, 29(6):507–510.

Ferrari, L. and Rosas-Elguera, J. (2000). Late miocene to quaternary extension at the northern boundary of the jalisco block, western mexico: The tepic-zacoalco rift revised. *Geological Society of America Special Papers*, 334:41–63.

Ferrazzini, V., Aki, K., and Chouet, B. (1991). Characteristics of seismic waves composing hawaiian volcanic tremor and gas-piston events observed by a near-source array. *Journal of Geophysical Research: Solid Earth*, 96(B4):6199–6209.

Field, E. H. and Jacob, K. H. (1995). A comparison and test of various site-response estimation techniques, including three that are not reference-site dependent. *Bulletin of the Seismological Society of America*, 85(4):1127–1143.

Fink, M. (1992). Time reversal of ultrasonic fields. i. basic principles. *Ultrasonics, Ferroelectrics and Frequency Control, IEEE Transactions on*, 39(5):555–566.

Fournier, T., Pritchard, M., and Riddick, S. (2010). Duration, magnitude, and frequency of subaerial volcano deformation events: New results from latin america using insar and a global synthesis. *Geochemistry, Geophysics, Geosystems*, 11(1).

Frey, H. M., Lange, R. A., Hall, C. M., Delgado-Granados, H., and Carmichael, I. S. E. (2007). A pliocene ignimbrite flare-up along the tepic-zacoalco rift: Evidence for the initial stages of rifting between the jalisco block (mexico) and north america. *Geological Society of America Bulletin*, 119:49–64.

Friedrich, A., Krüger, F., and Klinge, K. (1998). Ocean-generated microseismic noise located with the gräfenberg array. *Journal of Seismology*, 2(1):47–64.

Froger, J.-L., Remy, D., Bonvalot, S., and Legrand, D. (2007). Two scales of inflation at lastarria-cordon del azufre volcanic complex, central andes, revealed from ASAR-ENVISAT interferometric data. *Earth and Planetary Science Letters*, 255(1–2):148–163.

Froment, B. (2011). *Utilisation du bruit sismique ambiant dans le suivi temporel de structures géologiques*. PhD thesis, Université de Grenoble, France.

Froment, B., Campillo, M., Chen, J., and Liu, Q. (2013). Deformation at depth associated with the 12 may 2008 MW 7.9 wenchuan earthquake from seismic ambient noise monitoring. *Geophysical Research Letters*, 40(1):78–82.

Froment, B., Campillo, M., and Roux, P. (2011). Reconstructing the green's function through iteration of correlations. *Comptes Rendus Geoscience*, 343(8–9):623–632.

Froment, B., Campillo, M., Roux, P., Gouédard, P., Verdel, A., and Weaver, R. L. (2010). Estimation of the effect of nonisotropically distributed energy on the apparent arrival time in correlations. *Geophysics*, 75(5):SA85–SA93.

Gaite, B., Iglesias, A., Villaseñor, A., Herraiz, M., and Pacheco, J. F. (2012). Crustal structure of mexico and surrounding regions from seismic ambient noise tomography. *Geophysical Journal International*, 188(3):1413–1424.

García-Jerez, A., Luzón, F., Sánchez-Sesma, F. J., Lunedei, E., Albarello, D., Santoyo, M. A., and Almendros, J. (2013). Diffuse elastic wavefield within a simple crustal model. some consequences for low and high frequencies. *Journal of Geophysical Research: Solid Earth*, 118(10):5577–5595.

García-Jerez, A., Navarro, M., Alcalá, F., Luzón, F., Pérez-Ruiz, J., Enomoto, T., Vidal, F., and Ocaña, E. (2007). Shallow velocity structure using joint inversion of array and h/v spectral ratio of ambient noise: The case of mula town (se of spain). *Soil Dynamics and Earthquake Engineering*, 27(10):907–919.

Garnier, J. and Papanicolaou, G. (2009). Passive sensor imaging using cross correlations of noisy signals in a scattering medium. *SIAM Journal on Imaging Sciences*, 2(2):396–437.

Garnier, J. and Papanicolaou, G. (2010). Resolution analysis for imaging with noise. *Inverse Problems*, 26(7):074001.

Gaviria, P., Ramón, J., Gutiérrez, M., A, C., Bandy, W. L., and Michaud, F. (2013). Morphology and magnetic survey of the rivera-cocos plate boundary of colima, mexico. *Geofísica internacional*, 52(1):73–85.

G.G.L., K. (1921). Het idjen hoogland de geologie en geomorphologie van den idjen. Technical report, de Koninklijke Natuurkundige Vereniging.

Giles, P. M., Duvall, T. L., Scherrer, P. H., and Bogart, R. S. (1997). A subsurface flow of material from the sun's equator to its poles. *Nature*, 390(6655):52–54.

Godin, O. A. (2007). Emergence of the acoustic green's function from thermal noise. *The Journal of the Acoustical Society of America*, 121(2):EL96–EL102.

Godin, O. A. (2009). Accuracy of the deterministic travel time retrieval from cross-correlations of non-diffuse ambient noisea). *The Journal of the Acoustical Society of America*, 126(6):EL183–EL189.

Gómez-Tuena, A., Orozco-Esquivel, M. T., and Ferrari, L. (2007). Igneous petrogenesis of the trans-mexican volcanic belt. *Geological Society of America Special Papers*, 422:129–181.

Goodman, N. R. (1960). Measuring amplitude and phase. *Journal of the Franklin Institute*, 270(6):437–450.

Gouédard, P. (2008). *Techniques de corrélation : aspects méthodologiques et applications à la sub-surface*. PhD thesis, Université de Grenoble, France.

Gouédard, P., Stehly, L., Brenguier, F., Campillo, M., Colin de Verdière, Y., Larose, E., Margerin, L., Roux, P., Sánchez-Sesma, F. J., Shapiro, N. M., and Weaver, R. L. (2008).

Cross-correlation of random fields: mathematical approach and applications. *Geophysical Prospecting*, 56(3):375–393.

Gudmundsson, Ó., Khan, A., and Voss, P. (2007). Rayleigh-wave group-velocity of the icelandic crust from correlation of ambient seismic noise. *Geophysical Research Letters*, 34(14):n/a–n/a.

Guéguen, P., Cornou, C., Garambois, S., and Banton, J. (2007). On the limitation of the h/v spectral ratio using seismic noise as an exploration tool: Application to the grenoble valley (france), a small apex ratio basin. *Pure and Applied Geophysics*, 164(1):115–134.

Gutenberg, B. (1958). Microseisms. *Advances in Geophysics*, 5:53–92.

Hadziioannou, C. (2011). *Ondes sismiques en milieu complexe : mesure des variations temporelles des vitesses*. PhD thesis, Université de Grenoble, France.

Hadziioannou, C., Larose, E., Baig, A., Roux, P., and Campillo, M. (2011). Improving temporal resolution in ambient noise monitoring of seismic wave speed. *Journal of Geophysical Research: Solid Earth (1978–2012)*, 116(B7).

Hadziioannou, C., Larose, E., Coutant, O., Roux, P., and Campillo, M. (2009). Stability of monitoring weak changes in multiply scattering media with ambient noise correlation: Laboratory experiments. *The Journal of the Acoustical Society of America*, 125(6):3688–3695.

Handley, H. K., Macpherson, C. G., Davidson, J. P., Berlo, K., and Lowry, D. (2007). Constraining fluid and sediment contributions to subduction-related magmatism in indonesia: Ijen volcanic complex. *Journal of Petrology*, 48(6):1155–1183.

Heimann, S., Trabs, S., and Dahm, T. (2013). Lazufre volcanic complex, chile: attempts to image a large scale magmatic inflation body using regional and teleseismic broadband recordings. In *EGU General Assembly Conference Abstracts*, volume 15, page 13072.

Henderson, S. T. and Pritchard, M. E. (2013). Decadal volcanic deformation in the central andes volcanic zone revealed by InSAR time series. *Geochemistry, Geophysics, Geosystems*, 14(5):1358–1374.

Hennino, R., Trégoures, N., Shapiro, N., Margerin, L., Campillo, M., Van Tiggelen, B., and Weaver, R. (2001). Observation of equipartition of seismic waves. *Physical Review Letters*, 86(15):3447.

Herak, M. (2008). ModelHVSR—a matlab® tool to model horizontal-to-vertical spectral ratio of ambient noise. *Computers & Geosciences*, 34(11):1514–1526.

Herrmann, R. B. (1996). Computer proramms in seismology.

Hunter, J. D. (2007). Matplotlib: A 2d graphics environment. *Computing in Science and Engineering*, 9(3):90–95.

Ibs-von Seht, M. and Wohlenberg, J. (1999). Microtremor measurements used to map thickness of soft sediments. *Bulletin of the Seismological Society of America*, 89(1):250–259.

Iglesias, A., Clayton, R. W., Pérez-Campos, X., Singh, S. K., Pacheco, J. F., García, D., and Valdés-González, C. (2010). S wave velocity structure below central mexico using high-resolution surface wave tomography. *Journal of Geophysical Research: Solid Earth*, 115(B6):n/a–n/a.

Iglesias, A., Cruz-Atienza, V. M., Shapiro, N. M., Singh, S. K., and Pacheco, J. F. (2001). Crustal structure of south-central mexico estimated from the inversion of surface-wave dispersion curves using genetic and simulated annealing algorithms. *Geofísica Internacional*, 40(3).

Ingebritsen, S. and Sorey, M. (1985). A quantitative analysis of the lassen hydrothermal system, north central california. *Water Resources Research*, 21(6):853–868.

Jaxybulatov, K., Shapiro, N. M., Koulakov, I., Mordret, A., Landès, M., and Sens-Schönfelder, C. (2014). A large magmatic sill complex beneath the toba caldera. *Science*, 346(6209):617–619.

Jay, J. A., Pritchard, M. E., West, M. E., Christensen, D., Haney, M., Minaya, E., Sunagua, M., McNutt, S. R., and Zabala, M. (2012). Shallow seismicity, triggered seismicity, and ambient noise tomography at the long-dormant uturuncu volcano, bolivia. *Bulletin of volcanology*, 74(4):817–837.

Jousset, P., Haberland, C., Bauer, K., and Arnason, K. (2011). Hengill geothermal volcanic complex (iceland) characterized by integrated geophysical observations. *Geothermics*, 40(1):1–24.

Jousset, P., Neuberg, J., and Jolly, A. (2004). Modelling low-frequency volcanic earthquakes in a viscoelastic medium with topography. *Geophysical Journal International*, 159(2):776–802.

Jousset, P., Neuberg, J., and Sturton, S. (2003). Modelling the time-dependent frequency content of low-frequency volcanic earthquakes. *Journal of Volcanology and Geothermal Research*, 128(1):201–223.

Kang, T.-S. and Shin, J. S. (2006). Surface-wave tomography from ambient seismic noise of accelerograph networks in southern korea. *Geophysical Research Letters*, 33(17):L17303.

Kárason, H. and Van Der Hilst, R. D. (2000). Constraints on mantle convection from seismic tomography. In Richards, r. A., Gordon, R. G., and Hilst, R. D. V. D., editors, *The History and Dynamics of Global Plate Motions*, pages 277–288. American Geophysical Union.

Karplus, M., Klemperer, S., Lawrence, J., Zhao, W., Mechie, J., Tilmann, F., Sandvol, E., and Ni, J. (2013). Ambient-noise tomography of north tibet limits geological terrane signature to upper-middle crust. *Geophysical Research Letters*, 40(5):808–813.

Kawase, H., Sánchez-Sesma, F. J., and Matsushima, S. (2011). The optimal use of horizontal-to-vertical spectral ratios of earthquake motions for velocity inversions based on diffuse-field theory for plane waves. *Bulletin of the Seismological Society of America*, 101(5):2001–2014.

Kim, S., Nyblade, A. A., Rhie, J., Baag, C.-E., and Kang, T.-S. (2012). Crustal s-wave velocity structure of the main ethiopian rift from ambient noise tomography. *Geophysical Journal International*, 191(2):865–878.

Kinnaert, X., Calo, M., and Dorbath, C. (2012). 3-d surface wave tomography of the soultz-sous-forêts enhanced geothermal site using seismic noise correlations. In *AGU Fall Meeting Abstracts*, volume 1, page 2497.

Kirkpatrick, S. (1984). Optimization by simulated annealing: Quantitative studies. *Journal of statistical physics*, 34(5-6):975–986.

Konno, K. and Ohmachi, T. (1998). Ground-motion characteristics estimated from spectral ratio between horizontal and vertical components of microtremor. *Bulletin of the Seismological Society of America*, 88(1):228–241.

Kostoglodov, V. and Bandy, W. (1995). Seismotectonic constraints on the convergence rate between the rivera and north american plates. *Journal of Geophysical Research: Solid Earth (1978–2012)*, 100(B9):17977–17989.

Krischer, L., Megies, T., Barsch, R., Beyreuther, M., Lecocq, T., Caudron, C., and Wassermann, J. (2015). Obspy: a bridge for seismology into the scientific python ecosystem. *Computational Science & Discovery*, 8(1):014003.

Kubo, R. (1966). The fluctuation-dissipation theorem. *Reports on Progress in Physics*, 29(1):255.

Kuznetsov, P. and Koulakov, I. Y. (2014). The three-dimensional structure beneath the popocatépetl volcano (mexico) based on local earthquake seismic tomography. *Journal of Volcanology and Geothermal Research*, 276:10–21.

Lachetl, C. and Bard, P.-Y. (1994). Numerical and theoretical investigations on the possibilities and limitations of nakamura's technique. *Journal of Physics of the Earth*, 42(5):377–397.

Lacoss, R., Kelly, E., and Toksöz, M. (1969). Estimation of seismic noise structure using arrays. *GEOPHYSICS*, 34(1):21–38.

Landès, M., Hubans, F., Shapiro, N. M., Paul, A., and Campillo, M. (2010). Origin of deep ocean microseisms by using teleseismic body waves. *Journal of Geophysical Research: Solid Earth*, 115(B5):B05302.

Larose, E., Khan, A., Nakamura, Y., and Campillo, M. (2005). Lunar subsurface investigated from correlation of seismic noise. *Geophysical Research Letters*, 32(16).

Larose, E., Roux, P., and Campillo, M. (2007). Reconstruction of rayleigh–lamb dispersion spectrum based on noise obtained from an air-jet forcing. *The Journal of the Acoustical Society of America*, 122(6):3437–3444.

Lawrence, J. F., Denolle, M., Seats, K. J., and Prieto, G. A. (2013). A numeric evaluation of attenuation from ambient noise correlation functions. *Journal of Geophysical Research: Solid Earth*, 118(12):6134–6145.

Lawrence, J. F. and Prieto, G. A. (2011). Attenuation tomography of the western united states from ambient seismic noise. *J. Geophys. Res*, 116:B06302.

Lecocq, T., Caudron, C., and Brenguier, F. (2014). MSNoise, a python package for monitoring seismic velocity changes using ambient seismic noise. *Seismological Research Letters*, 85(3):715–726.

Lees, J. M. (2007). Seismic tomography of magmatic systems. *Journal of Volcanology and Geothermal Research*, 167(1–4):37–56.

Legrand, D., Calahorrano, A., Guillier, B., Rivera, L., Ruiz, M., Villagómez, D., and Yepes, H. (2002). Stress tensor analysis of the 1998–1999 tectonic swarm of northern quito related to the volcanic swarm of guagua pichincha volcano, ecuador. *Tectonophysics*, 344(1–2):15–36.

Lehujeur, M., Vergne, J., Maggi, A., and Schmittbuhl, J. (2013). Imaging of a deep geothermal reservoir using ambient noise correlation. In *European Geothermal Congress*.

Lehujeur, M., Vergne, J., Schmittbuhl, J., and Maggi, A. (2015). Characterization of ambient seismic noise near a deep geothermal reservoir and implications for interferometric methods: a case study in northern alsace, france. *Geothermal Energy*, 3(1):1–17.

Lermo, J. and Chávez-García, F. J. (1993). Site effect evaluation using spectral ratios with only one station. *Bulletin of the Seismological Society of America*, 83(5):1574–1594.

Lesage, P., Reyes-Dávila, G., and Arámbula-Mendoza, R. (2014). Large tectonic earthquakes induce sharp temporary decreases in seismic velocity in volcán de colima, mexico. *Journal of Geophysical Research: Solid Earth*.

Lévěque, J.-J., Rivera, L., and Wittlinger, G. (1993). On the use of the checker-board test to assess the resolution of tomographic inversions. *Geophysical Journal International*, 115(1):313–318.

Levshin, A. L., Pisarenko, V. F., and Pogrebinsky, G. A. (1972). Frequency-time analysis of oscillations. *ANNALES DE GEOPHYSIQUE*, 28(2):211–218.

Levshin, A. L., Yanovskaia, T. B., Lander, A. V., Bukchin, B. G., Barmin, M. P., Ratnikova, L. I., and Its, E. N. (1989). Surface waves in vertically inhomogeneous media. *Seismic Surface Waves in a Laterally Inhomogeneous Earth*, pages 131–182.

Lin, F.-C., Moschetti, M. P., and Ritzwoller, M. H. (2008). Surface wave tomography of the western united states from ambient seismic noise: Rayleigh and love wave phase velocity maps. *Geophysical Journal International*, 173(1):281–298.

Lin, F.-C. and Ritzwoller, M. H. (2011). Helmholtz surface wave tomography for isotropic and azimuthally anisotropic structure. *Geophysical Journal International*, 186(3):1104–1120.

Lin, F.-C., Ritzwoller, M. H., and Snieder, R. (2009). Eikonal tomography: surface wave tomography by phase front tracking across a regional broad-band seismic array. *Geophysical Journal International*, 177(3):1091–1110.

Lin, F.-C., Ritzwoller, M. H., Townend, J., Bannister, S., and Savage, M. K. (2007). Ambient noise rayleigh wave tomography of new zealand. *Geophysical Journal International*, 170(2):649–666.

Lin, F.-C., Tsai, V. C., and Ritzwoller, M. H. (2012). The local amplification of surface waves: A new observable to constrain elastic velocities, density, and anelastic attenuation. *Journal of Geophysical Research: Solid Earth (1978–2012)*, 117(B6).

Liu, Z., Huang, J., Peng, Z., and Su, J. (2014). Seismic velocity changes in the epicentral region of the 2008 wenchuan earthquake measured from three-component ambient noise correlation techniques. *Geophysical Research Letters*, 41(1):37–42.

Lobkis, O. I. and Weaver, R. L. (2001). On the emergence of the green's function in the correlations of a diffuse field. *The Journal of the Acoustical Society of America*, 110(6):3011–3017.

Longuet-Higgins, M. S. (1950). A theory of the origin of microseisms. *Philosophical Transactions of the Royal Society of London A: Mathematical, Physical and Engineering Sciences*, 243(857):1–35.

López-Loera, H. (2012). 2 ³⁄₄ dimension modeling of the aeromagnetic anomaly of volcán de colima, western mexico. *Geofísica internacional*, 51(2):129–142.

Lu, Z., Dzurisin, D., Biggs, J., Wicks, C., and McNutt, S. (2010). Ground surface deformation patterns, magma supply, and magma storage at okmok volcano, alaska, from insar analysis: 1. intereruption deformation, 1997–2008. *Journal of Geophysical Research: Solid Earth (1978–2012)*, 115(B5).

Luhr, J. F. (1992). Slab-derived fluids and partial melting in subduction zones: insights from two contrasting mexican volcanoes (colima and ceboruco). *Journal of Volcanology and Geothermal Research*, 54(1–2):1–18.

Luhr, J. F. and Carmichael, I. S. E. (1980). The colima volcanic complex, mexico. *Contributions to Mineralogy and Petrology*, 71(4):343–372.

Luo, Y., Yang, Y., Xu, Y., Xu, H., Zhao, K., and Wang, K. (2015). On the limitations of interstation distances in ambient noise tomography. *Geophysical Journal International*, 201(2):652–661.

Lüschen, E., Müller, C., Kopp, H., Engels, M., Lutz, R., Planert, L., Shulgin, A., and Djajadihardja, Y. S. (2011). Structure, evolution and tectonic activity of the eastern sunda forearc, indonesia, from marine seismic investigations. *Tectonophysics*, 508(1–4):6–21.

Ma, S. and Beroza, G. C. (2012). Ambient-field green's functions from asynchronous seismic observations. *Geophysical Research Letters*, 39(6).

Mainsant, G., Larose, E., Brönnimann, C., Jongmans, D., Michoud, C., and Jaboyedoff, M. (2012). Ambient seismic noise monitoring of a clay landslide: Toward failure prediction. *Journal of Geophysical Research: Earth Surface (2003–2012)*, 117(F1).

Malischewsky, P. G. and Scherbaum, F. (2004). Love's formula and h/v-ratio (ellipticity) of rayleigh waves. *Wave Motion*, 40(1):57–67.

Manea, V., Manea, M., Kostoglodov, V., and Sewell, G. (2006). Intraslab seismicity and thermal stress in the subducted cocos plate beneath central mexico. *Tectonophysics*, 420(3):389–408.

Margerin, L., Campillo, M., Shapiro, N., and Van Tiggelen, B. (1999). Residence time of diffuse waves in the crust as a physical interpretation of coda q: application to seismograms recorded in mexico. *Geophysical Journal International*, 138(2):343–352.

Margerin, L., Campillo, M., and Van Tiggelen, B. (2000). Monte carlo simulation of multiple scattering of elastic waves. *Journal of Geophysical Research: Solid Earth (1978–2012)*, 105(B4):7873–7892.

Marsh, B. D. (2000). Magma chambers. *Encyclopedia of volcanoes*, 1:191–206.

Masterlark, T., Haney, M., Dickinson, H., Fournier, T., and Searcy, C. (2010). Rheologic and structural controls on the deformation of okmok volcano, alaska: FEMs, InSAR, and ambient noise tomography. *Journal of Geophysical Research: Solid Earth*, 115(B2):B02409.

Matsushima, S., Hirokawa, T., Martin, F. D., Kawase, H., and Sánchez-Sesma, F. J. (2014). The effect of lateral heterogeneity on horizontal to vertical spectral ratio of microtremors inferred from observation and synthetics. *Bulletin of the Seismological Society of America*, 104(1):381–393.

Medina-Martínez, F., Espíndola, J. M., De la Fuente, M., and Mena, M. (1996). A gravity model of the colima. *Geofísica Internacional*, 35:409–114.

Menke, W. (2012). *Geophysical Data Analysis: Discrete Inverse Theory*. Academic Press.

Minato, S., Tsuji, T., Ohmi, S., and Matsuoka, T. (2012). Monitoring seismic velocity change caused by the 2011 tohoku-oki earthquake using ambient noise records. *Geophysical Research Letters*, 39(9).

Mora, M. M., Lesage, P., Dorel, J., Bard, P.-Y., Métaxian, J.-P., Alvarado, G. E., and Leandro, C. (2001). Study of seismic site effects using h/v spectral ratios at arenal volcano, costa rica. *Geophysical Research Letters*, 28(15):2991–2994.

Mora, M. M., Lesage, P., Valette, B., Alvarado, G. E., Leandro, C., Métaxian, J.-P., and Dorel, J. (2006). Shallow velocity structure and seismic site effects at arenal volcano, costa rica. *Journal of Volcanology and Geothermal Research*, 152(1–2):121–139.

Mordret, A. (2014). *Imaging and monitoring using correlations of seismic noise in an industrial context: application to the Valhall network*. PhD thesis, Institut de Physique du Globe de Paris, France.

Mordret, A., Jolly, A., Duputel, Z., and Fournier, N. (2010). Monitoring of phreatic eruptions using interferometry on retrieved cross-correlation function from ambient seismic noise: Results from mt. ruapehu, new zealand. *Journal of Volcanology and Geothermal Research*, 191(1–2):46–59.

Mordret, A., Landès, M., Shapiro, N. M., Singh, S. C., Roux, P., and Barkved, O. I. (2013a). Near-surface study at the valhall oil field from ambient noise surface wave tomography. *Geophysical Journal International*, page ggt061.

Mordret, A., Rivet, D., Landès, M., and Shapiro, N. M. (2014a). 3-d shear-velocity anisotropic model of piton de la fournaise volcano (la réunion island) from ambient seismic noise. *Journal of Geophysical Research: Solid Earth*, page 2014JB011654.

Mordret, A., Shapiro, N. M., and Singh, S. (2014b). Seismic noise-based time-lapse monitoring of the valhall overburden. *Geophysical Research Letters*, 41(14):4945–4952.

Mordret, A., Shapiro, N. M., Singh, S. S., Roux, P., and Barkved, O. I. (2013b). Helmholtz tomography of ambient noise surface wave data to estimate scholte wave phase velocity at valhall life of the field. *GEOPHYSICS*, 78(2):WA99–WA109.

Moschetti, M. P., Ritzwoller, M. H., Lin, F.-C., and Yang, Y. (2010). Crustal shear wave velocity structure of the western united states inferred from ambient seismic noise and earthquake data. *Journal of Geophysical Research: Solid Earth*, 115(B10):B10306.

Mucciarelli, M. (1998). Reliability and applicability of nakamura's technique using microtremors: An experimental approach. *Journal of Earthquake Engineering*, 2(4):625–638.

Nagaoka, Y., Nishida, K., Aoki, Y., Takeo, M., and Ohminato, T. (2012). Seismic imaging of magma chamber beneath an active volcano. *Earth and Planetary Science Letters*, 333–334:1–8.

Nakahara, H. (2006). Theoretical background of retrieving green's function by cross-correlation: one-dimensional case. *Geophysical Journal International*, 165:719–728.

Nakamura, Y. (1989). A method for dynamic characteristics estimation of subsurface using microtremor on the ground surface. *Railway Technical Research Institute, Quarterly Reports*, 30(1).

Nakamura, Y. (2000). Clear identification of fundamental idea of nakamura's technique and its applications. In *Proceedings of the 12th world conference on earthquake engineering.*, New Zealand: Auckland.

Naranjo, J. A. (1985). Sulphur flows at lastarria volcano in the north chilean andes. *Nature*, 313(6005):778–780.

Nardone, L. and Maresca, R. (2011). Shallow velocity structure and site effects at mt. vesuvius, italy, from HVSR and array measurements of ambient vibrations. *Bulletin of the Seismological Society of America*, 101(4):1465–1477.

Nicolson, H., Curtis, A., Baptie, B., and Galetti, E. (2012). Seismic interferometry and ambient noise tomography in the british isles. *Proceedings of the Geologists' Association*, 123(1):74–86.

Nishida, K., Kawakatsu, H., and Obara, K. (2008). Three-dimensional crustal s wave velocity structure in japan using microseismic data recorded by hi-net tiltmeters. *Journal of Geophysical Research: Solid Earth (1978–2012)*, 113(B10).

Nishida, K., Montagner, J.-P., and Kawakatsu, H. (2009). Global surface wave tomography using seismic hum. *Science*, 326(5949):112–112.

O'Brien, G. S. and Bean, C. J. (2009). Volcano topography, structure and intrinsic attenuation: Their relative influences on a simulated 3d visco-elastic wavefield. *Journal of Volcanology and Geothermal Research*, 183(1–2):122–136.

Panzera, F., Lombardo, G., and Rigano, R. (2011). Evidence of topographic effects through the analysis of ambient noise measurements. *Seismological Research Letters*, 82(3):413–419.

Pardo, M. and Suárez, G. (1995). Shape of the subducted rivera and cocos plates in southern mexico: Seismic and tectonic implications. *Journal of Geophysical Research: Solid Earth*, 100(B7):12357–12373.

Parolai, S., Bormann, P., and Milkereit, C. (2002). New relationships between vs, thickness of sediments, and resonance frequency calculated by the h/v ratio of seismic noise for the cologne area (germany). *Bulletin of the Seismological Society of America*, 92(6):2521–2527.

Parsiegla, N. and Wegler, U. (2008). Modelling of seismic energy transport at volcanoes with real topography and complex propagation medium. *Journal of Volcanology and Geothermal Research*, 171(3–4):229–236.

Paul, A., Campillo, M., Margerin, L., Larose, E., and Derode, A. (2005). Empirical synthesis of time-asymmetrical green functions from the correlation of coda waves. *Journal of Geophysical Research: Solid Earth (1978–2012)*, 110(B8).

Pearse, J. and Lundgren, P. (2013). Source model of deformation at lazufre volcanic center, central andes, constrained by InSAR time series. *Geophysical Research Letters*, 40(6):1059–1064.

Pérez-Campos, X., Kim, Y., Husker, A., Davis, P. M., Clayton, R. W., Iglesias, A., Pacheco, J. F., Singh, S. K., Manea, V. C., and Gurnis, M. (2008). Horizontal subduction and

truncation of the cocos plate beneath central mexico. *Geophysical Research Letters*, 35(18):L18303.

Perrier, L. (2011). *Apport de l'étude des sources sismo-volcaniques à la connaissance des processus éruptifs du volcan Yasur Vanuatu*. PhD thesis, Université de Grenoble, France.

Perrier, L., Métaxian, J.-P., Battaglia, J., and Garaebiti, E. (2012). Estimation of the near-surface velocity structure of the yasur-yenkahe volcanic complex, vanuatu. *Journal of Volcanology and Geothermal Research*, 227–228:50–60.

Perton, M., Sánchez-Sesma, F. J., Rodríguez-Castellanos, A., Campillo, M., and Weaver, R. L. (2009). Two perspectives on equipartition in diffuse elastic fields in three dimensions. *The Journal of the Acoustical Society of America*, 126(3):1125–1130.

Petrosino, S., Damiano, N., Cusano, P., Di Vito, M. A., de Vita, S., and Del Pezzo, E. (2012). Subsurface structure of the solfatara volcano (campi flegrei caldera, italy) as deduced from joint seismic-noise array, volcanological and morphostructural analysis. *Geochemistry, Geophysics, Geosystems*, 13(7):Q07006.

Piña-Flores, J. (2015). *Cálculo e Inversión del Cociente H/V a Partir de Ruido Ambiental*. MSc thesis, Universidad Nacional Autónoma de México, Mexico city.

Piña-Flores, J., García-Jerez, A., Luzón, F., Perton, M., and Sánchez-Sesma, F. J. (2014). Inversion of h/v ratio in layered systems. In ., San Francisco, CA. AGU.

Poli, P., Campillo, M., Pedersen, H., et al. (2012a). Body-wave imaging of earth's mantle discontinuities from ambient seismic noise. *Science*, 338(6110):1063–1065.

Poli, P., Pedersen, H., and Campillo, M. (2012b). Emergence of body waves from cross-correlation of short period seismic noise. *Geophysical Journal International*, 188(2):549–558.

Prieto, G., Lawrence, J., and Beroza, G. (2009). Anelastic earth structure from the coherency of the ambient seismic field. *J. geophys. Res*, 114:B07303.

Prieto, G. A. (2012). Imaging the deep earth. *Science*, 338(6110):1037–1038.

Prieto, G. A. and Beroza, G. C. (2008). Earthquake ground motion prediction using the ambient seismic field. *Geophys. Res. Lett*, 35:L14304.

Prieto, G. A., Denolle, M., Lawrence, J. F., and Beroza, G. C. (2011). On amplitude information carried by the ambient seismic field. *Comptes Rendus Geoscience*, 343(8):600–614.

Prieto, G. A., Lawrence, J. F., Chung, A. I., and Kohler, M. D. (2010). Impulse response of civil structures from ambient noise analysis. *Bulletin of the Seismological Society of America*, 100(5A):2322.

Pritchard, M. E. and Simons, M. (2002). A satellite geodetic survey of large-scale deformation of volcanic centres in the central andes. *Nature*, 418(6894):167–171.

Pritchard, M. E. and Simons, M. (2004). An InSAR-based survey of volcanic deformation in the southern andes. *Geophysical Research Letters*, 31(15):L15610.

Prôno, E., Battaglia, J., Monteiller, V., Got, J.-L., and Ferrazzini, V. (2009). P-wave velocity structure of piton de la fournaise volcano deduced from seismic data recorded between 1996 and 1999. *Journal of Volcanology and Geothermal Research*, 184(1):49–62.

Pyle, M. L., Wiens, D. A., Nyblade, A. A., and Anandakrishnan, S. (2010). Crustal structure of the transantarctic mountains near the ross sea from ambient seismic noise tomography. *Journal of Geophysical Research: Solid Earth (1978–2012)*, 115(B11).

Rawlinson, N., Hauser, J., and Sambridge, M. (2008). Seismic ray tracing and wavefront tracking in laterally heterogeneous media. *Advances in Geophysics*, 49:203–273.

Rawlinson, N. and Sambridge, M. (2003). Seismic traveltime tomography of the crust and lithosphere. In *Advances in Geophysics*, volume Volume 46, pages 81–198. Elsevier.

Rawlinson, N. and Sambridge, M. (2004a). Multiple reflection and transmission phases in complex layered media using a multistage fast marching method. *GEOPHYSICS*, 69(5):1338–1350.

Rawlinson, N. and Sambridge, M. (2004b). Wave front evolution in strongly heterogeneous layered media using the fast marching method. *Geophysical Journal International*, 156(3):631–647.

Rawlinson, N. and Sambridge, M. (2005). The fast marching method: an effective tool for tomographic imaging and tracking multiple phases in complex layered media. *Exploration Geophysics*, 36(4):341–350.

Remy, D., Froger, J. L., Perfettini, H., Bonvalot, S., Gabalda, G., Albino, F., Cayol, V., Legrand, D., and Saint Blanquat, M. D. (2014). Persistent uplift of the lazufre volcanic complex (central andes): New insights from PCAIM inversion of InSAR time series and GPS data. *Geochemistry, Geophysics, Geosystems.*

Ritzwoller, M. H., Lin, F.-C., and Shen, W. (2011). Ambient noise tomography with a large seismic array. *Comptes Rendus Geoscience*, 343(8):558–570.

Rivet, D., Brenguier, F., Clarke, D., Shapiro, N. M., and Peltier, A. (2014a). Long-term dynamics of piton de la fournaise volcano from 13 years of seismic velocity change measurements and gps observations. *Journal of Geophysical Research: Solid Earth*, 119(10):7654–7666.

Rivet, D., Campillo, M., Radiguet, M., Zigone, D., Cruz-Atienza, V., Shapiro, N. M., Kostoglodov, V., Cotte, N., Cougoulat, G., Walpersdorf, A., et al. (2014b). Seismic velocity changes, strain rate and non-volcanic tremors during the 2009–2010 slow slip event in guerrero, mexico. *Geophysical Journal International*, 196(1):447–460.

Rivet, D., Campillo, M., Shapiro, N. M., Cruz-Atienza, V., Radiguet, M., Cotte, N., and Kostoglodov, V. (2011). Seismic evidence of nonlinear crustal deformation during a large slow slip event in mexico. *Geophysical Research Letters*, 38(8):n/a–n/a.

Rosas-Elguera, J., Ferrari, L., Garduño-Monroy, V. H., and Urrutia-Fucugauchi, J. (1996). Continental boundaries of the jalisco block and their influence in the pliocene-quaternary kinematics of western mexico. *Geology*, 24(10):921–924.

Roux, P. (2009). Passive seismic imaging with directive ambient noise: application to surface waves and the san andreas fault in parkfield, ca. *Geophysical Journal International*, 179(1):367–373.

Roux, P., Sabra, K. G., Gerstoft, P., Kuperman, W. A., and Fehler, M. C. (2005a). P-waves from cross-correlation of seismic noise. *Geophysical Research Letters*, 32(19):L19303.

Roux, P., Sabra, K. G., Kuperman, W. A., and Roux, A. (2005b). Ambient noise cross correlation in free space: Theoretical approach. *The Journal of the Acoustical Society of America*, 117(1):79–84.

Ruch, J., Anderssohn, J., Walter, T. R., and Motagh, M. (2008). Caldera-scale inflation of the lazufre volcanic area, south america: Evidence from InSAR. *Journal of Volcanology and Geothermal Research*, 174(4):337–344.

Ruch, J., Manconi, A., Zeni, G., Solaro, G., Pepe, A., Shirzaei, M., Walter, T. R., and Lanari, R. (2009). Stress transfer in the lazufre volcanic area, central andes. *Geophysical Research Letters*, 36(22):L22303.

Ruch, J. and Walter, T. (2010). Relationship between the insar-measured uplift, the structural framework, and the present-day stress field at lazufre volcanic area, central andes. *Tectonophysics*, 492(1):133–140.

Ruigrok, E., Campman, X., and Wapenaar, K. (2011). Extraction of p-wave reflections from microseisms. *Comptes Rendus Geoscience*, 343(8–9):512–525.

Ryzhik, L., Papanicolaou, G., and Keller, J. B. (1996). Transport equations for elastic and other waves in random media. *Wave motion*, 24(4):327–370.

Sabra, K. G., Gerstoft, P., Roux, P., Kuperman, W. A., and Fehler, M. C. (2005a). Extracting time-domain green's function estimates from ambient seismic noise. *Geophysical Research Letters*, 32(3):L03310.

Sabra, K. G., Gerstoft, P., Roux, P., Kuperman, W. A., and Fehler, M. C. (2005b). Surface wave tomography from microseisms in southern california. *Geophysical Research Letters*, 32(14):L14311.

Sánchez-Sesma, F. J. and Campillo, M. (2006). Retrieval of the green's function from cross correlation: The canonical elastic problem. *Bulletin of the Seismological Society of America*, 96(3):1182–1191.

Sánchez-Sesma, F. J., Pérez-Ruiz, J. A., Campillo, M., and Luzón, F. (2006). Elastodynamic 2d green function retrieval from cross-correlation: Canonical inclusion problem. *Geophysical Research Letters*, 33(13).

Sánchez-Sesma, F. J., Pérez-Ruiz, J. A., Luzón, F., Campillo, M., and Rodríguez-Castellanos, A. (2008). Diffuse fields in dynamic elasticity. *Wave Motion*, 45(5):641–654.

Sánchez-Sesma, F. J., Rodríguez, M., Iturrarán-Viveros, U., Luzón, F., Campillo, M., Margerin, L., García-Jerez, A., Suarez, M., Santoyo, M. A., and Rodríguez-Castellanos,

A. (2011). A theory for microtremor h/v spectral ratio: application for a layered medium. *Geophysical Journal International*, 186(1):221–225.

Saygin, E. and Kennett, B. L. N. (2010). Ambient seismic noise tomography of australian continent. *Tectonophysics*, 481(1–4):116–125.

Schaaf, P., Morán-Zenteno, D., Hernández-Bernal, M. d. S., Solís-Pichardo, G., Tolson, G., and Köhler, H. (1995). Paleogene continental margin truncation in southwestern mexico: Geochronological evidence. *Tectonics*, 14(6):1339–1350.

Scher, S. (2012). *Fumarolic Activity, Acid-Sulfate Alteration and High-Sulfidation Epithermal Precious Metal ineralization in the Crater of Kawah Ijen Volcano (Java, Indonesia)*. Master's thesis, McGill University.

Scher, S., Williams-Jones, A. E., and Williams-Jones, G. (2013). Fumarolic activity, acid-sulfate alteration, and high sulfidation epithermal precious metal mineralization in the crater of kawah ijen volcano, java, indonesia. *Economic Geology*, 108(5):1099–1118.

Schimmel, M., Stutzmann, E., and Gallart, J. (2011). Using instantaneous phase coherence for signal extraction from ambient noise data at a local to a global scale. *Geophysical Journal International*, 184(1):494–506.

Seats, K. J., Lawrence, J. F., and Prieto, G. A. (2012). Improved ambient noise correlation functions using welch's method. *Geophysical Journal International*, 188(2):513–523.

Sens-Schönfelder, C. and Wegler, U. (2006). Passive image interferometry and seasonal variations of seismic velocities at merapi volcano, indonesia. *Geophysical Research Letters*, 33(21).

Serrato-Díaz, G. S., Bandy, W. L., and Gutiérrez, C. A. M. (2004). Active rifting and crustal thinning along the rivera-cocos plate boundary as inferred from mantle bouguer gravity anomalies. *Geofísica Internacional*, 43(3):361.

Sethian, J. A. (1996). A fast marching level set method for monotonically advancing fronts. *Proceedings of the National Academy of Sciences*, 93(4):1591–1595.

Shapiro, N., Campillo, M., Margerin, L., Singh, S., Kostoglodov, V., and Pacheco, J. (2000). The energy partitioning and the diffusive character of the seismic coda. *Bulletin of the Seismological Society of America*, 90(3):655–665.

Shapiro, N. M. and Campillo, M. (2004). Emergence of broadband rayleigh waves from correlations of the ambient seismic noise. *Geophysical Research Letters*, 31(7).

Shapiro, N. M., Campillo, M., Paul, A., Singh, S. K., Jongmans, D., and Sánchez-Sesma, F. J. (1997). Surface-wave propagation across the mexican volcanic belt and the origin of the long-period seismic-wave amplification in the valley of mexico. *Geophysical Journal International*, 128(1):151–166.

Shapiro, N. M., Campillo, M., Stehly, L., and Ritzwoller, M. H. (2005). High-resolution surface-wave tomography from ambient seismic noise. *Science*, 307(5715):1615–1618.

Shapiro, N. M., Ritzwoller, M., and Bensen, G. (2006). Source location of the 26 sec microseism from cross-correlations of ambient seismic noise. *Geophysical research letters*, 33(18).

Shapiro, N. M. and Singh, S. K. (1999). A systematic error in estimating surface-wave group-velocity dispersion curves and a procedure for its correction. *Bulletin of the Seismological Society of America*, 89(4):1138–1142.

Shen, Y., Ren, Y., Gao, H., and Savage, B. (2012). An improved method to extract very-broadband empirical green's functions from ambient seismic noise. *Bulletin of the Seismological Society of America*, 102(4):1872–1877.

Sitorus, K. (1990). *Volcanic stratigraphy and geochemistry of the Idjen Caldera Complex, East-Java, Indonesia*. Ph.d. thesis, Victoria University of Wellington.

Skinner, S. M. and Clayton, R. W. (2011). An evaluation of proposed mechanisms of slab flattening in central mexico. *Pure and applied geophysics*, 168(8-9):1461–1474.

Smyth, H. R., Hamilton, P. J., Hall, R., and Kinny, P. D. (2007). The deep crust beneath island arcs: Inherited zircons reveal a gondwana continental fragment beneath east java, indonesia. *Earth and Planetary Science Letters*, 258(1–2):269–282.

Snieder, R. (2002). Coda wave interferometry and the equilibration of energy in elastic media. *Physical review E*, 66(4):046615.

Snieder, R. (2004). Extracting the green's function from the correlation of coda waves: A derivation based on stationary phase. *Physical Review E*, 69(4):046610.

Snieder, R. (2006). The theory of coda wave interferometry. *Pure and Applied Geophysics*, 163(2-3):455–473.

Snieder, R. and Larose, E. (2013). Extracting earth's elastic wave response from noise measurements. *Annual Review of Earth and Planetary Sciences*, 41(1):183.

Soto, G. L., Ni, J. F., Grand, S. P., Sandvol, E., Valenzuela, R. W., Speziale, M. G., González, J. M. G., and Reyes, T. D. (2009). Mantle flow in the rivera–cocos subduction zone. *Geophysical Journal International*, 179(2):1004–1012.

Spica, Z. (2011). *Étude du volcan Kawah Ijen par la méthode des rapports spectraux H/V*. Unpublished MSc. thesis, Université Libre de Bruxelles, Brussels, Belgium.

Spica, Z., Cruz-Atienza, V. M., Reyes-Alfaro, G., Legrand, D., and Iglesias, A. (2014). Crustal imaging of western michoacán and the jalisco block, mexico, from ambient seismic noise. *Journal of Volcanology and Geothermal Research*, 289:193–201.

Spica, Z., Legrand, D., Iglesias, A., Walter, T. R., Sebastian, H., Dahm, T., Froger, J.-L., Rémy, D., Bonvalot, S., and Pardo, M. (2015). Hydrothermal and magmatic reservoirs at lazufre volcanic area, revealed by a high-resolution seismic noise tomography. *Earth and Planetary Science Letters*, 421:27–38.

Stachnik, J. and Dueker, K. (2006). Constraining yellowstone magmatic processes beneath the eastern snake river plain from rayleigh wave ambient noise. In *AGU Fall Meeting Abstracts*, volume 1, page 1375.

Stachnik, J. C., Dueker, K., Schutt, D. L., and Yuan, H. (2008). Imaging yellowstone plume-lithosphere interactions from inversion of ballistic and diffusive rayleigh wave dispersion and crustal thickness data. *Geochemistry, Geophysics, Geosystems*, 9(6):Q06004.

Stähler, S. C., Sens-Schönfelder, C., and Niederleithinger, E. (2011). Monitoring stress changes in a concrete bridge with coda wave interferometry. *The Journal of the Acoustical Society of America*, 129(4):1945–1952.

Stankiewicz, J., Ryberg, T., Haberland, C., Natawidjaja, D., et al. (2010). Lake toba volcano magma chamber imaged by ambient seismic noise tomography. *Geophysical Research Letters*, 37(17).

Stankiewicz, J., Weber, M. H., Mohsen, A., and Hofstetter, R. (2012). Dead sea basin imaged by ambient seismic noise tomography. *Pure and Applied Geophysics*, 169(4):615–623.

Stehly, L., Campillo, M., Froment, B., and Weaver, R. L. (2008). Reconstructing green's function by correlation of the coda of the correlation (c3) of ambient seismic noise. *Journal of Geophysical Research: Solid Earth*, 113(B11):B11306.

Stehly, L., Campillo, M., and Shapiro, N. (2007). Traveltime measurements from noise correlation: stability and detection of instrumental time-shifts. *Geophysical Journal International*, 171(1):223–230.

Stehly, L., Campillo, M., and Shapiro, N. M. (2006). A study of the seismic noise from its long-range correlation properties. *Journal of Geophysical Research: Solid Earth*, 111(B10):n/a–n/a.

Stehly, L., Cupillard, P., and Romanowicz, B. (2011). Towards improving ambient noise tomography using simultaneously curvelet denoising filters and SEM simulations of seismic ambient noise. *Comptes Rendus Geoscience*, 343(8–9):591–599.

Stehly, L., Fry, B., Campillo, M., Shapiro, N. M., Guilbert, J., Boschi, L., and Giardini, D. (2009). Tomography of the alpine region from observations of seismic ambient noise. *Geophysical Journal International*, 178(1):338–350.

Stein, S. and Wysession, M. (2009). *An introduction to seismology, earthquakes, and earth structure*. John Wiley & Sons.

Suhardja, S. K. (2013). *Mapping the Rivera and Cocos subduction zone*. Ph.d. thesis, University of Texas, Austin.

Sujanto, Sjarifudin, M., and Sitorus, K. (1988). Geological map of the ijen caldera complex, east java.

Syracuse, E. M. and Abers, G. A. (2006). Global compilation of variations in slab depth beneath arc volcanoes and implications. *Geochemistry, Geophysics, Geosystems*, 7(5):Q05017.

Takano, B., Suzuki, K., Sugimori, K., Ohba, T., Fazlullin, S. M., Bernard, A., Sumarti, S., Sukhyar, R., and Hirabayashi, M. (2004). Bathymetric and geochemical investigation

of kawah ijen crater lake, east java, indonesia. *Journal of Volcanology and Geothermal Research*, 135(4):299–329.

Tamburello, G., Hansteen, T. H., Bredemeyer, S., Aiuppa, A., and Tassi, F. (2014). Gas emissions from five volcanoes in northern chile and implications for the volatiles budget of the central volcanic zone. *Geophysical Research Letters*, 41(14):2014GL060653.

Taran, Y., Morán-Zenteno, D., Inguaggiato, S., Varley, N., and Luna-González, L. (2013). Geochemistry of thermal springs and geodynamics of the convergent mexican pacific margin. *Chemical Geology*, 339:251–262.

Tourin, A., Derode, A., and Fink, M. (2001). Sensitivity to perturbations of a time-reversed acoustic wave in a multiple scattering medium. *Physical review letters*, 87(27):274301.

Tramelli, A., Galluzzo, D., Del Pezzo, E., and Di Vito, M. A. (2010). A detailed study of the site effects in the volcanic area of campi flegrei using empirical approaches. *Geophysical Journal International*, 182(2):1073–1086.

Tsai, V. C. (2009). On establishing the accuracy of noise tomography travel-time measurements in a realistic medium. *Geophysical Journal International*, 178(3):1555–1564.

Tsai, V. C. and Moschetti, M. P. (2010). An explicit relationship between time-domain noise correlation and spatial autocorrelation (spac) results. *Geophysical Journal International*, 182(1):454–460.

Tukey, J. W. (1962). The future of data analysis. *The Annals of Mathematical Statistics*, pages 1–67.

van Hinsberg, V., Berlo, K., Sumarti, S., van Bergen, M., and Williams-Jones, A. (2010a). Extreme alteration by hyperacidic brines at kawah ijen volcano, east java, indonesia: II: Metasomatic imprint and element fluxes. *Journal of Volcanology and Geothermal Research*, 196(3–4):169–184.

van Hinsberg, V., Berlo, K., van Bergen, M., and Williams-Jones, A. (2010b). Extreme alteration by hyperacidic brines at kawah ijen volcano, east java, indonesia: I. textural and mineralogical imprint. *Journal of Volcanology and Geothermal Research*, 198(1–2):253–263.

van Tiggelen, B. A. (2003). Green function retrieval and time reversal in a disordered world. *Physical Review Letters*, 91(24):243904.

Ventura, G., Vilardo, G., Milano, G., and Pino, N. A. (1999). Relationships among crustal structure, volcanism and strike–slip tectonics in the lipari–vulcano volcanic complex (aeolian islands, southern tyrrhenian sea, italy). *Physics of the Earth and Planetary Interiors*, 116(1):31–52.

Vigouroux, N., Wallace, P. J., and Kent, A. J. R. (2008). Volatiles in high-k magmas from the western trans-mexican volcanic belt: Evidence for fluid fluxing and extreme enrichment of the mantle wedge by subduction processes. *Journal of Petrology*, 49(9):1589–1618.

Vigouroux-Caillibot, N. (2011). *Tracking the evolution of magmatic volatiles from the mantle to the atmosphere using integrative geochemical and geophysical methods*. Thesis, Dep. of Earth Sci., Simon Fraser Univ., Burnaby, BC, Canada.

Villaseñor, A., Yang, Y., Ritzwoller, M. H., and Gallart, J. (2007). Ambient noise surface wave tomography of the iberian peninsula: Implications for shallow seismic structure. *Geophysical Research Letters*, 34(11):L11304.

Walter, T. R. and Motagh, M. (2014). Deflation and inflation of a large magma body beneath uturuncu volcano, bolivia? insights from insar data, surface lineaments and stress modelling. *Geophysical Journal International*, page ggu080.

Wang, C.-Y., Chan, W. W., and Mooney, W. D. (2003). Three-dimensional velocity structure of crust and upper mantle in southwestern china and its tectonic implications. *Journal of Geophysical Research: Solid Earth (1978–2012)*, 108(B9).

Wapenaar, K. (2004). Retrieving the elastodynamic green's function of an arbitrary inhomogeneous medium by cross correlation. *Physical Review Letters*, 93(25):254301.

Wapenaar, K. (2006). Nonreciprocal green's function retrieval by cross correlation. *The Journal of the Acoustical Society of America*, 120(1):EL7–EL13.

Ward, K. M., Porter, R. C., Zandt, G., Beck, S. L., Wagner, L. S., Minaya, E., and Tavera, H. (2013). Ambient noise tomography across the central andes. *Geophysical Journal International*, page ggt166.

Ward, K. M., Zandt, G., Beck, S. L., Christensen, D. H., and McFarlin, H. (2014). Seismic imaging of the magmatic underpinnings beneath the altiplano-puna volcanic complex

from the joint inversion of surface wave dispersion and receiver functions. *Earth and Planetary Science Letters*, 404:43–53.

Weaver, R. L. (2005). Information from seismic noise. *Science*, 307(5715):1568–1569.

Weaver, R. L. (2012). On the retrieval of attenuation from the azimuthally averaged coherency of a diffuse field. *arXiv preprint arXiv:1206.6513*.

Weaver, R. L., Hadziioannou, C., Larose, E., and Campillo, M. (2011). On the precision of noise correlation interferometry. *Geophysical Journal International*, 185(3):1384–1392.

Weaver, R. L. and Lobkis, O. I. (2001). Ultrasonics without a source: Thermal fluctuation correlations at mhz frequencies. *Physical Review Letters*, 87(13):134301.

Weaver, R. L. and Lobkis, O. I. (2003). Elastic wave thermal fluctuations, ultrasonic waveforms by correlation of thermal phonons. *The Journal of the Acoustical Society of America*, 113(5):2611–2621.

Weemstra, C., Boschi, L., Goertz, A., and Artman, B. (2012). Seismic attenuation from recordings of ambient noise. *Geophysics*, 78(1):Q1–Q14.

Weemstra, C., Westra, W., Snieder, R., and Boschi, L. (2014). On estimating attenuation from the amplitude of the spectrally whitened ambient seismic field. *Geophysical Journal International*, page ggu088.

Wegler, U. (2003). Analysis of multiple scattering at vesuvius volcano, italy, using data of the TomoVes active seismic experiment. *Journal of Volcanology and Geothermal Research*, 128(1–3):45–63.

Wegler, U. and Lühr, B.-G. (2001). Scattering behaviour at merapi volcano (java) revealed from an active seismic experiment. *Geophysical Journal International*, 145(3):579–592.

Wegler, U., Nakahara, H., Sens-Schönfelder, C., Korn, M., and Shiomi, K. (2009). Sudden drop of seismic velocity after the 2004 mw 6.6 mid-niigata earthquake, japan, observed with passive image interferometry. *Journal of Geophysical Research: Solid Earth (1978–2012)*, 114(B6).

Wegler, U. and Sens-Schönfelder, C. (2007). Fault zone monitoring with passive image interferometry. *Geophysical Journal International*, 168(3):1029–1033.

Wicks, C. W., Dzurisin, D., Ingebritsen, S., Thatcher, W., Lu, Z., and Iverson, J. (2002). Magmatic activity beneath the quiescent three sisters volcanic center, central oregon cascade range, usa. *Geophysical Research Letters*, 29(7):26–1.

Woodhouse, J. (1974). Surface wave in a laterally varying layered structure. *Geophysical Journal International*, 37(3):461–490.

Yamanaka, H., Takemura, M., Ishida, H., and Niwa, M. (1994). Characteristics of long-period microtremors and their applicability in exploration of deep sedimentary layers. *Bulletin of the Seismological Society of America*, 84(6):1831–1841.

Yang, T., Grand, S. P., Wilson, D., Guzman-Speziale, M., Gomez-Gonzalez, J. M., Dominguez-Reyes, T., and Ni, J. (2009). Seismic structure beneath the rivera subduction zone from finite-frequency seismic tomography. *Journal of Geophysical Research: Solid Earth (1978–2012)*, 114(B1).

Yang, Y., Ritzwoller, M. H., and Jones, C. H. (2011). Crustal structure determined from ambient noise tomography near the magmatic centers of the coso region, southeastern california. *Geochemistry, Geophysics, Geosystems*, 12(2):Q02009.

Yang, Y., Ritzwoller, M. H., Levshin, A. L., and Shapiro, N. M. (2007). Ambient noise rayleigh wave tomography across europe. *Geophysical Journal International*, 168(1):259–274.

Yang, Y., Ritzwoller, M. H., Lin, F.-C., Moschetti, M. P., and Shapiro, N. M. (2008). Structure of the crust and uppermost mantle beneath the western united states revealed by ambient noise and earthquake tomography. *Journal of Geophysical Research: Solid Earth*, 113(B12):B12310.

Yang, Y., Zheng, Y., Chen, J., Zhou, S., Celyan, S., Sandvol, E., Tilmann, F., Priestley, K., Hearn, T. M., Ni, J. F., Brown, L. D., and Ritzwoller, M. H. (2010). Rayleigh wave phase velocity maps of tibet and the surrounding regions from ambient seismic noise tomography. *Geochemistry, Geophysics, Geosystems*, 11(8):Q08010.

Yao, H., Beghein, C., and Van Der Hilst, R. D. (2008). Surface wave array tomography in se tibet from ambient seismic noise and two-station analysis-ii. crustal and upper-mantle structure. *Geophysical Journal International*, 173(1):205–219.

Yao, H., Hilst, R. D. v. D., and Hoop, M. V. d. (2006). Surface-wave array tomography in SE tibet from ambient seismic noise and two-station analysis — i. phase velocity maps. *Geophysical Journal International*, 166(2):732–744.

Zhan, Z., Ni, S., Helmberger, D. V., and Clayton, R. W. (2010). Retrieval of moho-reflected shear wave arrivals from ambient seismic noise. *Geophysical Journal International*, 182(1):408–420.

Zhang, H. and Thurber, C. H. (2003). Double-difference tomography: The method and its application to the hayward fault, california. *Bulletin of the Seismological Society of America*, 93(5):1875–1889.

Zhang, J. and Yang, X. (2013). Extracting surface wave attenuation from seismic noise using correlation of the coda of correlation. *Journal of Geophysical Research: Solid Earth*, 118(5):2191–2205.

Zheng, S., Sun, X., Song, X., Yang, Y., and Ritzwoller, M. H. (2008). Surface wave tomography of china from ambient seismic noise correlation. *Geochemistry, Geophysics, Geosystems*, 9(5).

Zheng, Y., Shen, W., Zhou, L., Yang, Y., Xie, Z., and Ritzwoller, M. H. (2011). Crust and uppermost mantle beneath the north china craton, northeastern china, and the sea of japan from ambient noise tomography. *Journal of Geophysical Research: Solid Earth (1978–2012)*, 116(B12).

Zobin, V. M., Luhr, J. F., Taran, Y. A., Bretón, M., Cortés, A., De La Cruz-Reyna, S., Domínguez, T., Galindo, I., Gavilanes, J. C., Muníz, J., Navarro, C., Ramírez, J., Reyes, G. A., Ursúa, M., Velasco, J., Alatorre, E., and Santiago, H. (2002). Overview of the 1997–2000 activity of volcán de colima, méxico. *Journal of Volcanology and Geothermal Research*, 117(1–2):1–19.

Zollo, A., Gasparini, P., Virieux, J., Biella, G., Boschi, E., Capuano, P., De Franco, R., Dell'Aversana, P., De Matteis, R., De Natale, G., et al. (1998). An image of mt. vesuvius obtained by 2d seismic tomography. *Journal of volcanology and geothermal research*, 82(1):161–173.